



# SHIVAJI UNIVERSITY, KOLHAPUR

Volume-49 Issue-1 (January, 2023)

ISSN-Science-0250-5347

Estd. 1962  
"A++" Accredited by NAAC (2021)  
with CGPA 3.52



## JOURNAL OF SHIVAJI UNIVERSITY : SCIENCE AND TECHNOLOGY

(Peer Reviewed Journal)

# JOURNAL OF SHIVAJI UNIVERSITY : SCIENCE AND TECHNOLOGY

(Peer Reviewed Journal)

Volume-49, Issue-1 (January, 2023)

ISSN Science-0250-5347

## EDITORIAL BOARD OF THE JOURNAL

**Prof. (Dr.) D. T. Shirke**

Chairman

Hon'ble Vice Chancellor, Shivaji University, Kolhapur

**Prof. (Dr.) P. S. Patil**

Hon'ble Pro Vice Chancellor, Shivaji University, Kolhapur

**Dr. V. N. Shinde**

Registrar (Ag.), Shivaji University, Kolhapur

**Prof. (Dr.) Smt. S. H. Thakar**

Dean, Faculty of Science & Technology, and  
Head, Department of Mathematics, Shivaji University, Kolhapur

**Prof. (Dr.) S. D. Delekar**

Editor,

Department of Chemistry, Shivaji University, Kolhapur

## MEMBERS OF THE EDITORIAL BOARD

<b>Prof. (Dr.) K. Y. Rajpure</b>	Head, Dept. of Physics, Shivaji University, Kolhapur
<b>Prof. (Dr.) Smt. J. P. Jadhav</b>	Head, Dept. of Bio-technology, Shivaji University, Kolhapur
<b>Prof. (Dr.) K. D. Sonawane</b>	Head, Dept. of Biochemistry, Shivaji University, Kolhapur
<b>Dr. S. N. Sapali</b>	Director, Dept. of Technology, Shivaji University, Kolhapur
<b>Prof. (Dr.) R. V. Gurav</b>	Head, Dept. of Botany, Shivaji University, Kolhapur
<b>Prof. (Dr.) S. B. Mahadik</b>	Head, Dept. of Statistics, Shivaji University, Kolhapur
<b>Dr. Smt. K. S. Oza</b>	Head, Dept. of Computer Science, Shivaji University, Kolhapur
<b>Prof. (Dr.) A. A. Deshmukh</b>	Head, Dept. of Zoology, Shivaji University, Kolhapur
<b>Prof. (Dr.) K. K. Sharma</b>	Head, Dept. of Nano Science & Technology, Shivaji University, Kolhapur
<b>Prof. (Dr.) S. D. Shinde</b>	Head, Dept. of Geography, Shivaji University, Kolhapur
<b>Dr. Smt. A. S. Jadhav</b>	Head, Dept. of Environmental Science, Shivaji University, Kolhapur
<b>Prof. (Dr.) P. K. Gaikwad</b>	Head, Dept. of Electronics, Shivaji University, Kolhapur



Estd. 1962  
"A++" Accredited by NAAC (2021)  
with CGPA 3.52

---

---

**Shivaji University**  
Kolhapur 416 004 (INDIA)

---

---

## **JOURNAL OF SHIVAJI UNIVERSITY : SCIENCE AND TECHNOLOGY**

(Peer Reviewed Journal)

.....  
**Volume-49, Issue-1 (January, 2023)**  
.....

ISSN Science-0250-5347  
.....

- Contact Details -

**Prof. (Dr.) S. D. Delekar**

Editor, Journal of Shivaji University : Science and Technology  
and

Department of Chemistry

Shivaji University, Kolhapur 416 004 (India)

E-mail : [editor,jscitech@unishivaji.ac.in](mailto:editor,jscitech@unishivaji.ac.in)

website : <http://www.unishivaji.ac.in/journals/>

---

---

---

---

Shivaji University, Kolhapur

---

---

**JOURNAL OF SHIVAJI UNIVERSITY :  
SCIENCE AND TECHNOLOGY**

(Peer Reviewed Journal)

.....  
**Volume-49, Issue-1 (January, 2023)**  
.....

ISSN Science-0250-5347  
.....

- Editor -

**Prof. (Dr.) S. D. Delekar**

Journal of Shivaji University :  
Science and Technology

- Published by -

**Dr. V. N. Shinde**

Ag. Registrar,  
Shivaji University, Kolhapur 416004.

- Printed by -

**Shri. B. P. Patil**

Superintend  
Shivaji University, Kolhapur 416004.

The Editor, on behalf of the Editorial Board of the Journal of Shivaji University : Science and Technology, Vol. No. 49 (1) wishes to express his thanks to the contributing authors and the experts for acting as referees for the papers included in the issue.

**Published : July, 2023**

---

---

**Journal of Shivaji University: Science and Technology**  
**Volume-49, Issue-1 (January,2023)**  
**INDEX**

<b>Sr. No.</b>	<b>Title of Research Article with Name of Author/s</b>	<b>Page No.</b>
1.	<b>Synthesis and Characterization of g-C<sub>3</sub>N<sub>4</sub> Decorated ZnONanorods and their Binder Free Deposited Photoanodes for Photoelectrochemical Water Splitting Studies</b> Pramod A. Koyale, Prakash S. Pawar, Swapnajit V. Mulik, Vijay S. Ghodake, Amol B. Pandhare, Ankita K. Dhukate, Sagar D. Delekar	1
2.	<b>Thiamine Hydrochloride (VB<sub>1</sub>) Catalyzed Synthesis of 5-aryl-4-phenyl-1,2,4-triazolidine-3-thiones in Aqueous Medium</b> Pradeep P. Patil, Prasad M. Swami, Shankar P. Hangirgekar, Sandeep A. Sankpal	10
3.	<b>Evaluation of Acute Toxic Effect of Gallic Acid Loaded Eudragit's 100 Nanoparticles on <i>Artemia Salina</i> Brine Shrimp Bioassay</b> PoournimaS. Sankpal, Sachinkumar V.Patil,SayaliS. Patil	20
4.	<b>Surface Modifications of Binder Free ZnONanorod Thin Films through Cds Quantum Dots for Dye Sensitized Solar Cells</b> Krantiveer V. More, Anant G. Dhodamani, Sajid B. Mullani, Tukaram D. Dongale,Prakash S. Pawar,Satish M. Patil, Sunil J. Kadam, Sagar D. Delekar	36
5.	<b>Review on Candle Soot based Superhydrophobic Surfaces for Oil-Water Separation</b> Mehejbin R. Mujawar, Rajesh B. Sawant, Amol B. Pandhare, Prashant D. Sanadi, Sanjay S. Latthe, Ankush M. Sargar, Raghunath K. Mane, Shivaji R. Kulal	50
6.	<b>A Review on Current Advancements in Magnetic Nanomaterials for Magnetic Hyperthermia Applications</b> Amol B. Pandhare, Prakash S. Pawar, Vijay S. Ghodake, Swapnajit V. Mulik, Pramod A. Koyale, Ankita K. Dhukate, Deepak B. Mohite, Karishma V. Shikhare, Rajendra P. Patil, Sagar D. Delekar	62
7.	<b>One-Step Synthesis of Biomass-Derived Carbon Dots: Study of Optical Properties</b> Akanksha G. Kolekar, Omkar S. Nille,Shubham J. Kumbhar, Priyanka S. Mahadar, Sayali B. Lohar, Govind B. Kolekar, Gavisiddappa S. Gokavi, Vishalkumar R. More	87
8.	<b>Synthesis and Characterization of Plant-Mediated CuO Nanoparticles</b> Omkar S. Nille, Harshad A. Mirgane, Sneha V. Koparde, Akanksha G. Kolekar, Ashlesha R. Pawar, Pallavi J. Pawar, Abhishek A. Waghmode, Tanaji R. Dhage, Vijay S. Ghodake, Prasad M. Swami, Sarita D. Shinde,Govind B. Kolekar	95

**Department of Chemistry**  
**Shivaji University, Kolhapur**

**Journal of Shivaji University (Science & Technology)**

**Volume-49, Issue-1 (January, 2023)**

**Departmental Editorial Board**

<b>Sr. No.</b>	<b>Name of the Faculty</b>	<b>Editorial Board Designation</b>
1.	Prof. (Dr.) K.D. Sonawane	Chairman
2.	Prof. (Dr.) G. B. Kolekar	Member
3.	Prof. (Dr.) S. S. Chavan	Member
4.	Prof. (Dr.) S. S. Kolekar	Member
5.	Prof. (Dr.) K. M. Garadkar	Member
6.	Prof. (Dr.) P.V. Anbhule	Member
7.	Prof. (Dr.) S. D. Delekar	Member
8.	Prof. (Dr.) A.V. Ghule	Member
9.	Prof. (Dr.) D. M. Pore	Member
10.	Prof. (Dr.) D. H. Dagade	Member
11.	Prof. (Dr.) G. S. Rashinkar	Member
12.	Dr.D. S. Bhange	Member
13.	Dr.S.A. Sankpal	Member
14.	Dr. S.N. Tayade	Member



# Synthesis and Characterization of g-C<sub>3</sub>N<sub>4</sub> Decorated ZnO Nanorods and their Binder Free Deposited Photoanodes for Photoelectrochemical Water Splitting Studies

Pramod A. Koyale<sup>a</sup>, Prakash S. Pawar<sup>a,b</sup>, Swapnajit V. Mulik<sup>a</sup>, Vijay S. Ghodake<sup>a,d</sup>, Amol B. Pandhare<sup>a,c</sup>, Ankita K. Dhukate<sup>a</sup>, Sagar D. Delekar<sup>a,\*</sup>

<sup>a</sup>Department of Chemistry, Shivaji University, Kolhapur 416 004 (MS) India.

<sup>b</sup>Department of Chemistry, Shri Yashwantaro Patil Science College, Solankur, Kolhapur 416 212 (MS) India.

<sup>c</sup>Department of Chemistry, M.H. Shinde Mahavidyalaya, Tisangi, Gaganbavda, Kolhapur 416 206 (MS) India.

<sup>d</sup>Department of Chemistry, Yashwantrao Chavan Mahavidyalaya, Halkarni, Kolhapur 416 552 (MS) India.

\*Corresponding author: [sdd\\_chem@unishivaji.ac.in](mailto:sdd_chem@unishivaji.ac.in)

---

## ABSTRACT

Photoelectrochemical water splitting is one the efficient technology for solar energy conversion. In this connection, the present study is focused towards the synthesis of g-C<sub>3</sub>N<sub>4</sub> decorated ZnO nanorods and their characterization for structural, optical and morphological analysis. Binder free thin film deposition is deployed to design stable and efficient photoanodes. The fabricated g-C<sub>3</sub>N<sub>4</sub> decorated ZnO nanorods displayed the higher PEC performance with current density of 0.88 mA cm<sup>-2</sup> at 1.23 V vs. RHE, almost four times greater than that of bare ZnO nanorods.

## KEYWORDS

ZnO NRs, g-C<sub>3</sub>N<sub>4</sub>, Solar energy, Photoelectrochemical water splitting.

.....

## 1. INTRODUCTION

As energy demand across the world is growing rapidly, the utilization of solar energy for sustainable development including hydrogen generation as well as electricity generation is singing very dominant role [1,2]. And for this, the various efforts have been accomplished through research community for generation the efficient materials with the great impact. Where, the various metal oxides as well as organic materials have been exploited to design an effective system for said purpose [3]. Among such materials, nanostructured zinc oxide (ZnO) having wide band gap (~3.2 eV), non-toxic nature, easy synthetic protocol, etc. have been attracted as effective option for energy studies. But due to their incompetent optical property as well as deprived charge transportation, the use of bare ZnO brings the limitation to the studies [4], which provides the option to form composites of ZnO with other active materials to fulfil their drawbacks. g-C<sub>3</sub>N<sub>4</sub> with efficient optical property and well aligned band levels to that of ZnO. Nevertheless, pure g-C<sub>3</sub>N<sub>4</sub> owning high radiative recombination rate of photogenerated electrons and holes which revealing the high

fluorescence yield with incompetent performance [5]. Hence, it is possible to reduce recombination rate of electron-hole pairs by the incorporating with ZnO [5]. Chen et al., demonstrated the electrochemically deposited ZnO nanorods (NRs) arrays which were sulfurated following hydrothermal reaction to form ZnO/ZnS/g-C<sub>3</sub>N<sub>4</sub> nanocomposites (NCs) [6]. In this investigation, ZnO/ZnS/g-C<sub>3</sub>N<sub>4</sub> NCs showed the photocurrent density of 0.66 mA cm<sup>-2</sup> at 1.23 V vs. RHE. It has been highly appreciated for composite formation with excellent photoelectrochemical properties with competent current stability by the simple strategy.

In this connection, present work is focused to design well-organized NCs assembly of g-C<sub>3</sub>N<sub>4</sub> decorated ZnO NRs by uniting their synergistic effect for efficient photoelectrochemical water splitting. ZnO NRs were synthesized using simple sol-gel method, while g-C<sub>3</sub>N<sub>4</sub> nanosheets formed by thermal pyrolysis method. The sonochemical treatment was deployed to enterprise ZnO/g-C<sub>3</sub>N<sub>4</sub> NCs. Thereafter, structural and optical properties of ZnO/g-C<sub>3</sub>N<sub>4</sub> NCs were investigated. Binder free deposition of synthesized materials with variable thickness was carried out to design thin film photoanodes. Further investigation of was deployed to perceive the photoelectrochemical behavior of the ZnO NRs and ZnO/g-C<sub>3</sub>N<sub>4</sub> NCs.

## **2. EXPERIMENTAL SECTION**

### **2.1. Materials**

Zinc acetate (C<sub>4</sub>H<sub>10</sub>O<sub>6</sub>Zn.2H<sub>2</sub>O, 99%), ammonia (NH<sub>4</sub>OH, 30%), urea (NH<sub>2</sub>.CO.NH<sub>2</sub>, 99%), *N,N*-dimethylformamide (DMF, C<sub>3</sub>H<sub>7</sub>NO, 99.5%), acetonitrile (CH<sub>3</sub>CN, 99.9%) and the substrate utilized for thin film design is fluorine doped tin oxide (FTO) glass were purchased from Sigma-Aldrich, India.

### **2.2. Synthesis of ZnO NRs**

ZnO NRs were equipped by simple sol-gel technique, which was priorly deployed by our research group [7].

### **2.3. Synthesis of g-C<sub>3</sub>N<sub>4</sub>**

Simple thermal pyrolysis method was deployed for synthesis of g-C<sub>3</sub>N<sub>4</sub> nanosheets [8]. The product was obtained by the pyrolysis of mixture of thiourea and urea with equal quantity. For this purpose, the reaction mixture was poured in silica crucible at temperature of 550°C for nearly about 5 hours. Yellow powder of g-C<sub>3</sub>N<sub>4</sub> nanosheets was collected at the end after cooling.

### **2.4. Synthesis of ZnO/g-C<sub>3</sub>N<sub>4</sub> NCs**

The formation of ZnO/g-C<sub>3</sub>N<sub>4</sub> NCs with variation in amount of 0.5%, 1%, and 1.5% of g-C<sub>3</sub>N<sub>4</sub>, was carried out using sonochemical technique. Firstly, certain amount of g-C<sub>3</sub>N<sub>4</sub> nanosheets was sonicated in ethanol for few minutes to get swell and exfoliate and then required amount of ZnO was added to g-C<sub>3</sub>N<sub>4</sub> solution. The whole



solution was sonicated for next 30 minutes and finally dried at 50°C in open air to get ZnO/g-C<sub>3</sub>N<sub>4</sub> NCs which is represented as ZCN NCs. Further same protocol was utilized to get different ZCN NCs. The synthesized samples were named as ZCN0.5, ZCN1, and ZCN1.5 for 0.5%, 1%, and 1.5% of g-C<sub>3</sub>N<sub>4</sub>, respectively.

## 2.5. Fabrication of working electrode

Simple binder free thin film deposition was accomplished using doctor-blade technique, which was reported by our research group previously [9].

## 2.6. Characterizations

The crystallinity and phase structure determination of the synthesized samples were analyzed using X-ray diffractometer (XRD, Bruker, AXS D8 Advance). To investigate the functional moieties which present in the synthesized material, fourier transform infrared spectrometer (FTIR, Bruker, Alpha) was exploited by locating FTIR spectra with the range of wavenumber 4000-400cm<sup>-1</sup>. UV-Visible diffused reflectance spectra were used to explore the optical behavior of synthesized materials using UV-Visible spectrophotometer (LABINDIA Analytical, UV 3000+). Scanning electron microscopy (SEM, JSM-6360, JEOL Ltd. Japan) was used to analyze the surface morphology of the synthesized materials.

## 2.7. Photoelectrochemical Set up

PEC study was accomplished using three electrode system. The fabricated ZnO/g-C<sub>3</sub>N<sub>4</sub> NCs based electrodes were used as working electrode (WE), while platinum (Pt) plate and saturated calomel electrode (SCE) were utilized as counter electrode (CE) and reference electrode (RE), respectively. PEC study was carried out in 0.5 M Na<sub>2</sub>SO<sub>4</sub>. Whole setup was maintained under UV-Visible illumination sourced from AM 1.5 G solar simulator (100 mW/cm<sup>2</sup>). The photocurrent was measured by applying a constant potential scan rate of 10 mV/S within potential window of -0.3 V to 0.65 V (vs. SCE). In addition, chronoamperometry study was performed over 400 seconds. All photoelectrochemical performance were carried out using CH instrument D650 potentiostat.

## 3. RESULTS AND DISCUSSION

**Figure-1a** exhibits the characteristic peaks of hexagonal wurtzite ZnO phase at diffraction angles of 31.84°, 34.45°, 36.28°, 47.57°, 56.63°, 62.87°, and 67.93° corresponding to the (100), (002), (101), (102), (110), (103), and (112) reflections; respectively. It displays the lattice constant values *a* and *c* which are 3.25 and 5.21, respectively (*JCPDS NO. 01-080-0074, Space group=P63mc*) [7,10,11]. The XRD pattern of g-C<sub>3</sub>N<sub>4</sub> revealed the distinctive peak at diffraction angle of 27.34° corresponding to (002), which was embodied for pure g-C<sub>3</sub>N<sub>4</sub> [11]. As little amount of g-C<sub>3</sub>N<sub>4</sub> utilized in ZCN NCs, its distinctive peaks are not observing in the pattern of ZCN NCs. But it was observed that, as the concentration of g-C<sub>3</sub>N<sub>4</sub> is increased in

ZnO lattice, the intensity of characteristic peaks of ZnO NRs observed to be reduced [11,12]. Hence, XRD pattern reveals the successful incorporation of g-C<sub>3</sub>N<sub>4</sub> in ZnO lattice. Crystallite size of all samples were also calculated using Debye-Scherrer equation, which are discussed in **Table-1**.

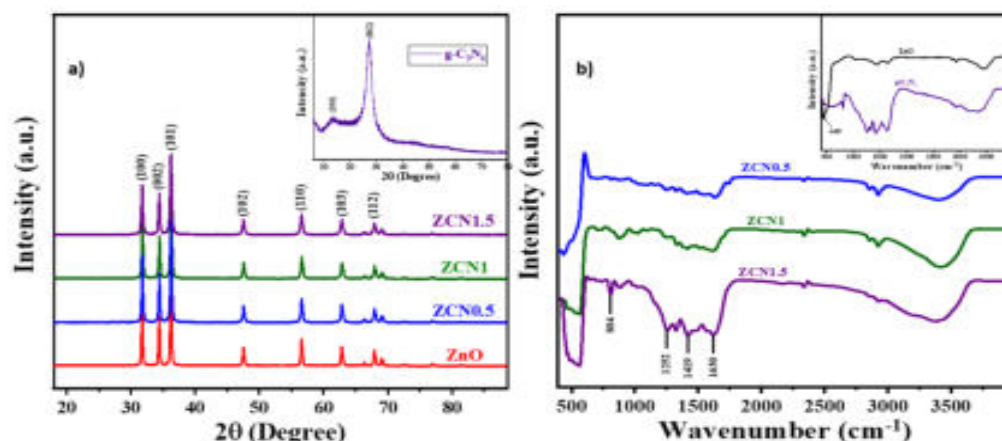


**Figure-1.** a) XRD pattern for all samples including bare ZnO and ZCN NCs. XRD pattern of pure g-C<sub>3</sub>N<sub>4</sub> (inset), b) FTIR spectra of ZCN NCs and bare ZnO & g-C<sub>3</sub>N<sub>4</sub> (inset).

**Table-1.** The observed FWHM (full width high maxima), crystallite size and optical band gap of the bare ZnO NRs and ZCN NCs.

Sample	FWHM ( $\theta$ )	Crystallite Size (nm)	Band gap (eV)
ZnO	0.25143	34.74	3.14
ZCN0.5	0.27591	31.65	3.10
ZCN1	0.29218	29.89	3.09
ZCN1.5	0.34073	25.63	3.06
g-C <sub>3</sub> N <sub>4</sub>	4.2587	2.05	2.78

In **Figure-1b**, FTIR spectra for all samples are shown. In case of bare ZnO NRs, FTIR spectra displays the characteristic vibrational band at  $\sim 449$  cm<sup>-1</sup> which corresponds to Zn-O stretching mode, and broad frequency region at 3000-3500 cm<sup>-1</sup> due to -OH functional moieties [7,13]. For pure g-C<sub>3</sub>N<sub>4</sub>, the spectra consist of characteristic peaks at 1200-1600 cm<sup>-1</sup>, i.e., peak at 1631 cm<sup>-1</sup> corresponds to C=N stretching vibration modes, while peaks at 1252, 1324 and 1419 cm<sup>-1</sup> correspond to aromatic C-N stretching vibration modes<sup>13</sup>. The peak at 804 cm<sup>-1</sup> associated with out of plane bending vibration of triazine units. While the broad peak observed between 3000 to 3400 cm<sup>-1</sup> describes the presence of -N-H functional moieties [14]. For all

ZCN NCs, it is observed that as concentration of g-C<sub>3</sub>N<sub>4</sub> enhanced, the intensity of the peaks at 1200-1600 cm<sup>-1</sup> and 804 cm<sup>-1</sup> gets higher. Also, the characteristic broad peaks at 3000-3500 cm<sup>-1</sup> get detached with increased amount of g-C<sub>3</sub>N<sub>4</sub> in ZnO lattice, which reveals the successful incorporation of g-C<sub>3</sub>N<sub>4</sub> into ZnO lattice.

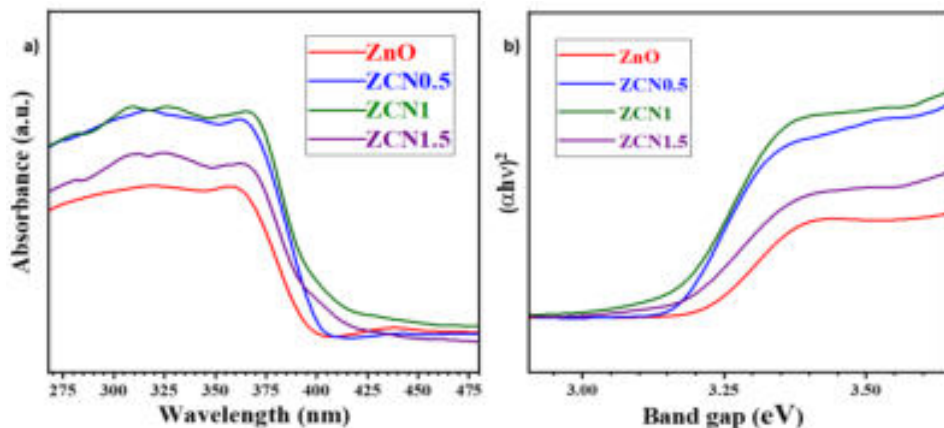


**Figure-2. a) UV-Visible spectra, and b) Tauc plot for representative ZCN NCs.**

**Figure-2a** displays the proper UV-visible spectrum for the desired sample, where absorption edge perceived at 395 nm [15]. The bare ZnO NRs observed to be inactive in the visible region. It was observed that, absorption enhanced from 395 nm to 449 nm for ZCN1.5. Hence, such incorporation of ZnO NRs with g-C<sub>3</sub>N<sub>4</sub> is foremost to stimulate the material in the visible region. **Figure-2b** represents the band gap calculation of synthesized materials using Tauc plot  $(\alpha h\nu)^2$ , where  $\alpha$  is absorption coefficient,  $h$  is plank's constant, and  $\nu$  is the frequency [16]. The observed band gap values for all samples are mentioned in **Table-1**.

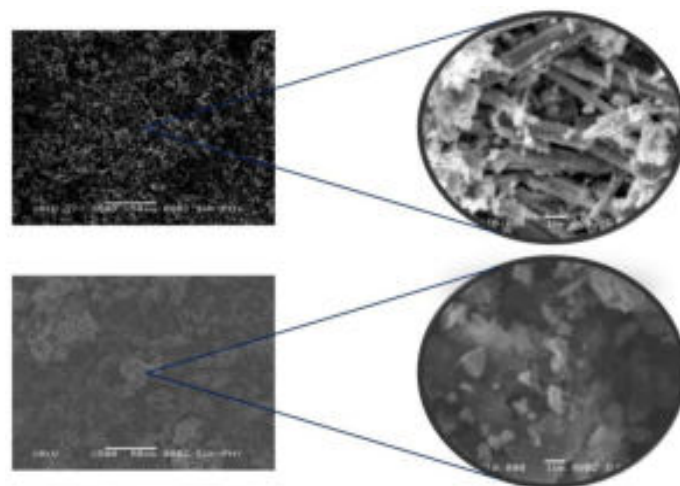


**Figure-3. SEM images: a) bare ZnO NRs and b) ZCN1.5 at 50 μm and 1 μm.**

### 3.1.Photoelectrochemical Performance:

The morphology images of the synthesized bare ZnO NRs as well as ZCN NCs are shown in **Figure-3**. The clear evidence about hexagonal ZnO NRs, established from SEM images. Wherein the incorporation of g-C<sub>3</sub>N<sub>4</sub> into ZnO lattice leads to form aggregates, due to the sheet like structures of g-C<sub>3</sub>N<sub>4</sub>.

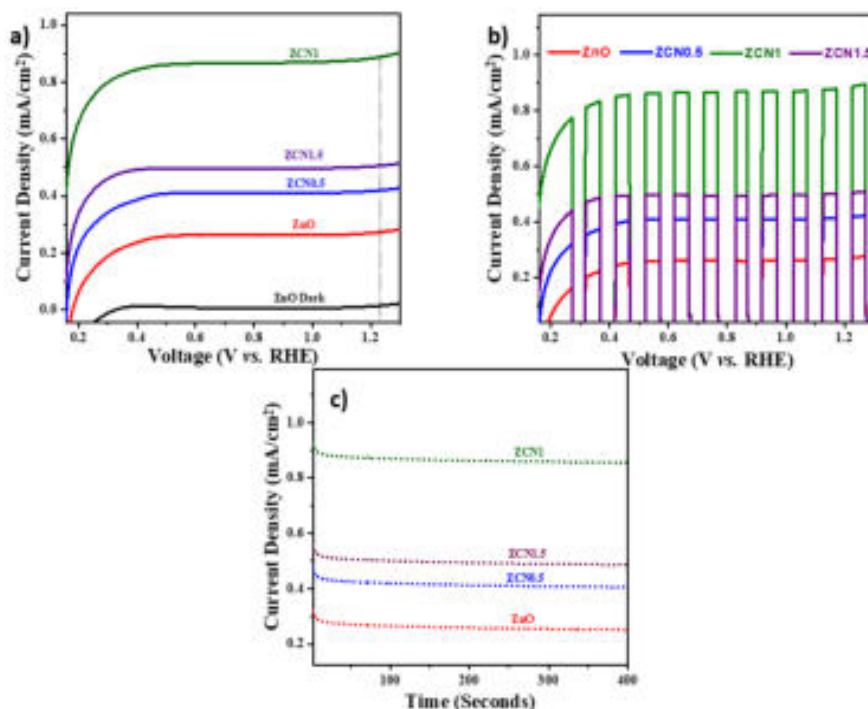


**Figure-4.** a) current-voltage curves under both light and dark conditions for bare and ZCN NCs based photoanodes, b) current-voltage curves under chopped light as well as dark conditions for bare ZnO and ZCN NCs based photoanodes, and c) the chronoamperometric curves for bare ZnO NRs and ZCN NCs based photoanodes.

**Figure-4a** displays the linear sweep voltammograms (LSV) for bare ZnO NRs as well as ZCN NCs within potential range of 0.15 to 1.3 V vs. RHE. It was observed that, current density enhanced to 0.88 mA cm<sup>-2</sup> for ZCN1 NCs at 1.23 V vs. RHE, which was almost four times greater than that of bare ZnO NRs based working electrode (0.26 0.88 mA cm<sup>-2</sup>). **Figure-4b** showed the chopped LSV for all design working electrodes. The stability of the fabricated ZnO NRs based as well as ZCN NCs based working electrodes was taken using chronoamperometric analysis, as shown in **Figure-4c**. The overall PEC performance and related parameters of the materials are discussed in **Table-2**.

**Table-2. The overview of PEC parameters for designed photoanodes of ZnO NRs and ZCN NCs.**

Sample	Current Density (mA/cm <sup>2</sup> )	Stability (over 400 sec.) (μA/cm <sup>2</sup> )
ZnO	0.26	247
ZCN0.5	0.41	405
ZCN1	0.88	858
ZCN1.5	0.51	485

**Table-3** shows the comparison of PEC results obtained for the different previously reported materials with this present investigation and hence revealing the superior PEC performance to that of other reported materials.

**Table-3. Comparison of PEC results obtained for present study with different previously reported works.**

Sr. No	Scheme	Output	Electrolyte	Ref.
1.	ZnO Nanotubes@N-CD@ZIF-8	0.4 at 0.5 V <i>vs.</i> Ag/AgCl	0.5 M Na <sub>2</sub> SO <sub>4</sub>	[13]
2.	ZnO/ZnFe <sub>2</sub> O <sub>4</sub> /NiOOH	0.48 at 1.23 V <i>vs.</i> RHE	0.1 M Na <sub>2</sub> SO <sub>4</sub>	[17]
3.	Ni- doped ZnO thin films	0.25 at 1.23 V <i>vs.</i> RHE	0.3 M Na <sub>2</sub> SO <sub>4</sub>	[5]
4.	ZnO nanotrees/ nanoclusters	0.67 at 1 V <i>vs.</i> Ag/AgCl	0.5 M Na <sub>2</sub> SO <sub>4</sub>	[12]
5.	ZnO/ZnS/g-C <sub>3</sub> N <sub>4</sub>	0.66 at 1.33 V <i>vs.</i> RHE	0.5 M Na <sub>2</sub> SO <sub>4</sub>	[6]
6.	ZnO/g-C <sub>3</sub> N <sub>4</sub> NCs ( <b>This work</b> )	0.88 at 1.23 V <i>vs.</i> RHE	0.5 M Na <sub>2</sub> SO <sub>4</sub>	--

#### 4. CONCLUSION

In present work, the ZCN NCs were prepared using simple sonochemical method. Further bare ZnO NRs and ZCN NCs based working electrodes were fabricated via binder free technique. The structural, optical as well as morphological studies were preformed using XRD, FTIR, UV-Visible DRS and SEM analysis. The highest PEC performance was observed for ZCN1 NCs based working electrode, which also possessing high chronoamperometric stability. Hence, such ZCN NCs based

photoanodes will be highly appreciated and efficient for solar energy conversion studies.

## ACKNOWLEDGMENT

Author Pramod A. Koyale and Sagar D. Delekar honestly thank to Department of Science and Technology, India for financial funding through DST-INSPIRE Fellowship.

## REFERENCES

1. Koyale, P. A., Panda, D. K., Delekar, S. D. In *Advances in Metal Oxides and Their Composites for Emerging Applications*, edited by Delekar S. D. Elsevier, (2022) pp.339–376.
2. Pawar, P. S., Koyale, P. A., Dhodamani, A. G., Delekar, S. D. In *Advances in Metal Oxides and Their Composites for Emerging Applications*, edited by Delekar S. D. Elsevier, (2022) pp.263–286.
3. Koyale, P. A., Panda, D. K., Delekar, S. D. In *Advances in Metal Oxides and Their Composites for Emerging Applications*, edited by Delekar S. D. Elsevier, (2022) pp.3-56.
4. Dalapati, G. K., Sharma, H., Guchhait, A., Chakrabarty, N., Bamola, P., Liu, Q., Saianand, G., Krishna, A. M. S., Mukhopadhyay, S., Dey, A., Wong, T. K. S. (2021) *Journal of Materials Chemistry A*, 9, 16621–16684.
5. Chetia, T. R., Ansari, M. S., Qureshi, M. (2016) *Journal of Materials Chemistry A*, 4, 5528–5541.
6. Liu, C., Qiu, Y., Wang, F., Wang, K., Liang, Q., Chen, Z. (2017) *Advanced Material Interfaces*, 4, 1700681.
7. Mullani, S. B., Dhodamani, A. G., Shellikeri, A., Mullani, N. B., Tawade, A. K., Tayade, S. N., Biscay, J., Dennany, L., Delekar, S. D. (2020) *Scientific Reports*, 10, 1–18.
8. Yang, D., Zhao, X., Chen, Y., Wang, W., Zhou, Z., Zhao, Z., Jiang, Z. (2019) *Industrial & Engineering Chemistry Research*, 58, 5516–5525.
9. Delekar, S. D., Dhodamani, A. G., More, K. V., Dongale, T. D., Kamat, R. K., Acquah, S. F., Dalal, N. S., Panda, D. K. (2018) *ACS Omega*, 3, 2743–2756.
10. Mullani, S. B., Tawade, A. K., Tayade, S. N., Sharma, K. K. K., Deshmukh, S. P., Mullani, N. B., Mali, S. S., Hong, C. K., Swamy, B. K., Delekar, S. D. (2020) *RSC Advance*, 10, 36949–36961.

11. Guan, R., Li, J., Zhang, J., Zhao, Z., Wang, D., Zhai, H., Sun, D. (2019) ACS Omega, 4, 20742–20747.
12. Singh, A. K., Shukla, N., Verma, D. K., Kumar, B., Rastogi, R. B. (2021) Industrial & Engineering Chemistry Research, 60, 864–874.
13. Paul, D. R., Gautam, S., Panchal, P., Nehra, S. P., Choudhary, P., Sharma, A. (2020) ACS omega, 5, 3828–3838.
14. Jiang, D., Chen, L., Xie, J., Chen, M. (2014) Dalton Transactions, 43, 4878–4885.
15. Gogurla, N., Sinha, A.K., Santra, S., Manna, S., Ray, S.K. (2014) Scientific Reports, 4, 1–9.
16. Verma, K. C., Goyal, N., Kotnala, R. K. (2019) Physical Chemistry Chemical Physics, 21, 12540–12554.
17. Lan, Y., Liu, Z., Guo, Z., Li, X., Zhao, L., Zhan, L., Zhang, M. (2018) Dalton Transactions, 47, 12181–12187.



# Thiamine Hydrochloride (VB<sub>1</sub>) Catalyzed Synthesis of 5-aryl-4-phenyl-1,2,4-triazolidine-3-thiones in Aqueous Medium

Pradeep P. Patil<sup>a,b</sup>, Prasad M. Swami<sup>a</sup>,  
Shankar P. Hangirgekar<sup>a</sup>, Sandeep A. Sankpal<sup>a,\*</sup>

<sup>a</sup>Department of Chemistry, Shivaji University, Kolhapur 416 004 (MS) India.

<sup>b</sup>School of Chemical Sciences, Sanjay Ghodawat University, Atigre 416 118 (MS) India.

\*Corresponding author:sandeeporg1@gmail.com

---

## ABSTRACT

*5-aryl-4-phenyl-1, 2, 4-triazolidine-3-thiones* is still a demanding class of triazoles. In the present work, we have emerged thiamine hydrochloride (VB<sub>1</sub>) a renowned natural organocatalyst for the synthesis of 5-aryl-4-phenyl-1, 2, 4-triazolidine-3-thiones by adopting one-pot three component condensation of phenyl isothiocyanate, hydrazine hydrate and diverse aromatic aldehydes in an aqueous medium. This methodology represents a sustainable approach by using water as a green solvent, with broad substrate scope, shorter reaction time, and high atom economy etc.

## KEYWORDS

*Thiamine hydrochloride (VB<sub>1</sub>), Multicomponent reaction, 5-aryl-4-phenyl-1, 2, 4-triazolidine-3-thiones, Green solvent, Reusable catalyst.*

.....

## 1. INTRODUCTION

The exploration of environmentally amenable synthetic methodologies to discover heterocyclic compounds from easily available precursors through a one-pot multicomponent reaction (MCR) strategy [1]. Ideally, the MCRs will be adequately versatile and have attracted a strong attention due to the incorporation of multiple functions into one system for specific applications [2]. Additionally, the interactions between different components through a single method can provide the expedient synthesis of libraries of bioactive drug molecule [3]. In recent years, the substitution of volatile and toxic organic solvents by water as a sustainable medium for numerous organic transformations due to its manifold advantages such as being environmentally friendly, inexpensive, non-toxic, ease of availability, and greater heat capacity [4]. Moreover, water possesses a high dielectric constant, good selectivity, and able to dissolve large number of precursors to increase the reactivity [5].



A promising synthetic approach to use a catalytic system is capable of accelerating and studying the progress of the reaction. As an eco-benign catalyst, thiamine hydrochloride (VB<sub>1</sub>) is one of the investigated parts in the field of biocatalysis [6]. As being versatile catalyst, it has reflected diverse applications in organic reactions and transformations such as 1,4-dihydropyridines [7], xanthene derivatives [8], polyhydroquinoline [9], dihydroquinazolin [10], etc. Its miscellaneous applications are due to easy availability, non-toxic, biodegradability, air, and water stability, etc.

Recently triazoles and substituted triazoles are very interesting five-membered heterocyclic compounds present as pharmaceutically active ingredients [11]. Furthermore, they are found to possess a broad array of applications in agrochemicals and pharmaceuticals [12]. Moreover, N-substituted 1,2,4-triazoles have been very enticing as a consequence of their wide array of biological applications like Antibacterial [A] [13], 1,2,4-triazole stuck with pyridazine scaffold shows significant Antiviral [B] properties [14], Loreciezole with chloro substitution plays a vital role as an Anticonvulsant [C] [15] and Letrozole containing 1,2,4-triazole are more efficacious against Anticancer [D] [16] activity as shown in **Figure-1**.

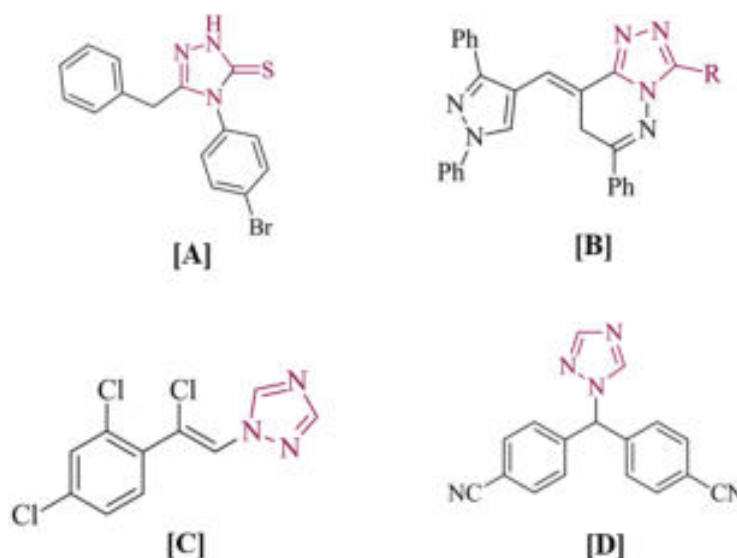


**Figure-1. Examples of pharmacologically useful 1,2,4-triazole molecular scaffolds.**

From the literature survey, previous reports on the synthesis of such 5-aryl-4-phenyl-1, 2, 4-triazolidine-3-thiones molecular scaffold from the reaction between phenyl isothiocyanate, hydrazine hydrate, and aromatic aldehydes using Lewis acid surfactant combined catalyst [BZT]AlCl<sub>4</sub> [17], HCl [18], sulphamic acid [19], etc. As

part of our ongoing endeavors, we have developed a facile and convenient method for the synthesis of diverse 5-aryl-4-phenyl-1, 2, 4-triazolidine-3-thiones using thiamine hydrochloride (VB<sub>1</sub>) as a catalyst in aqueous medium at ambient conditions.

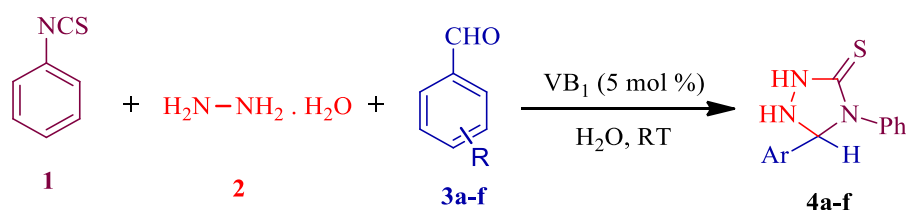
## 2. EXPERIMENTAL PROCEDURE

### 2.1. General considerations

All reagents and chemicals were procured from spectrochem, Loba, and Aldrich chemical companies. All reactions were performed at ambient temperature by using oven-dried glassware. <sup>1</sup>H (400 MHz) and <sup>13</sup>C (100 MHz) NMR spectra were carried out by using Bruker AVANCE spectrometer using CDCl<sub>3</sub> as the dissolving solvent and tetramethylsilane as the internal reference standard. DBK programmed melting point apparatus was used to define the physical constant (melting points) with temperature increment 2-3 °C/ min. and were uncorrected. FT-IR spectroscopy (Bruker alpha spectrometer), was employed to study the functional groups and measured in cm<sup>-1</sup>. The reaction monitoring was accomplished via Thin-layer chromatography (TLC) on silica gel-coated aluminium sheets.

### 2.2. General procedure for the synthesis of 5-phenyl-1,2,4-triazolidine-3-thione derivative

A mixture of Aromatic/heteroaromatic aldehyde (1 mmol), hydrazine hydrate (1 mmol), phenyl isothiocyanate (1 mmol), VB<sub>1</sub> (15 mol %), and water (5 mL) was taken in a round bottom flask (50 mL) and stirred at room temperature till completion of reaction monitored by TLC (8:2 v/v, pet ether: ethyl acetate). After the accomplishment of the reaction, water (20 mL) was added and the product was filtered to separate the catalyst. The crude product was dried in an oven at 50 °C and further purified by recrystallization from hot ethanol.



### 2.3. Spectral data of synthesized compound

#### 2.3.1. 4-phenyl-5-(pyridin-4-yl)-1,2,4-triazolidine-3-thione (Table-2.3, entry 4b)

Golden solid; M.P. 202-04 °C (lit., 204 °C); IR (KBr): 3422, 3376, 3292, 3117, 2961, 2891, 2789, 1725, 1640, 1594, 1492, 1249, 1176, 1079, 911, 678 cm<sup>-1</sup>; <sup>1</sup>H NMR (400 MHz, CDCl<sub>3</sub>): δ 7.32-7.26 (1H, m, Ar-H), 7.46-7.42 (2H, m, Ar-H), 7.55-7.54 (2H, q, *J*=3.6, 6 Hz Ar-H), 7.67-7.65 (1H, d, *J*=7.6 Hz, Ar-H), 7.87 (1H, s, -CH), 8.70-8.69 (2H, d, *J*=5.2 Hz, Ar-H), 9.18 (1H, s, -NH), 10.11 (1H, s, -NH);

<sup>13</sup>C NMR (100 MHz, CDCl<sub>3</sub>): δ 121.04, 124.70, 126.72, 128.96, 137.39, 139.76, 140.29, 150.55, 176.16.

### 3. RESULTS AND DISCUSSION

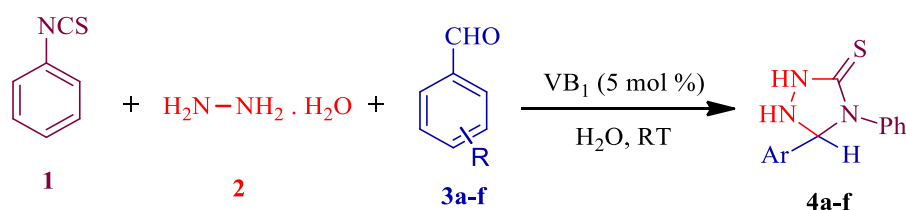
To explore the catalytic activity of thiamine hydrochloride (VB<sub>1</sub>), the model reaction of phenyl isothiocyanate, hydrazine hydrate, and benzaldehyde was investigated in water at room temperature and the obtained results are summarized in **Table-1**. Accordingly, we primarily carried out the reaction, in absence of solvent and catalyst at room temperature condition, which resulted in very trace yield of desired 5-phenyl-1,2,4-triazolidine-3-thione (**4a**) (**Table-1**, entry 1). Also, the very inferior yield of the product was observed without a catalyst in an aqueous medium (**Table-1**, entry 2). Thereafter, the same model reaction was screened to test the efficiency of the VB<sub>1</sub> catalyst in H<sub>2</sub>O, H<sub>2</sub>O:C<sub>2</sub>H<sub>5</sub>OH (1:1), C<sub>2</sub>H<sub>5</sub>OH, CH<sub>2</sub>Cl<sub>2</sub> and CH<sub>3</sub>CN reaction medium. Among the different polar/non-polar solvents, using an aqueous medium and 10 mol % of VB<sub>1</sub> catalyst showed an 88 % yield of the desired 5-aryl-4-phenyl-1, 2, 4-triazolidine-3-thione (**Table-1**, entry 7). Herein, we also performed the same model reaction by using PTSA, CSA, oxalic acid, and L-proline as a catalyst in same aqueous medium, which showing no substantial improvement in the yield and reaction time.

**Table-1. Optimization of reaction conditions<sup>[a]</sup> in the formation of 3a.**

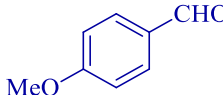
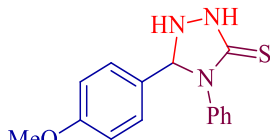
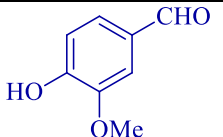
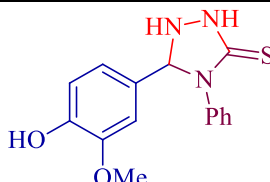
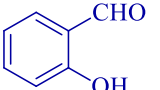
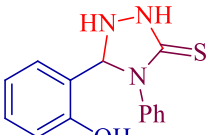
Entry	Solvent	Catalyst (mol %)	Time (min)	Yield <sup>[b]</sup> (%)
1	--	--	180	Trace
2	H <sub>2</sub> O	--	180	38
3	H <sub>2</sub> O	VB <sub>1</sub> (5)	54	80
4	H <sub>2</sub> O:C <sub>2</sub> H <sub>5</sub> OH	VB <sub>1</sub> (10)	39	83
5	C <sub>2</sub> H <sub>5</sub> OH	VB <sub>1</sub> (10)	46	80
6	CH <sub>2</sub> Cl <sub>2</sub>	VB <sub>1</sub> (10)	80	66
7	CH <sub>3</sub> CN	VB <sub>1</sub> (10)	120	59
8	H <sub>2</sub> O	VB <sub>1</sub> (10)	35	88
9	H <sub>2</sub> O	VB <sub>1</sub> (15)	35	89
10	H <sub>2</sub> O	PTSA (10)	40	78
11	H <sub>2</sub> O	CSA (10)	48	74
12	H <sub>2</sub> O	Oxalic acid (10)	51	69
13	H <sub>2</sub> O	L-proline(10)	100	75

With the optimized conditions in hand, we then set out to explore the robustness and generality of the protocol by using structurally diverse aromatic aldehydes containing electron-donating and withdrawing substituents (1 mmole), phenyl isothiocyanate (1 mmole), and hydrazine hydrate (1 mmole) as depicted in **Table-2**, entries **4a–f**. To address the factors that define the reaction outcome, the aromatic aldehydes bearing both electron-withdrawing and electron-donating substituents participated well in the reaction affording the corresponding 5-aryl-4-phenyl-1, 2, 4-triazolidine-3-thione (**4**) in much higher yields, illuminating no obvious steric and electronic impact (**Table-2**, 4c-f).

**Table-2. Substrate Scope for Synthesis of 5-aryl-4-phenyl-1,2,4-triazolidine-3-thiones<sup>[a]</sup>**

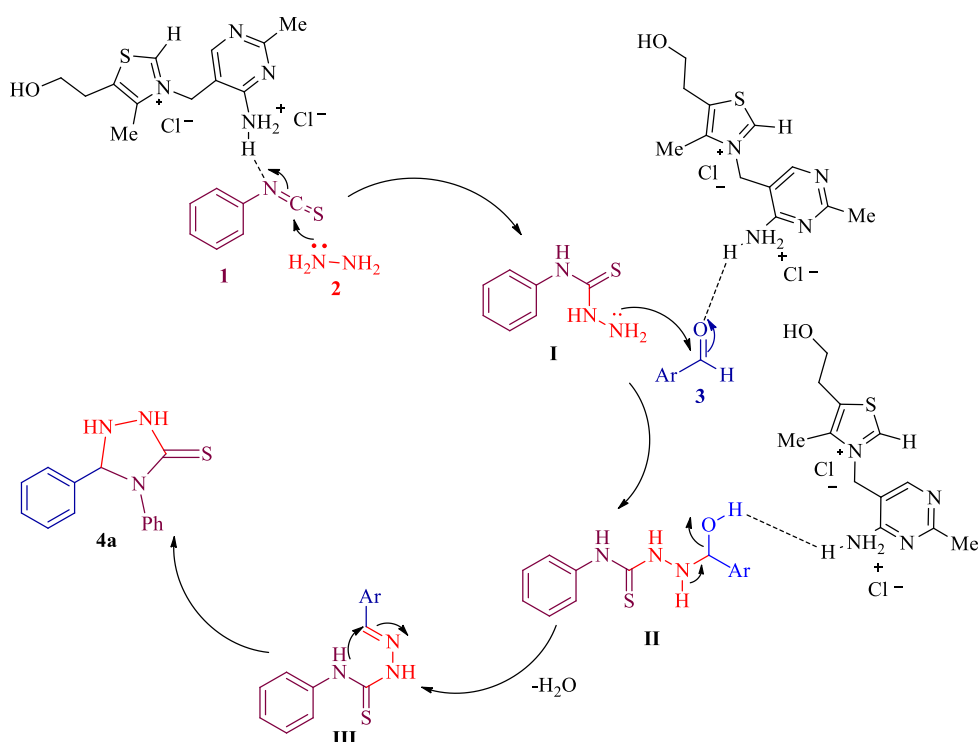


Entry	Aryl aldehyde	Product	Time (min)	Yield <sup>[b]</sup> (%)	Atom Economy <sup>[d]</sup>
<b>4a</b>			35	88	93
<b>4b</b>			44	90	93
<b>4c</b>			34	92	94

<b>4d</b>			39	86	94
<b>4e</b>			42	84	94
<b>4f</b>			40	83	93

Reaction conditions: Phenyl isothiocyanate (1 mmol), Hydrazine hydrate (1 mmol), aryl aldehyde (1 mmol) 10mol % VB<sub>1</sub> in water (5mL) at room temperature. <sup>b</sup>Isolated yield.

We herein propose a plausible reaction mechanism for VB<sub>1</sub> catalyzed synthesis of 5-aryl-4-phenyl-1,2,4-triazolidine-3-thiones (**4a**) as shown in **Scheme 1**. Initially, nucleophilic addition of hydrazine hydrate (**2**) to thiocarbonyl carbon of phenyl isothiocyanate (**1**) activated by thiamine hydrochloride (VB<sub>1</sub>), formation of amine intermediate (**I**) takes place. Further, nucleophilic attack of the -NH<sub>2</sub> group of amine intermediate (**I**) to the carbonyl carbon of aldehyde (**3**) in acidic condition furnishes the intermediate (**II**). Meanwhile, intermediate (**II**) undergoes loss of water molecule to form imine (**III**) and it undergoes intramolecular hydrogen transfer followed by cyclization to yield desired product **4a**.



**Scheme-1. Proposed mechanism for the synthesis of 5-aryl-4-phenyl-1,2,4-triazolidine-3-thiones in presence of VB<sub>1</sub>**

The recyclability and reusability of the catalyst is the prime goal of our current methodology. In this regard, the reaction media comprising the VB<sub>1</sub> catalyst and solvent was filtered after complete conversion into product molecules as indicated by TLC. The catalyst was recovered by the elimination of water by applying reduced pressure. The recovered VB<sub>1</sub> catalyst was washed thoroughly with absolute ethanol (2x4 mL) to remove loosely bound organic matter from its surface. Finally, the recycled catalyst was then reused for another same model reaction which furnishes **4a** with 85 % yield with the insignificant decline in catalytic activity. The reusability of the recovered VB<sub>1</sub> catalyst was tested twomore times which exhibited there is a slight change in conversion and yield of a product as shown in **Figure-2**.

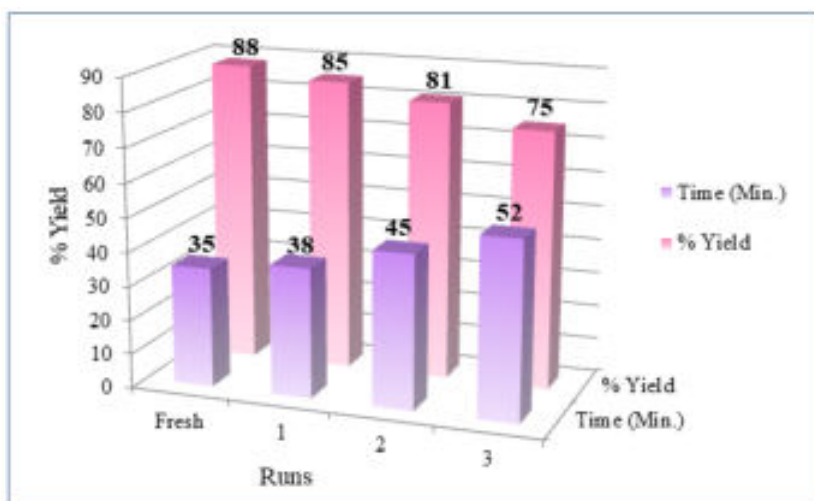


**Figure-2. Reusability of VB<sub>1</sub> catalyst in model reaction for the synthesis of 4a.**

The catalytic efficacy of the developed protocol for the synthesis of 5-aryl-4-phenyl-1,2,4-triazolidine-3-thiones has been compared with some previously reported catalysts presented in **Table-3**. The comparative study validates the use of VB<sub>1</sub> as one of the most effective catalysts for the one-pot three-component synthesis in an aqueous medium. All the prior methodologies based on using the other catalysts give the product of triazole with much longer times as compared to the current protocol.

**Table-3. A comparative catalytic efficiency of VB<sub>1</sub> in the synthesis of the model product 5-aryl-4-phenyl-1,2,4-triazolidine-3-thione (4a)**

Entry	Catalyst (mol %)	Solvent	Temperature (°C)	Time (min.)	Yield <sup>a</sup> (%)
1	[BZT] [AlCl <sub>4</sub> ] (25 mol %)	H <sub>2</sub> O	RT	40	84 <sup>[17]</sup>
2	HCl (3 mmole)	0.25 M, 12 mL HCl	RT	960	92 <sup>[18]</sup>
3	Sulphamic acid (20 %)	EtOH	Reflux	30	92 <sup>[19]</sup>
6	<b>VB<sub>1</sub></b>	<b>H<sub>2</sub>O</b>	<b>RT</b>	<b>35</b>	<b>88</b>

### 3.CONCLUSION

In conclusion, we accomplished a facile highly proficient, green synthetic protocol for a series of biologically relevant 5-aryl-4-phenyl-1,2,4-triazolidine-3-thione derivatives from a one-pot three-component reaction between phenyl isothiocyanate, hydrazine hydrate, and diversely substituted aromatic/hetero-aromatic aldehydes in presence of thiamine hydrochloride (VB<sub>1</sub>) as a biodegradable catalyst in aqueous medium at ambient conditions. Eco-benign and reusable catalysts, simple and energy-efficient processes, metal-free synthesis, high atom economy and cleaner reaction profiles are relevant to green credentials of the present protocol.

### REFERENCES

1. Naeimi, H., Foroughi, H. (2015) *New Journal of Chemistry*, 39, 1228-1236.
2. Singh, G., Kumar, M., Bhalla, V. (2018) *ACS Sustainable Chemistry & Engineering*, 9, 11466–11472.
3. Gordon, E. M., Gallop, M. A., Patel, D. V. (1996) *Accounts of Chemical Research*, 29, 144-154.
4. Alotaibi, M. A., Bakht, M. A., Alharthi, A. I., Geesi, M. H., Alshammari, M. B., Riadi, Y. (2020) *Sustainable Chemistry and Pharmacy*, 17, 100279.
5. Brahmachari, G. (2018) *Asian Journal of Organic Chemistry*, 7, 1982-2004.
6. Dhakane, V. D., Gholap, S. S., Deshmukh, U. P., Chavan, H. V., Bandgar, B. P. (2014) *Comptes Rendus Chimie*, 17, 431-436.
7. Lei, M., Ma, L., Hu, L. (2011) *Synthetic Communications*, 41, 1969-1976.
8. Fatma, S., Singh, P., Ankit, K., Shireen, P., Singh, M., Singh, J. (2013) *Tetrahedron Letters*, 54, 6732-6736.
9. Gholap, S., Gunjal, N. (2016) *Iranian Journal of Catalysis*, 6, 147-152.
10. Devi, J., Kalita, S. J., Deka, D. C. (2017) *Synthetic Communications*, 47, 1601-1609.
11. Ramesh, R., Lalitha, A. (2015) *RSC Advances*, 5, 51188-51192.
12. Zhang, H. Z., Damu, G. V., Cai, G. X., Zhou, C. H. (2014) *Organic Chemistry Frontiers*, 18, 359-406.
13. Singha, T., Singh, J., Naskar, A., Ghosh, T., Mondal, A., Kundu, M., Harwansh, R. K. (2012) *Indian Journal of Pharmaceutical Education and Research*, 46, 346.
14. Ramadan, S. K., Abou-Elmagd, W. S. I. (2018) *Synthetic Communications*, 48, 2409.



15. Peyton, L.R., Gallagher, S. (2015) *Drugs Today*, 51, 705.
16. Mojaddami, A., Sakhteman, A., Fereidoon nezhad, M., Faghih, Z., Najdian, A., Khabnadideh, S., Sadeghpour, H., Rezaei, Z. (2017) *Research in Pharmaceutical Sciences*, 12, 21.
17. Patil, M., Mhaldar, P., Mahadik, V., Pore, D. M. (2020) *Tetrahedron Letters*, 61, 152015.
18. Huggins, W. M., Minrovic, B. M., Corey, B. W., Jacobs, A. C., Melander, R. J., Sommer, R. D., Zurawski, D. V., Melander, C. (2017) *ACS Medicinal Chemistry Letters*, 8, 27.
19. Mane, M.M., Pore D.M. (2014) *Tetrahedron Letters*, 55, 6601-6604.

# Evaluation of Acute Toxic Effect of Gallic Acid Loaded Eudragit's 100 Nanoparticles on *Artemia Salina* Brine Shrimp Bioassay

Poournima S. Sankpal<sup>a,\*</sup>, Sachinkumar V. Patil<sup>a</sup>, Sayali S. Patil<sup>a</sup>

<sup>a</sup>Ashokrao Mane College of Pharmacy, Peth-Vadgaon, Kolhapur 416 112 (MS) India.

\*Corresponding author: poournima6@gmail.com

---

## ABSTRACT

Developing gallic acid nanoparticles and testing their *in vitro* cytotoxicity using a brine shrimp lethality assay were the goals of this study. (*Artemia salina*) In this study, we used the probe sonicator method to synthesize and characterize gallic acid nanoparticles using GMO, Poloxamer 188, and Eudragit S 100. Particle size, zeta potential, DSC, XRD, entrapment efficiency, loading content, and an *in-vitro* release studies were used to characterize the nanoparticles. Gallic acid was completely encapsulated, with an average size of 151.20 nm and a zeta potential of +18.2 mV. We may be able to conclude the conclusion from our research that our efforts will improve the development and production of gallic acid nanoparticles for the *Artemia salina* brine shrimp bioassay, where cytotoxicity was evaluated using the LC50 method. It was revealed that the gallic acid-loaded herbal nano formulation of brine shrimp was effective.

## KEYWORDS

Gallic acid, Eudragit S 100 nanoparticles.

.....

## 1. INTRODUCTION

These bioactive molecules have all been extensively studied for their antitussive, antioxidant, cardiac, gastro, neuroprotective, hypoglycemic, hypolipidemic, chemomodulator, and anticancer properties. Gallic acid (GA), a Phenolic molecule that is insoluble in water, is one of the important components that may help to the medical benefits [1]. Great efforts are being made in the current work to discover and develop nano formulation based on natural products, as well as to evaluate their *in-vitro* cytotoxic activity on brine shrimp lethality assay. The brine shrimp lethality test is a low-cost method and capable of detecting a wide range of bioactivity in crude extract. Many researchers have discovered that screening different chemical compounds found in various bioactivities investigations by the lethality of a test sample in a simple biological organism like the brine shrimp (*Artemia salina*) is a useful technique [2-4].

GA's pharmacokinetic parameters, such as its high particle size, low absorption, poor solubility, low bioavailability, and rapid elimination, have a significant impact on how well it is absorbed and developed by humans. Because gallic acid is unstable at high temperatures, there are substantial limitations to its use in various formulations to treat various disorders. In order to increase the effectiveness of Eudragit S 100 nanoparticles, a gallic acid loaded method was developed [5]. Nanoparticle approaches, such as polymeric nanoparticles, were successful in overcoming low solubility, higher stability, sharper size distribution, sustained and controlled release profiles, higher encapsulation efficiency for weakly water soluble agents, and can be effective in enhancing bioavailability with better targeting efficiency. Eudragit S 100 has been shown to transport a variety of hydrophilic and hydrophobic pharmaceuticals, while Poloxamer 188, a nonionic stabilizer approved by the US FDA, is employed in several formulations [6]. However, surface modification alters the properties of polymeric nanoparticles on their surfaces, and/or Eudragit S 100 is used as a polymer to enhance the pharmacokinetics of these colloidal carriers [7].

With the help of the innovative nanoparticulate technology Eudragit S 100, medications that have been enclosed in capsules can be preserved, stabilized, and delivered to the right targets. FTIR and UV spectroscopy were used to investigate the mechanism of gallic acid [8]. Based on the poloxamer and 188 Eudragit S 100 approaches described for preparation of nanoparticles, where no nanoformulations for the manufacture of gallic acid-loaded nanoparticles have been developed. In this study, we aimed to develop Eudragit S 100 nanoparticles loaded with gallic acid [9]. The solubility, stability, and bio-distribution of gallic acid biomolecule in the drug delivery system are frequently improved by gallic acid-loaded Eudragit S 100 nanoparticles, which also increases the efficacy of the medicine. Gallic acid can be designed as a drug delivery system since nanoparticle formation considerably enhances gallic acid absorption. Utilizing FT-IR, DSC, XRD, zeta potential, entrapment efficiency, loading efficiency, particle size, and other measurements, the improved formulation was assessed. Finally, release kinetic studies using a method for determining typical nanoparticle release were carried out.

In this study, we compared the gallic acid nanoformulations activity in a brine shrimp lethality experiment to its in vitro anti-cancer cytotoxicity. Chitosan nanoparticle cytotoxicity was applied to this bioassay for 12 hours, and different concentrations of 100–1000 ug/mL were required for different levels of activity. In order to investigate into the possible in-vitro cytotoxic effects of gallic acid nanoparticles, we developed herbal nanoparticles using biomolecule of gallic acid, a phenolic mostly present in amla fruit. The number of nauplii that survived and the percentage of mortality that were subjected to gallic acid nano formulation after 12 hours demonstrated significant viability in a dose-dependent manner. After 12 hours

of treatment, the LC50 of herbal nanoparticles was reported to be 196.16ug/ml. The brine shrimp lethality assay results revealed that the produced herbal nanoparticles have a higher antitumor potential, which is briefly discussed in this work.

## **2. MATERIAL AND METHODS**

### **2.1. Chemicals**

Poloxamer 188 and Eudragit S100 were gifted from BASF (Mumbai), Glyceryl Mono-Oleate (GMO) from Mohini organics Pvt. Ltd. (Mumbai) and rest of the solvents and chemicals were purchased from Himedia Laboratories and Research Lab (Mumbai). Gallic acid was purchased from Loba Chemie.,

### **2.2 Methods**

#### ***2.2.1 UV-Visible spectroscopy***

Sample was scanned by Shimadzu UV/Vis spectrophotometer and spectrum was recorded at  $\lambda$  max at 270 nm.

### **2.2 Formulation of nanoparticles**

#### ***2.2.1 Design of experiments and data analysis***

The generation of various significant data with fewer experiment runs and the assessment of the linear, quadratic, and interaction effects of the independent parameters on the responses are two benefits of response surface methodology over other statistical techniques based on the traditional one-variable-at-a-time method. As a result, the central composite design, which is used for determining independent components while allowing for a smaller number of tests using a block, was chosen for the experiment design. Using a factorial design to evaluate the effects of the analysis parameters, such as the concentrations of poloxamer 188 and Eudragit S 100, it was determined the impact of these changes on physicochemical attributes; On the response variables particle size (Y1) and zeta potential (Y2) of the produced GA-loaded Eudragit S 100 nanoparticles, the quantity of Eudragit S 100 (X1, 1.2 to 3.6 gm) and the amount of poloxamer 188 (X2, 0.05 to 0.15 gm)

#### ***2.2.2 Preparation of nanoparticles***

The Eudragit S 100 was used to produce nanoparticles of gallic acid using a probe sonicator and freeze-drying method. According to the factorial design, batch number five was developed for the nanoformulation. In molten 1.75 mL GMO, gallic acid (100 mg) was dissolved. A total of 12.5 mL of 0.1 % poloxamer 188 was added drop by drop and sonicated at 18 W for 3 minutes. A 2.4 % eudragit S 100 solution was added to the initial emulsion. To make the final nano emulsion, the emulsion was exposed to three cycles of probe sonicator at 18000 psi. A dialysis membrane was used to purify the water (molecular weight cutoff 12 kDa; Sigma Aldrich). To

achieve a fine powder of nanoparticles, the dialyzed product was freeze-dried for 48 hours with 2 % mannitol as the cryoprotectant. The white lyophilized product was then refrigerated at 4°C [10].

## 2.3 Characterization of nanoparticles

### 2.3.1 Particle size and charge measurements

The size and electrical charge of the particles were determined using dynamic light scattering and electrophoresis techniques [11-12].

### 2.3.2 FTIR spectroscopy

For the identification of functional groups contained in plant compounds, FTIR has shown to be a useful technique. Attenuated total reflection/Fourier transform infrared spectroscopic (ATR/FTIR) spectra was collected at room temperature by coupling ATR accessory to an FTIR spectrometer (Perkin Elmer, Spectrum 100) [11-12].

### 2.3.3 Differential scanning calorimetry (DSC)

Gallic acid, poloxamer 188, Eudragit S 100, physical mixes, and gallic acid nanoparticles were scanned using DSC Q10 equipment (TA Instruments, DE, USA) at 10°C/min and 50 mL/min flow rate [11-12].

### 2.3.4 X-ray diffraction analysis (XRD)

On a Bruker D8-Advance diffractometer (Bruker AXS Inc., Madison, WI, USA) with back groundless sample holders and operating at 40 kV and 30 mA, XRD graphs of gallic acid, poloxamer 188, Eudragit S 100, and gallic acid nanoparticles were recorded [11-12].

### 2.3.5 Determination of % entrapment efficiency and % drug loading

Entrapment efficiency has been described as an important characteristic since insufficient trapping contributes to the drug's first burst release, which may be attributed to the hydrophilicity of the Eudragit S 100 polymer [5]. Gallic acid-loaded nanoparticles (20 mg) were completely dissolved in 10 ml of DMSO. Before filtering, the resultant suspension was evaporated to remove any remaining solvent. The residue was then rinsed and diluted for 24 hours by gently shaking it at 37°C. The solution was then centrifuged at 16,000 g for 10 minutes, and the supernatant was collected. A portion of the supernatant (1 mL) was diluted in DMSO to make 10 mL, and the absorbance was measured at 270 nm using a UV spectrophotometer. The percentages of gallic acid encapsulated in nanoparticles (% EE) and (% LC) were calculated as follows: [13]

$$\begin{aligned}\% \text{ Efficiency of Entrapment} &= \frac{[\text{Drug}]_{\text{total}} - [\text{Drug}]_{\text{free}}}{[\text{Drug}]_{\text{total}}} \\ \% \text{ loading capacity} &= \frac{[\text{Drug}]_{\text{total}} - [\text{Drug}]_{\text{free}}}{[\text{Weight of nanoparticle}]_{\text{total}}}\end{aligned}$$

### **2.3.6 In-vitro release studies**

The drug release from gallic acid nanosuspension was performed using USP II Paddle apparatus at 100 rpm and  $37 \pm 0.2^\circ\text{C}$ ; saline phosphate buffer (200 ml; pH = 7.4) was used as the dissolution medium. Concisely, 20 mg of gallic acid loaded eudragit S 100 nanoparticles were suspended in saline phosphate buffer and placed in dialysis membrane with 10,000 Da cut off. Samples were done at 0.5, 1, 2, 3, 4, 5, 6, 8, and 12. It was removed from the dissolution medium at different intervals (3 ml) and replaced with the same amount of fresh dissolution medium and analyzed by UV spectrophotometer (Shimadzu UV/VIS) at 270 nm for the presence of drug [14-15].

## **2.4 In-vitro anticancer activity (cytotoxicity) by brine shrimp lethality bioassay**

### **2.4.1 Preparation of sea water**

For brine shrimp meals, dissolve crude sea salt 25g/L in distilled water and add dried Brewer's yeast 6 mg/L to this solution. Before using, it was filtered with filter paper [16].

### **2.4.2 Hatching of brine shrimp eggs**

The different chamber was filled with 2.0 L of sea water, and 40 mg of eggs were rinsed in water before being scattered into the darkened compartment. Phototropic nauplii were collected by capillary from the lighter side after 48 hours and used in the bioassay [17].

### **2.4.3 Bioassay**

Meyer et al. 1982 developed the technique for doing the bioassay experiment [18]. Ten of these shrimps were added to each sample vial containing 4.5 ml of brine solution after being counted in the capillary stem against a light background (specific volume brine and yeast suspension). In each experiment, 0.5 mL of sample solution was mixed with 4.5 mL of brine solution at the indicated quantities. 4.5 mL artificial sea water and 0.5 mL artificial sea water with 0.2 % DMSO water were added to the control vial. For each concentration, three replications were employed. Distilled water is used for the blank control. Survivors were counted after 24 hours using 3x magnifying glasses or against a lighted background, and the % deaths were calculated using a formula [19].

Percent mortality =  $(\text{Total naupii} - \text{Alive naupii}) / \text{Total naupii} \times 100$

The chronic LC<sub>50</sub>, or lethal concentration for 50% death after 24 hours of exposure, was calculated using the probit method as a measure of toxicity of the extract or fractions. Inactive substances have LC<sub>50</sub> values more than 1000 ppm [20].

### 3. RESULT AND DISCUSSION

#### 3.1 UV-Visible spectroscopy

Gallic acid solution was scanned by using UV/Vis spectrophotometer and absorbance was recorded at 270 nm [21].

#### 3.2 Formulation of nanoparticles using central composite design

The optimization objective of the study was to reduce particle size and zeta potential. The following processing parameters were found to be related to the optimum condition/central points (optimum) of the optimal combination regions: Eudragit S 100 (gm) = 2.4 and poloxamer 188 (gm) = 0.1. Using Design-Expert 11 software, the overlay plot obtained from the experiment work was statistically evaluated (Stat-Ease Inc., USA). The statistical accuracy of the polynomials was determined using ANOVA. Counter plots, 3D response surface graphs, normal probability, and perturbation plots were designed to investigate the interaction of independent and dependent components. The formulation aim is optimized using the in-range maximum, minimum, target, and none. Both numerical and graphical optimization approaches are used. The following **Table-1** shows the criteria for nanoparticle optimization. Because the values of the center point provided by the overlay plot matched batch F5, batch F5 was chosen as the best batch.

**Table-1. Summary of experimental design.**

Std., Run	Factor 1	Factor 2	Response 1	Response 2
	A: Eudragit S 100 (gm)	B: Poloxamer 188 (gm)	Particle Size (nm)	Zeta potential (mV)
1	1.2	0.05	145	18.2
2	1.2	0.10	147	22.3
3	1.2	0.15	151	24.2
4	2.4	0.05	151	24.5
<b>5</b>	<b>2.4</b>	<b>0.10</b>	<b>172</b>	<b>24.9</b>
6	2.4	0.15	182	28.1
7	3.6	0.05	199	28.6
8	3.6	0.10	207	30.6
9	3.6	0.15	211	31.0

**Figure-1** shows two regions: a yellow region indicating a design space area with possible response values, and a grey region describing an area where the answer did not satisfy the quality product standards. The ideal condition/central points of the

best combination regions (optimum) for the processing factors eudragit S 100 (mg) =2.4 % and poloxamer 188 (mg) = 0.1 %. These conditions were used to estimate the formulation of nanoparticles with (nm) = 218 and Zeta potential (mV) = 11.50. Batch F5 was chosen as the optimal batch because the values of the overlay plot's centre point matched batch F5.

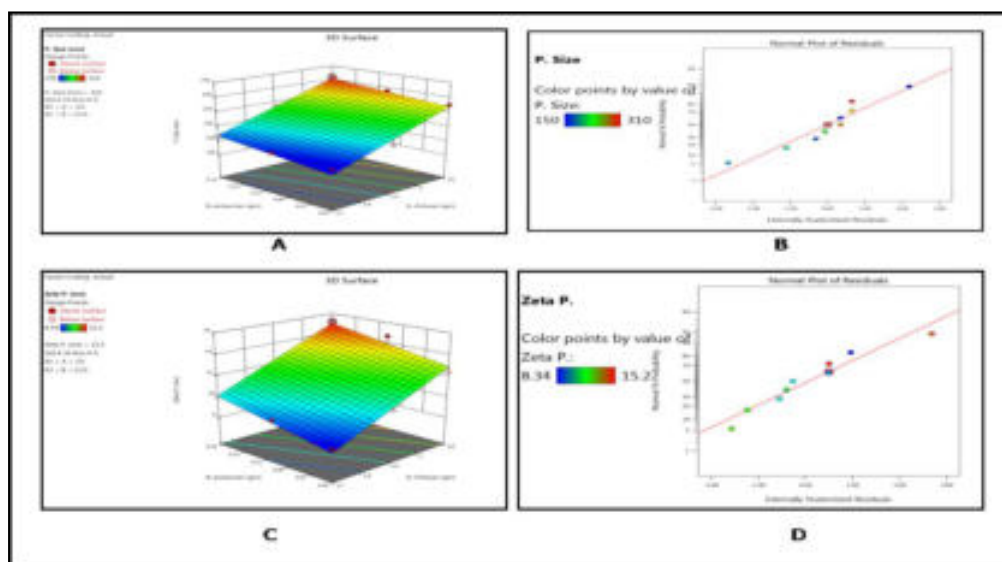


**Figure-1. Central composite models of (A) 3-D plot of particle size (B) Normal residual plot (C) 3-D plot of zeta potential (D) Normal residual plot.**

### 3.3 Characterization of gallic acid nanoparticles:

#### 3.3.1 Analysis of particle size and zeta potential

The concentrations of poloxamer (0.1%) and eudragit S 100 (2.4%) were chosen since greater concentrations of poloxamer (up to 0.15%) and eudragit S 100 (up to 3.6%) were found to affect particle size in increasing order [22]. Gallic acid-loaded eudragit S 100 nanoparticles had a mean diameter of 151.21 nm and a zeta potential of +18.2 mV.



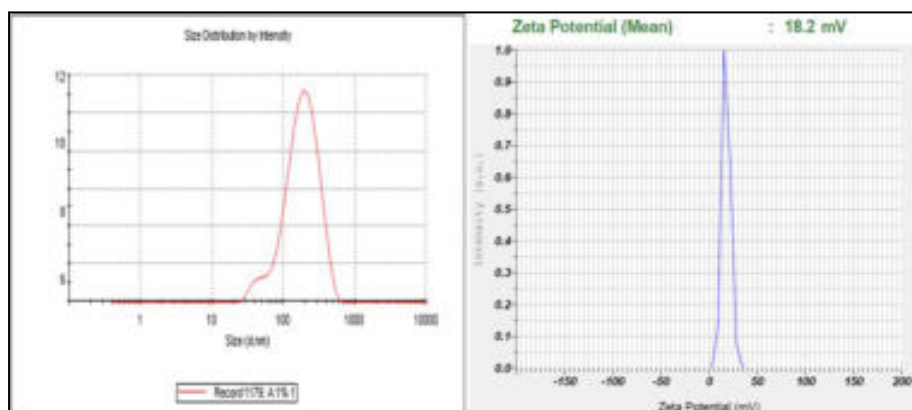


**Figure-2. Particle Size and Zeta Potential of nanoformulation.**

### **3.3.2 FTIR of nanoparticles**

Gallic acid's spectra show a broad band at  $3194.61\text{ cm}^{-1}$  due to OH stretching and hydrogen bonding between phenolic hydroxyl groups (**Figure-3A**). The COOH stretch/bend may be seen at  $1255.93\text{ cm}^{-1}$ . Aromatic ring stretching may be seen at  $1454.44\text{ cm}^{-1}$ . C-O has a stretch of  $1021.45\text{ cm}^{-1}$ . The OH stretching characteristic group of Eudragit S 100 is  $3285.15\text{ cm}^{-1}$ , and C- H stretching characteristic group is  $2875.66\text{ cm}^{-1}$ , as well as the amide CN stretching characteristic group is  $1415.23\text{ cm}^{-1}$  (**Figure-3B**). The bands at  $1150.54\text{ cm}^{-1}$  are for asymmetric stretching of the bond C-O-C and  $1062.04$  and  $1023.35\text{ cm}^{-1}$  are for vibrations involving the C-O bonds of primary alcohols, respectively. Poloxamer 188 carbon chain (**Figure-3C**) has aliphatic C-H stretching at  $2881.11\text{ cm}^{-1}$ , planar O-H bends at  $1365.12\text{ cm}^{-1}$  and  $1242.02\text{ cm}^{-1}$ , C-O stretch at  $1096.99\text{ cm}^{-1}$ , and  $\text{CH}=\text{CR}_2$  at  $840.46\text{ cm}^{-1}$ . GMO's C=O functionality was visible with a sharp peak at  $1738\text{ cm}^{-1}$  (**Figure-3D**) [23]. The O-H stretch of gallic acid was absent in the spectra of Gallic acid-loaded Eudragit S 100 nanoparticles (**Figure-3E**).

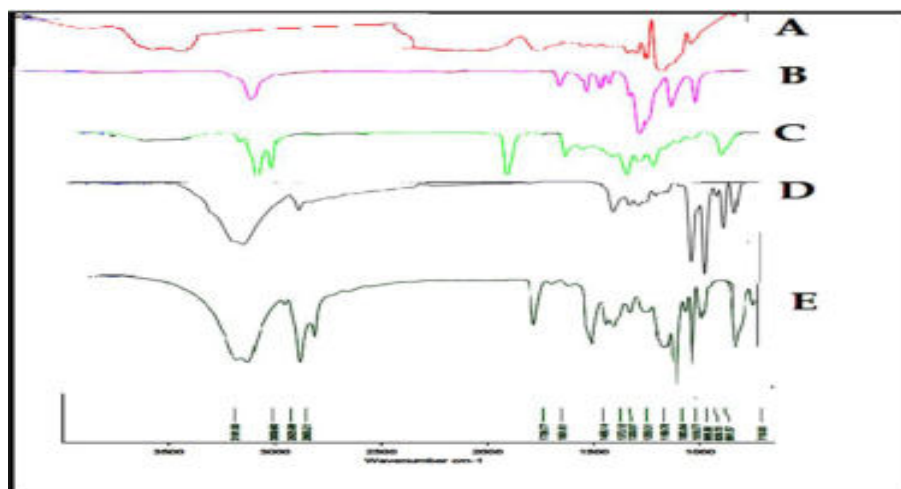


**Figure-3. FTIR Spectra of (A) Eudragit S 100, (B) Poloxamer 188, (C) GMO, (D) Gallic acid, (E) Gallic acid nanoformulation.**

### **3.3.3 Differential scanning calorimetry**

For gallic acid, a high endothermic peak was observed at 259.68°C, which corresponds to its melting point (**Figure-4A**). Another peak was seen at 91.73°C, which may have been caused by water evaporation and may have represented pure gallic acid in its crystalline form. The major endothermic peak, a pointed peak at 58.92°C, was seen when Poloxamer-188 (**Figure-4B**) melted. Eudragit S 100 thermogram showed a relatively broad endothermic peak at 84.37°C (**Figure-4C**). The thermogram of the physical mixture showed no changes; it is essentially a superimposition of the temperature profiles of the components, revealing that there was no interaction. (**Figure-4D**). On the other hand, the thermogram of nanoparticles (**Figure-4E**) the spectra of the gallic acid loaded Eudragit S 100 nanoparticles showed that O-H stretch of gallic acid was disappeared [24].

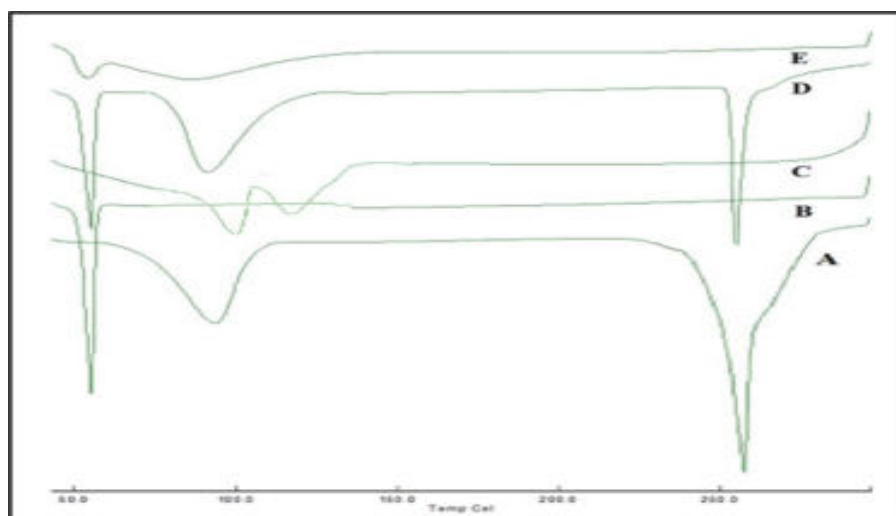


**Figure-4. DSC thermogram (A) Gallic acid, (B) Poloxamer-188, (C) Eudragit S 100, (D) Physical mixture, (E) Gallic acid nanoformulation.**

#### **3.3.4 X-Ray Diffracting studies (XRD)**

Powder XRD measurements show a crystalline peak of gallic acid and poloxamer 188, while Eudragit S 100 was present in an amorphous condition. Gallic acid has sharp peak at  $8^\circ$ ,  $16^\circ$ ,  $19^\circ$ ,  $33^\circ$ ,  $42^\circ$ , and  $43^\circ$  (**Figure-5A**). Poloxamer 188 has sharp peak at  $2\theta = 19^\circ$  and  $24^\circ$ . (**Figure-5B**) Eudragit S 100 usually has three XRD peaks, each of which corresponds to a different crystalline structure. The hydrated crystalline structure has two peaks at  $2\theta = 8$  and  $12^\circ$ , whereas the anhydrous crystalline structure has one peak at  $2\theta = 15^\circ$ . Eudragit S 100 also has a large peak at  $2\theta = 20^\circ$  due to the existence of an amorphous structure. At  $20^\circ$ , Eudragit S 100 corresponds to crystallographic planes (**Figure-5C**). A gallic acid nanoparticle peaks at (**Figure-5D**) with diffraction angle  $2\theta$  ( $10^\circ$ ,  $18^\circ$ ,  $21^\circ$ ,  $25^\circ$ ,  $36^\circ$ ,  $41^\circ$ ) when compared to pure forms in crystalline form. Gallic acid does not exist in crystalline form, as evidenced by the disappearance of significant diffraction peaks and the inability to distinguish the gallic acid's different peaks [22, 25].

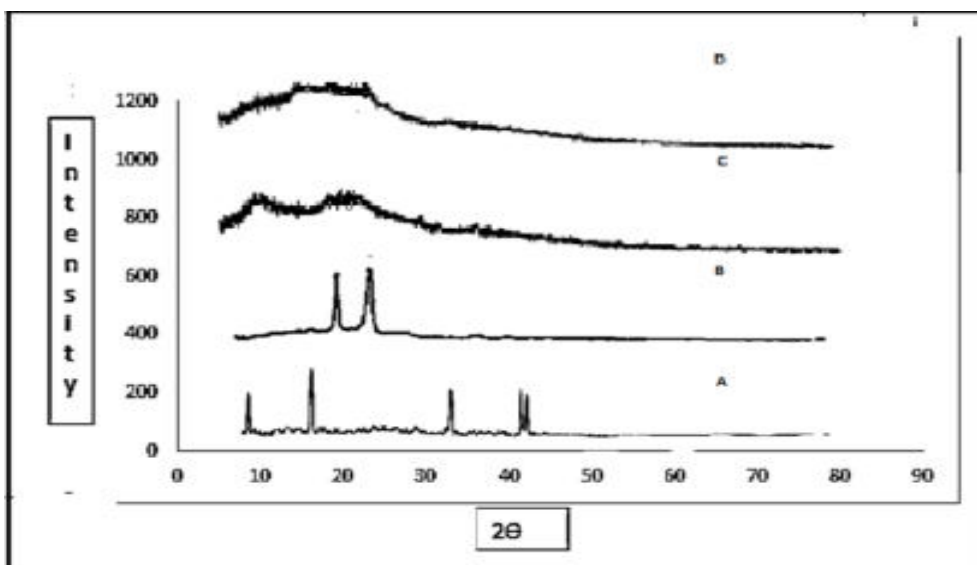


**Figure-5. XRD Pattern of (A) Gallic acid, (B) Poloxamer 188, (C) Eudragit S 100, (D) Gallic acid nanoformulation.**

### **3.3.5 Entrapment efficiency and loading content**

In nanoparticle formulation, Eudragit S 100 and poloxamer 188 have an effect on the EE and LC of the formulation. Increasing the concentration of Eudragit S 100 and poloxamer 188 increased the EE and LC formulation until that concentration was obtained, after which the EE and LC formulation decreased. The crystalline form of nanoparticles with entrapment efficiency (%) of 76.80% and a loading capacity (%) of 3.10 % [26].

### **3.3.6 In-vitro release studies**

To analyze drug release behavior further, various kinetic models, such as zero order, first order, second order were used [27]. As first order models, Higuchi's model, Hixson-Crowell cube root rule, and Peppas's exponential model were used [28]. The drug release is non-Fickian (anomalous) if the value of  $n$  is between 0.5 and 1.0, whereas  $n = 0.5$  shows Fickian diffusion and  $n$  values greater than 1 indicate case II transport. **(Figure-6)** At pH 7.4, gallic acid was released from nanoparticles using Peppas model and zero order release case II transport ( $n = 2.09$ )

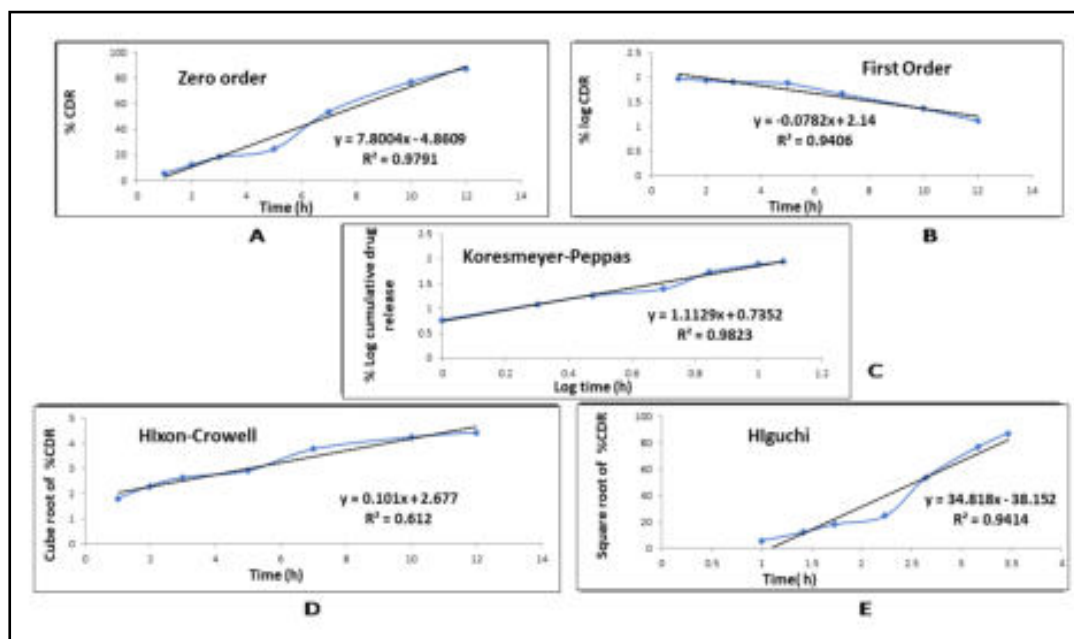


**Figure-6. *In-vitro* drug release plots in different kinetic models (A) Zero order (B) First order (C) Koresmeyer Peppas (D) Hixon Crowell (E) Higuchi.**

Gallic acid *in-vitro* release pattern formulation revealed improved drug release after 8 hours and 88.16 % after 12 hours in a sustained manner. For Higuchi  $y=26.006x-22.46$   $R^2=0.965$ , the linearity for zero order  $y=4.148x+11.39$   $R^2=0.807$ , for first order  $y=-0.048x+2.009$   $R^2=0.886$ , and for first order  $y=-0.048x+2.009$   $R^2=0.886$ .  $R^2=0.955$ , Hixson Crowell  $y=0.182x-0.681$ , The best linearity connection in K-Peppas was discovered to be  $y=1.032x+0747$ ,  $R^2=0.965$ , all data in **Table-2**.

**Table-2. *In-vitro* drug releases in different kinetic models.**

Kine tic Mod els	Zero order			First order			Higuchi	Hixon- Crowell
Sr. No.	Time (h)	%CR	Log (time)	Log (%CR)	% DR Rem.	Log % DR	SQRT time	Cube Root of DR
1	1	6.75	0	0.8293	93.25	1.96965	1	1.88988
2	2	13.08	0.301	1.1166	86.92	1.93912	1.41421	2.35615

3	3	19.21	0.477	1.1835	80.79	1.90736	1.73205	2.6782
4	5	26.46	0.698	1.4225	73.54	1.86652	2.23607	2.97987
5	7	55.56	0.845	1.7447	44.44	1.64777	2.64575	3.81582
6	10	77.81	1	1.8910	22.19	1.34616	3.16228	4.26919
7	12	89.12	1.079	1.9499	10.88	1.03663	3.4641	4.46675

#### 4. ASSESSMENT OF BRINE SHRIMP ASSAY

The brine shrimp lethality assay (BSLA) is a low-cost bioassay which can be used to determine the efficacy of phytochemicals in herbal micro formulations. In this investigation, the quantity of lethality was shown to be proportional to concentration of gallic acid loaded nanoparticles. After 24 hours of observation, all of the shrimp in the control group survived. Despite this, the largest mortalities were seen at concentrations of 1000 g/mL and the lowest mortalities at values of 1 g/mL. Shrimps began to die after 8 hours in higher concentrations of nanoformulation, and by 24 hours, all of the shrimp had starved to death. The lethality concentration (LC50) was calculated using probit analysis. The LC50 values were calculated by plotting the concentration against the death percentage. Gallic acid-loaded nanoparticles destroyed brine shrimps with a lethal dose of 196.16 µg. (**Table-3**).

**Table-3. Results of Brine Shrimp Assay.**

Drugs	Conc. of extract	Total no. shrimps used/tube	Shrimp Survived			Total No. of Shrimp Survived	Mortality (%)	LC <sub>50</sub> (µg)
			T1	T2	T3			
Nanoformulation	Control	10	10	10	10	30		195.86
	100 µg/ml		5	4	3	12	60	
	200 µg/ml		2	1	3	06	80	
	400 µg/ml		1	0	0	01	96.67	
	800 µg/ml		1	1	0	02	93.33	
	1000 µg/ml		0	0	0	00	100	

The results show that herbal nanoformulations of gallic acid have cytotoxic effects, showing that they can be used in conventional medicine.

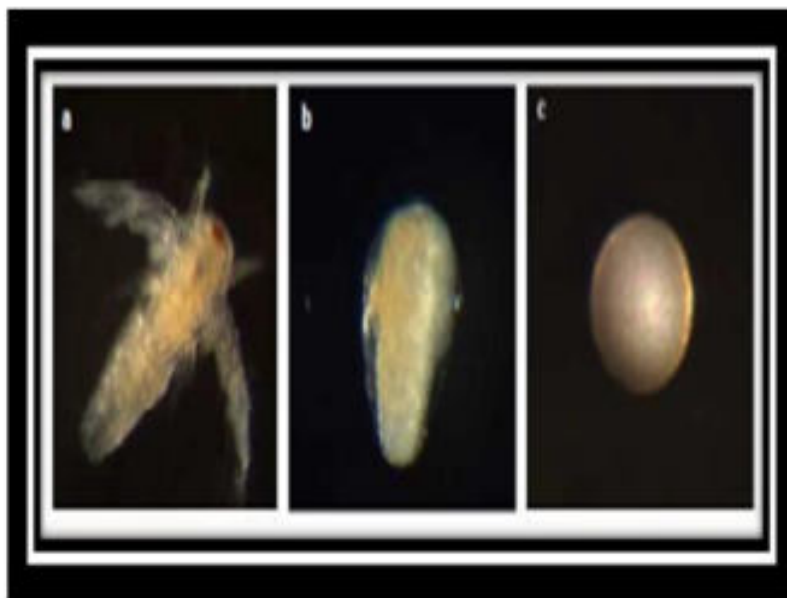


**Figure-7. Images of fully grown brine shrimps.**

## **5. CONCLUSION**

The phenolic compound (gallic acid) may be one of the important constituent in nanoformulation that contribute to the mechanism of cytotoxic action against brine shrimp in *in-vitro* testing. Although BSLA is insufficient for determining the mechanism of action of bioactive chemicals in herbal nanoformulation, it is extremely valuable for giving a preliminary screening that can be followed up with a more accurate bioassay. Special findings associated with brine shrimp bioassay included model hydrophobic gallic acid biomolecule in nanoformulation with nanoparticle size range, with positive charge, and sustained *in-vitro* releases from nanoparticles, especially in a wide pH range.

As a result, new nanoformulation based on natural products has been found to have a desired effect on brine shrimp lethality assays; hence, they have potential therapeutic anticancer biomolecule. More research is needed to determine the mechanism by which gallic acid nanoparticles exert their anticancer effect. Based on our findings, we may conclude that our study will make it easier to design, and manufacture nanoparticles for the protection and long-term release of gallic acid biomolecule, especially in the brine shrimp bioassay. Gallic acid with Eudragit S 100 polymer had no chemical interaction, according to FT-IR, DSC and XRD investigations.

The physicochemical characteristics of gallic acid have been shown to be changed by a nanoparticle system composed of polymer and stabilizer to generate Glyceryl monooleate/Eudragit S 100 nanostructures. As a result, extensive research has been done to discover and develop novel nanoformulation based on natural biomolecule, and the suggested carrier system may be useful in promoting gallic acid to the cancer activity.

## DECLARATION OF INTEREST

There are no conflicts of interest reported by the authors. This article's content and writing are entirely in the hands of the writers.

## ACKNOWLEDGEMENT

The author(s) express their deep sense of gratitude towards Ashokrao Mane College of Pharmacy, (Peth Vadgaon, Kolhapur, Maharashtra, (India)) for the provision of obligatory facilities to carry out present research work. Dr. Riyaz Ali M. Osmani, Department of Biosciences and Bioengineering (BSBE), Indian Institute of Technology Bombay (IITB), Mumbai, is gratefully acknowledged for his outstanding contributions and constructive ideas.

## REFERENCES

1. Abdou, E. M., Masoud, M. M. (2018) Pharmaceutical Development and Technology, 23, 55-66.
2. Arumugam, D.G., Sivaji, S., Dhandapani, K.V., Nookala, S, Ranganathan, B. (2019) Biocatalysis and agricultural biotechnology, 19, 101132.
3. Kachenton, S., Whangpurikul, V., Kangwanransan, N., Tansatit, T., Jiraungkoorskul, W. (2018) International Journal of Nanoscience, 17, 1850007.
4. Ates, M., Daniels, J., Arslan, Z., Farah, I.O., Rivera, H. F. (2013) Environmental science: Processes & impacts, 15, 225-33.
5. Badran, M. M., Harisa, G. I., AlQahtani, S. A., Alanazi, F. K., Zoheir, K. M. (2016) Journal of Drug Delivery Science and Technology, 32, 1-9.
6. Ahmad, N., Ahmad, R., Ahmad, F.J., Ahmad, W, Alam, M.A., Amir, M. (2020) Saudi Journal of Biological Sciences, 27, 500-17.
7. Dumortier, G., Grossiord, J. L., Agnely, F., Chaumeil, J. C. (2006) Pharmaceutical research, 23, 2709-28.
8. Caruso, D., Colombo, R., Patelli, R., Giavarini, F., Galli, G. (2000) Journal of Agricultural and Food Chemistry, 48, 1182-5.



9. Sagar, S., Reddy, M. S., Nanjwade, B. K., Srivani, M., Sughandi, M. (2018) American Journal of PharmTech Research, 8, 1-18.
10. Pandit, A. A., Dash, A. K. (2011) Nanomedicine, 6, 1397-412.
11. Alves, A., Mainardes, R.M., Khalil N.M. (2016) Materials Science and Engineering: C, 60, 126-34.
12. Rajasree, P., Paul, W., Sharma, C.P., Osmani, RAM., Hani, U., Srivastava, A. (2018) Journal of Drug Delivery Science and Technology, 46, 302-11.
13. Patil, P., Killedar, S. (2021) Journal of Drug Delivery Science and Technology, 63, 102523.
14. Agarwal, D., Ranawat, M., Chauhan, C., Kamble, R. (2013) Journal of drug delivery and Therapeutics, 3, 215-22.
15. Patil, P., Killedar, S., Chitosan. (2021) Heliyon X, 7, 6526.
16. Supraja, N., Prasad, T., Gandhi, A. D., Anbumani, D., Kavitha, P., Babujanarthanam, R. (2018) Biochemistry and Biophysics Reports, 14, 69-77.
17. Kachenton, S., Whangpurikul, V., Kangwanransan, N., Tansatit, T., Jiraungkoorskul, W. (2018) International Journal of Nanoscience, 17, 1850007.
18. Meyer, B., Ferrigni, N., Putnam, J., Jacobsen, L., Nichols, D., McLaughlin, J.L. (1982) Planta Medica, 45, 31-4.
19. Hnamte, S., Kaviyarasu, K., Siddhardha, B. In Evaluation of Toxicity of Nanoparticles Using Brine Shrimp, edited by Siddhardha, B., Dyavaiah, M., Kasinathan, K. Springer, Singapore (2020) pp. 15.
20. Kumar, P., Selvi, S. S., Praba, A., Selvaraj, M., Rani, L. M., Suganthi, P. (2012) Digest Journal of Nanomaterials and Biostructures, 7, 1447-55.
21. Itoh, N., Katsube, Y., Yamamoto, K., Nakajima, N., Yoshida, K. (2007) Tetrahedron, 63, 9488-92.
22. Yusuf, H., Rahmawati, R. A., Syamsur., Rijal, M. A., Isadiartuti, D. (2021) Future Science OA, 7, FSO677.
23. Ashokkumar, R., Ramaswamy, M. (2014) International journal of Current Microbiology and applied Sciences, 3, 395-406.
24. Zielińska, A., Carreiró, F., Oliveira, A. M., Neves, A., Pires, B., Venkatesh, D. N. (2020) Molecules, 25, 3731.
25. Lamarra, J., Rivero, S., Pinotti, A. (2016) Materials Science and Engineering C, 67, 717-26.
26. Jena, G. K. (2017) Asian Journal of Pharmaceutical Research, 11, 3.
27. Prasad, G., Prabhu, S. (2013) International Journal of Pharmacology & Biological Sciences, 7, 2.
28. Patil, P., Killedar, S. (2021) Journal of Pharmaceutical Innovation, 6, 1-14.

# Surface Modifications of Binder Free ZnO Nanorod Thin Films through Cds Quantum Dots for Dye Sensitized Solar Cells

Krantiveer V. More<sup>a</sup>, Anant G. Dhodamani<sup>a</sup>, Sajid B. Mullani<sup>a</sup>,  
Tukaram D. Dongale<sup>b</sup>, Prakash S. Pawar<sup>a</sup>, Satish M. Patil<sup>c</sup>, Sunil J. Kadam<sup>d</sup>,  
Sagar D. Delekar<sup>\*,a</sup>

<sup>a</sup>Department of Chemistry, Shivaji University, Kolhapur 416 004 (MS) India.

<sup>b</sup>School of Nanoscience and Biotechnology, Shivaji University, Kolhapur 416 004 (MS) India.

<sup>c</sup>Department of Chemistry, Karmaveer Hire Arts, Science, Commerce and Education College, Gargoti, Kolhapur 416 209 (MS) India.

<sup>d</sup>Bharati Vidyapeeth Deemed University College of Engineering, Pune 411 046 (MS) India.

\*Corresponding author: sdd\_chem@unishivaji.ac.in

---

## ABSTRACT

*In this work, zinc oxide (ZnO) nanorods (NRs) were synthesized by using simple sol-gel method at room temperature and used as photoanode material for the fabrication of sandwich type sensitized solar cell device. The morphologies and average particle size were studied by scanning electron microscopy (SEM) and transmission electron microscopy (TEM) respectively. Initially binder free ZnO NRs thin film was prepared and thereafter incorporated with CdS quantum dots (QDs). After modification of ZnO NRs with CdS QDs the structural and optoelectronic properties of ZnO NRs are different. Modified ZnO NRs-CdS QDs photoanode was sensitized with N719 dye. Optical study reveals that sensitization of CdS QDs on to ZnO NRs led to red-shift of the material, while absorbed N719 dye molecule further enhances the visible light which can effectively increases the overall efficiency of solar device. It was observed that the only N719 sensitized ZnO NRs (ZnO-N719) device show poor solar cell performance than CdS QDs modified ZnO-N719 device. This hybrid (ZnO-CdS QDs -N719 dye) solar cell led to higher solar cell parameters under AM 1.5G of 100 mW/cm<sup>2</sup> intensity.*

## KEYWORDS

*Quantum dot, Hybrid photoanode, Conversion efficiency, Binder free, Solar cell.*

.....

## 1. INTRODUCTION

Nowadays, metal-oxide based sensitized solar cells (SSCs) have received considerable attention due to their appealing properties and conceptual similarities with dye-sensitized solar cells (DSSCs) [1-3]. To achieve maximum efficiency in SSCs is still challenging task as compared to DSSCs or other solar devices [4-5], which is due to the low light absorption and improper charge transport in SSCs.

Therefore different alternative methods are used to construct promising next generation of solar cell. Recently different metal oxides are considered promising host material for solar device fabrication, among that zinc oxide (ZnO) is suggested to be an excellent alternative for titanium dioxide (TiO<sub>2</sub>) due to several similar properties of TiO<sub>2</sub> nanoparticles (NPs) [6]. Although the conduction band edge of both materials is located at approximately the same level; but the electron mobility of ZnO is much higher than TiO<sub>2</sub> indicating that the nanostructured (NS) ZnO is a good candidate as an electron acceptor and transport material for sensitized solar cell application [7]. Moreover, easy synthesis and processing of ZnO nanoelectrode makes it more advantageous [8]. Additionally, as compared to overall conversion efficiency of ZnO based DSSCs are still low due to its complexation with dye molecules, which hampers electron injection ability [9-12]. To overcome this issue and further improvement in electron injection efficiency there is need to modify the surface of ZnO. From literature it is seen that, the Ho et. al. modified ZnO nanorods (NRs) through Au NPs to improve the performance of DSSCs, but it is observed that after modification of ZnO NRs there is decrease in surfaces area and it affected on the overall efficiency of DSSCs [13]. Further, Yahong Xie coated thioacetamide on the surface of ZnO to control the reduction reaction between ZnO and dyes for highly efficient DSSCs. Importantly, it was noted that the thioacetamide worked as a surface modifier and not as sensitizer as well as observed efficiency is not up to the mark [8]. Hence, there is need of surface modification of ZnO with different materials for different applications.

In present investigation, the surface of ZnO was modified with CdS QDs which acted as surface modifying agent as well as sensitizer and which helps to boost the overall efficiency of solar device. However, efficient conversion of solar energy to electrical energy is depends upon the role of sensitizer, morphology of photo-anodic material and wide coverage of visible light spectrum and other parameters [14-16]. Considering the nature of semiconductor nanocrystal low-cost, stable ternary hybrid structure is developed a for QDDSSCs. In this type of CdS QDs were incorporated on binder free ZnO NRs thin films. The CdS QDs not only modify the surface area of ZnO but also extend the region from UV to Visible and it improve the overall efficiency of solar cell [17]. After sensitization of CdS QDs the N719 dye molecule anchored on film. The N719 dye molecules can be very useful in order to achieve both broadening of optical absorption region and increasing the absolute loading of absorbing media on the semiconductor [2,18]. Due to co-sensitized effect QDs and dye molecule affecting the overall photovoltaic parameters and increases the efficiency of co-sensitized solar device. For signally sensitized solar device we observed near to 0.86% efficiency, but as move from co-sensitized solar device getting almost double efficiency (2.15%) under one sun irradiation (air mass 1.5 G).

## 2. EXPERIMENTAL SECTION

### 2.1 Materials

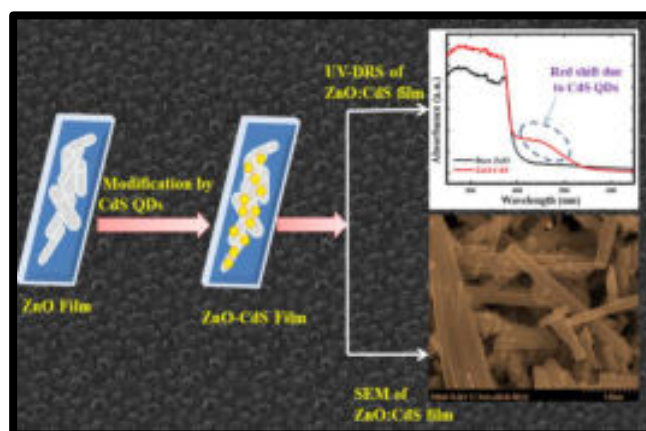
The fluorine doped tin oxide (FTO, Sheet resistance = 8-10  $\Omega$ ) glass was used for depositing bare ZnO NRs and considered as optically transparent electrode (OTE). The various AR grade chemicals such as, 3-mercaptopropionic acid (3-MPA, 98.00%), cadmium chloride monohydrate ( $\text{CdCl}_2 \cdot \text{H}_2\text{O}$ , 98.00%), sodium sulfide ( $\text{Na}_2\text{S}$ ), zinc acetate ( $\text{Zn}(\text{CH}_3\text{CO}_2)_2$ ), TritonX-100, ethylene glycol ( $(\text{CH}_2\text{OH})_2$ ), etc were purchased from Sigma-Aldrich.

### 2.2 Synthesis of ZnO Nanorods

Initially 100 mL zinc acetate was stirred at room temperature by slowly adding 2M ammonia solution still to obtain complete clear solution. Then after 5 mL of ethylene glycol and 5 mL TritonX-100 added in this solution and heated this whole solution at 70°C to 80°C with stirring up to getting white precipitate. The mixture is cooled to room temperature, centrifuged and washed with ethanol. The powder is dried and calcinated in at 450°C for 4 h. and used this powder for different characterizations.

### 2.3 Surface Modification of ZnO by CdS QDs and Device Fabrication with N719 dye

In ultrasonic bath, initially FTO substrates were cleaned using detergent solution for 30 min. and then rinsed with double distilled water. Again, it is rinsed with acetone and dried at 110°C for 30 min in electric oven. These substrates were used for deposition of ZnO NRs by using doctor-blade technique. In this protocol, ZnO paste was prepared by sonication of the ZnO NRs in ethanol solution and continuously stirred to get gel and this paste is deposited on surface of FTO. Then the prepared ZnO films were sintered at 450°C for 30 min and cooled naturally to room temperature. Subsequently, capped CdS QDs were deposited on ZnO films by using spin coater. Then, these modified ZnO -CdS films were rinsed with water and dried in oven at 110°C for 15 min. After sensitization of CdS QDs surface of ZnO NRs becomes rough (**Scheme 1**). Finally, the N719 dye were anchored on surface of modified ZnO:CdS QDs film by dipping films into N719 dye solution for 24 hrs. Then the electrodes were washed with equimolar mixture of tetra-butyl alcohol and acetonitrile (1:1 ratio) for removing the free dye molecules and considered as a photoanode. To design sandwich solar device of ZnO:CdS:N719 dye is used as a working electrode and platinum coated ITO as a counter electrode are pressed through Surlyn sheet and put in electric oven at 110°C. After proper binding of device electrolyte is inserted through counter electrode and whole device is placed in vacuum for the electrolyte filling on surface of ZnO:CdS:N719 electrode.

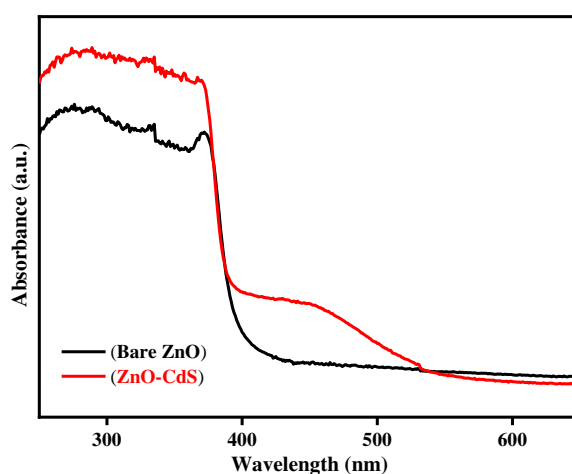


**Scheme 1. Surface modification of ZnO NRs through CdS QDs.**

### 3. RESULTS AND DISCUSSION

The prepared bare nanomaterials and their composites as well as fabricated devices are characterized by various characterization tools. In order to determine the optical properties of the nanomaterials UV-Vis-DRS spectroscopy is used with 200 to 800 nm wavelength range. X-ray diffractometer is used to analyse crystallite size and phase purity. Morphology of the ZnO NRs is determined by using scanning electron microscopy. After fabrication of sandwich solar devices, the photovoltaic measurement is carried out under solar simulator.

#### 3.1 Optical Absorption Study



**(a)**

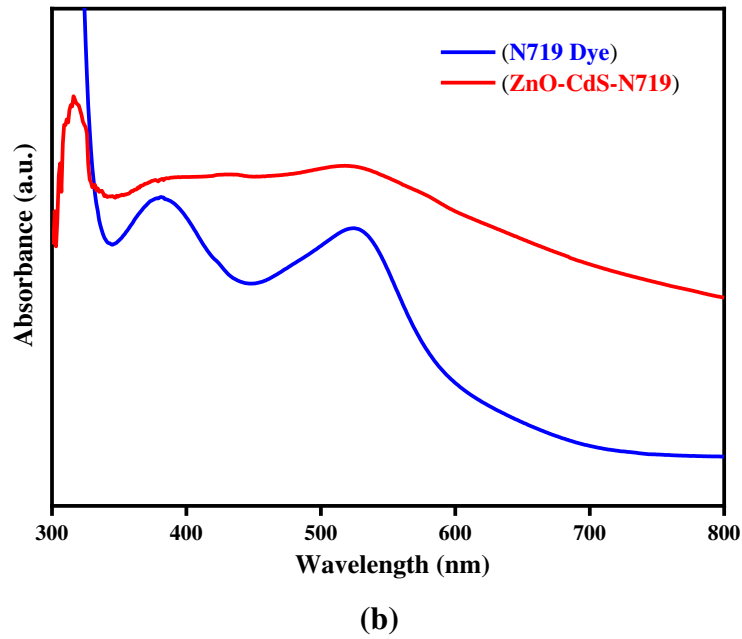
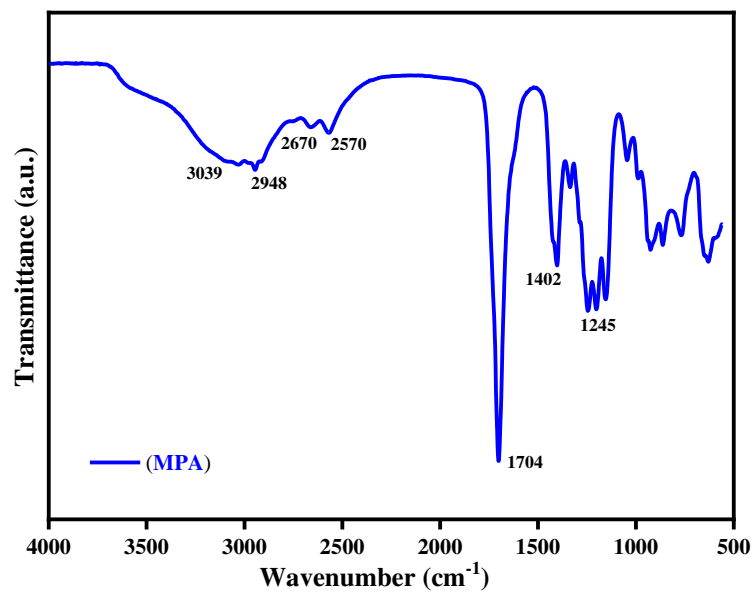


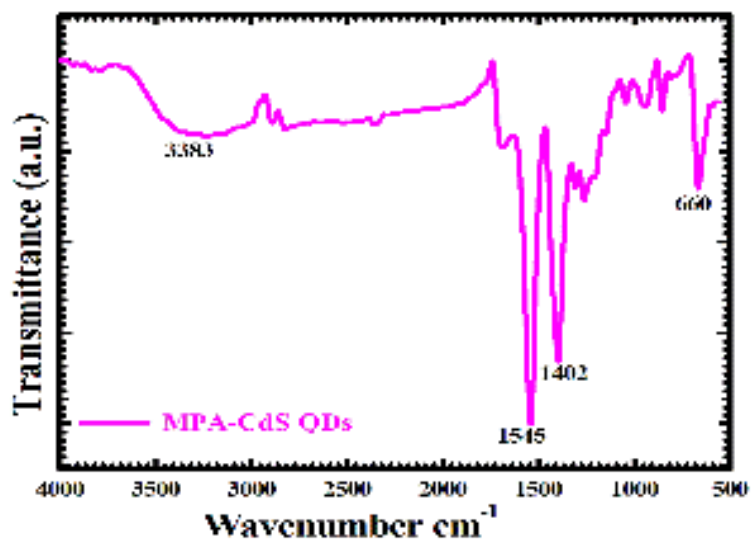
**Figure-1. (a) UV–Vis–DRS of bare ZnO, CdS sensitized ZnO film and (b) N719 dye and of ZnO:CdS:N719 film.**

The optical properties of the bare ZnO and CdS sensitized ZnO NRs are analyzed by using UV–Vis diffuse reflectance spectroscopy (DRS), the observed spectra are presented in **Figure-1**. From DRS spectra it is clear that the ZnO NRs shows absorption at 390 nm and obtained band-gap value of 3.17 eV. In the case of bare ZnO, the spectral curve does not display any significant deviation. However, in case of ZnO:CdS film, the absorption edge shows higher absorption than that of bare ZnO indicating the influence of CdS QDs (**Figure-1a**) in the binary composite [19]. The DRS spectra of ternary nanocomposites show a broad visible region, due to N719 dye (**Figure-1b**) [20]. Therefore, existence of N719 affects the optical properties of the ternary nanocomposites and is responsible for the red shift in the absorption spectrum. This improved absorption in the visible wavelength region results in the generation of abundant electron–hole pairs in the ZnO:CdS and ZnO:N719 based device under UV-visible illumination, which can lead to greater photo-current activity.

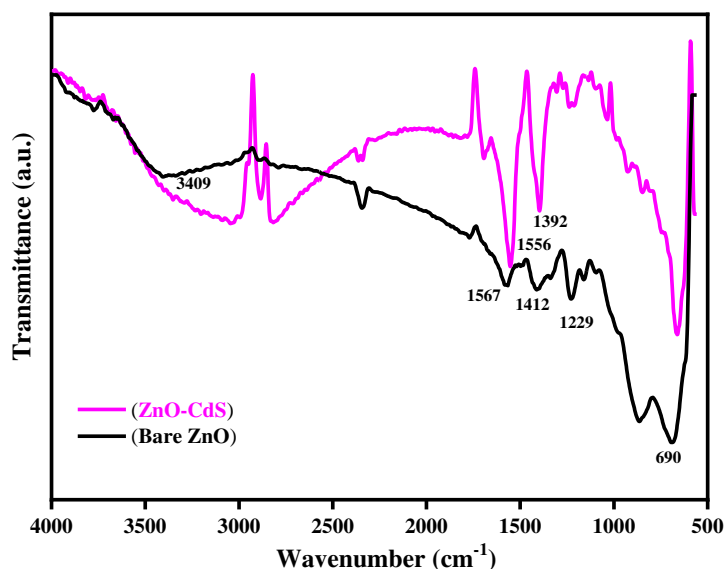
### 3.2 FTIR analysis



a)



b)



c)

**Figure-2. a) FTIR spectra of bare MPA, b) MPA capped CdS QDs and c) bare ZnO and CdS sensitized ZnO thin film.**

**Figure-2** presents FTIR pattern of bare MPA, MPA capped CdS QDs and bare ZnO NRs as well as CdS QDs sensitized ZnO NRs. For MPA (fig.2a) the bands observed at  $\sim 3400\text{--}3000\text{ cm}^{-1}$ ,  $\sim 2948\text{ cm}^{-1}$ ,  $\sim 2570\text{ cm}^{-1}$ ,  $\sim 1704\text{ cm}^{-1}$ ,  $\sim 1402\text{ cm}^{-1}$  are due to stretching vibrations of functional moieties such as -OH, -CH<sub>2</sub>, S-H, C=O and C-O, respectively. In addition, a small band at  $\sim 2670\text{ cm}^{-1}$  is due to bending vibration of -OH. However, in FTIR pattern of MPA capped CdS QDs (**Figure-2b**), the stretching band of carboxylic O-H group is disappeared due to its deprotonation; while the peak position of C=O group is shifted from  $1704\text{ cm}^{-1}$  to  $1545\text{ cm}^{-1}$  [21]. In addition, the stretching band of S-H is also not observed because of its high pK<sub>a</sub> value; which reveals that the interaction of sulfhydryl moieties of MPA with Cd<sup>2+</sup> ions and hence, the co-ordination between the different moieties avoids the deprotonation of the sulfhydryl group of MPA [22].

Similarly, in FTIR spectra of bare ZnO NRs, the broad absorption band at  $\sim 3400\text{--}3000\text{ cm}^{-1}$  and  $\sim 1400\text{--}1500\text{ cm}^{-1}$  due to O-H stretching and deformation of C-OH groups of water molecules, respectively. Zn-O bond stretching vibrations appears at  $690\text{ cm}^{-1}$ . However, ZnO:CdS composites also shows O-H stretching vibrations in the range of  $3000\text{--}3500\text{ cm}^{-1}$  range while, Zn-O between  $500$  and  $600\text{ cm}^{-1}$ . The peak at  $1392\text{ cm}^{-1}$  in the binary composite is assigned to C-O bending vibration. From the FTIR spectra of ZnO:CdS composite it is clear that; in composites the characteristic peaks of oxygen containing functional groups



particularly at  $1704\text{ cm}^{-1}$  are weakened and the O–H stretching peak decreases. This is mainly attributed to the loss of oxygen containing functional groups. Overall study reveals that, surface of ZnO NRs are covered through CdS QDs.

### 3.3 XRD analysis of ZnO: CdS thin film`

In order to determine crystallinity, phase of the ZnO NRs, CdS and their composites, X-ray diffraction (XRD) technique is used. Typical XRD pattern of the synthesized ZnO NRs, ZnO:CdS composites are shown in **Figure-3**. The various reflections are appeared at  $2\theta$  values of 31.86, 34.58, 36.32, 47.63, 56.71, 62.86, 68.08, 69.26, and 76.88, with corresponding reflection of (100), (002), (101), (102), (110), (103), (112), (201), and (202) respectively. All these peaks are indexed and these are well matches with wurtzite (hexagonal) structure of ZnO (JCPDS card no. 36-1451). Furthermore, absence of any characteristic impurity peaks indicates formation of high quality ZnO NRs.

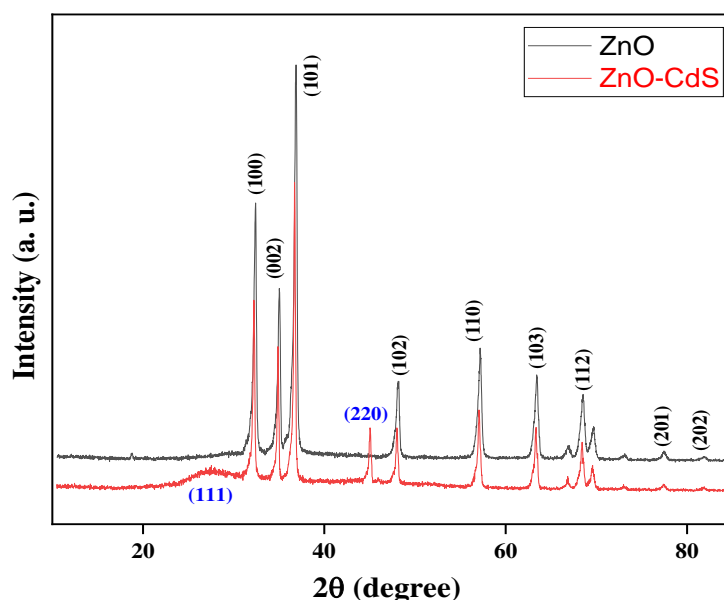


**Figure-3. XRD patterns of Bare ZnO NRs and CdS QDs sensitized ZnO thin film.**

Interestingly, ZnO:CdS composites shows an additional peak at  $27.42^\circ$ ,  $44.86^\circ$  which is due to presence of (111) and (220) crystal plane of CdS QDs on ZnO NRs respectively; which clearly indicate that the proper depositions of CdS QDs take place on surface of ZnO NRs. The crystallite size of bare ZnO NRs and ZnO:CdS composites determined from the Scherrer's equation and is shown in **Table-1**. Moreover, after sensitization the crystallite size of ZnO:CdS is decreases. The

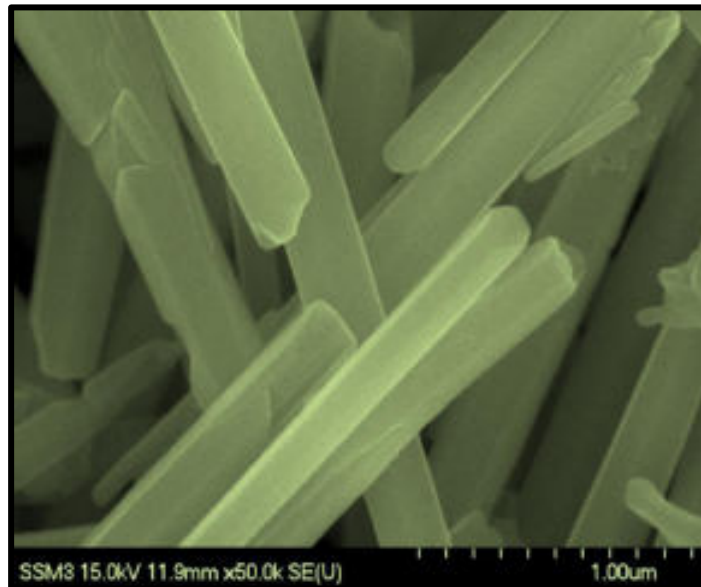
appearing of CdS QDs on ZnO surface is further supported by XPS and SEM analysis.

**Table-1. Structural parameter of ZnO:CdS thin film.**

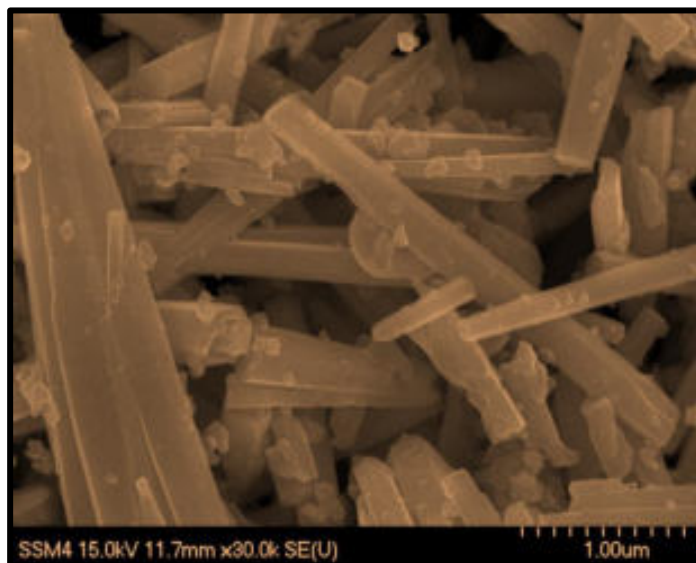
Sample	(hkl plane)	d value		Parameters			Dominance Crystal Structure
		observe d	a (Å)	c (Å)	V(Å <sup>3</sup> )	Cry. size (nm)	
Bare ZnO	(101)	2.471					Wurtzite
	(002)	2.590	3.23	5.18	54.04	09.34	Hexagonal
	(110)	1.621					
Bare CdS	(111)	2.38					
	(220)	2.07	5.85	--	200.20	1.89	Cubic
	(311)	1.76					
ZnO:CdS	(101)	2.482					
	(002)	2.585	3.21	5.19	53.47	09.39	Wurtzite
	(110)	1.602					Hexagonal

### 3.4 Scanning Electron Microscopy

The surface morphology of all pristine materials as well as the binary (ZnO-CdS) nanocomposites was carried out using a scanning electron microscopy (SEM), which is depicted in **Figure-4**. ZnO shows NRs shaped morphology (**Figure-4a**) without sensitization of CdS QDs. It is observed that the surfaces of the bare ZnO NRs appear clear and soft. SEM images of CdS QDs deposited on ZnO surfaces are shown in **Figure-4b**, which is appear rough and tarnished, which indicates that deposition of the CdS QDs on the surface of ZnO NRs. Randomly scattered spherical particles with uniform size-distribution of CdS QDs are good resolved on ZnO surface helps for the maximum anchoring of N719 dye molecule.



a)



b)

**Figure-4. a) SEM image of Bare ZnO NRs and b) SEM image of CdS QDs sensitized ZnO NRs.**

## 4. PHOTOVOLTAIC STUDIES

### 4.1 Photocurrent density-voltage (J-V) measurement

Wei et.al. designed CdS quantum dot-sensitized Zn<sub>2</sub>SnO<sub>4</sub> solar cells by surface treatment with Al<sup>3+</sup> ions and obtained results are shown in **Table-2** [23].

**Table-2. Cell parameters of CdS quantum dot-sensitized solar cells composed of Zn<sub>2</sub>SnO<sub>4</sub> treated with Al<sup>3+</sup> for 0–2 times.**

Electrode	Jsc (mAcm <sup>-2</sup> )	Voc (V)	Fill factor	Efficiency (%)
Zn <sub>2</sub> SnO <sub>4</sub>	0.49	0.487	0.455	0.109
Zn <sub>2</sub> SnO <sub>4</sub> /Al – 1	0.64	0.468	0.521	0.157
Zn <sub>2</sub> SnO <sub>4</sub> /Al – 2	0.53	0.444	0.530	0.126

Similarly, Yin et. al. fabricated CdSe–CdS quantum dots co-sensitized ZnO hierarchical hybrids for solar cells to improve the efficiency of solar device and obtained results are shown in **Table-3** [24].

**Table-3. Photovoltaic parameters of the assembled devices.**

Devices	Counter	Jsc (mA cm <sup>-2</sup> )	Voc (V)	FF (%)	η (%)
12 h ZnO	Cu <sub>2</sub> S	1.12	0.15	33.16	0.04
4CdS/24 h ZnO	Cu <sub>2</sub> S	3.07	0.49	30.53	0.46
4CdS/12 h ZnO	Cu <sub>2</sub> S	2.29	0.49	52.86	0.59
8CdS/12 h ZnO	Cu <sub>2</sub> S	4.01	0.57	37.98	0.87
12CdS/12 h ZnO	Cu <sub>2</sub> S	3.63	0.53	39.85	0.77
3CdSe–8CdS/12h ZnO	Cu <sub>2</sub> S	4.32	0.62	52.98	1.39

The solar devices are fabricated by using the composition of FTO/ZnO:CdS:N719/ (I<sup>-</sup>/I<sub>3</sub><sup>-</sup>) /Pt-ITO and tested under 1 sun (100 mW cm<sup>-2</sup> AM 1.5G) solar illumination conditions for photovoltaic studies. Similarly, DSSCs-based on ZnO:N719 dye and ZnO:CdS QDs also designed, and their photovoltaic performances compared with surface modified CdS QDs DSSCs. **Figure-5** shows the current density-voltage (J-V) characteristics of the hybrid cells i.e., ZnO:CdS,

ZnO:N719 and surface modified ZnO:CdS:N719 devices and corresponding photovoltaic parameters are listed in **Table-4**.

**Table-4. Photovoltaic properties of ZnO:N719, ZnO:CdS and ZnO:CdS:N719 device.**

Compositions	$I_{sc}$ (mA/cm <sup>2</sup> )	$V_{oc}$ (mV)	$FF$ (%)	$\eta$ (%)
ZnO ...CdS QDs	5.90	310	47.04	0.86
ZnO ...N719 dye	8.22	330	42.76	1.16
ZnO ...CdS QDs ..N719 (dye)	7.22	550	54.35	2.15

From photovoltaic parameters, it is seen that without surface modification of ZnO-N719 device shows poor performance [9-12], which may be due to complex formation of dye molecule with ZnO NRs. However, same ZnO NRs sensitized with CdS QDs shows 0.86% power conversion efficiency and which confirms that CdS QDs acts as a sensitizer. Therefore, CdS QDs are used as surface modifying agent as well as sensitizer in ZnO based DSSCs. After loading CdS QDs on the surface of ZnO N719 dye anchored on it and resulting efficiency of device is measured and it is seen that there is huge increment in efficiency of solar device. Specially,  $V_{oc}$  of the modified device is increased from 330 mV to 550 mV and corresponding efficiency is also increased from 1.16% to 2.15%. This is attributed to the near about double efficiency is increased for ZnO:CdS:N719 based device.

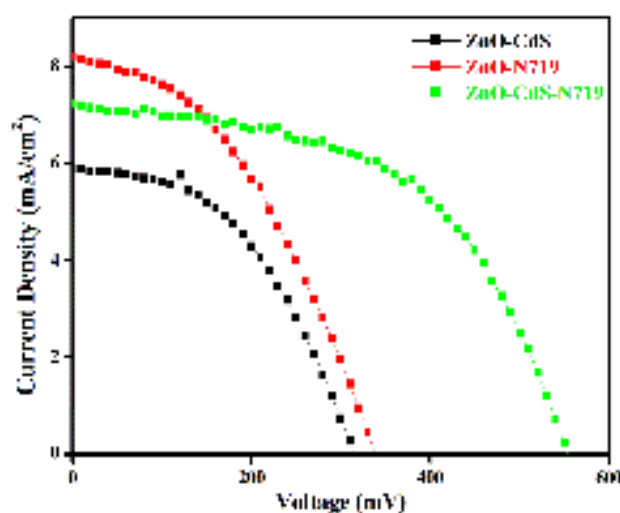


**Figure-5. Photocurrent -voltage (J-V) characteristics of single sensitized and co-sensitized ZnO based devices.**

## 5. CONCLUSION

In conclusion, the simple and convenient method is developed for the preparation of ZnO NRs. Then surface of ZnO NRs is further modified with CdS QDs, which significantly improves the optical behavior of the material. All characterization technique confirms the formation of CdS QDs and ZnO NRs. Thereafter, ZnO NRs:CdS QDs are co-sensitized with N719 dyes for photovoltaic studies. J-V measurements revealed that the CdS QDs:N719 dyes co-sensitized ZnO based devices have efficient photovoltaic performance as compared to individually sensitized devices. The ZnO sensitized with N719 dye showed 1.16% power conversion efficiency; while ZnO NRs sensitized CdS QDs showed 0.86% efficiency. Moreover, ZnO:CdS:N719 co-sensitized device showed 2.15% conversion efficiency.

## CONFLICTS OF INTEREST

There are no conflicts to declare.

## REFERENCES

1. Delekar, S. D., Dhodamani, A. G., More, K. V., Dongale, T. D., Kamat, R. K., Acquah, S. F., Dalal, N. S., Panda, D. K. (2018) ACS omega, 3, 2743–2756.
2. Dhodamani, A. G., More, K. V., Koli, V. B., Shelke, A. R., Deshpande, N. G., Panda, D. K., Delekar, S. D. (2019) ChemistrySelect, 4, 1055-68.
3. Delekar, S. D., More, K. V., Dhodamani, A. G., Maity, K., Acquah, S. F., Dalal, N., Panda, D. K. (2019) Journal of Solid-State Electrochemistry, 23, 1099-107.
4. Sun, W. T., Yu, Y., Pan, H. Y., Gao, X. F., Chen, Q., Peng, L. M. (2008) Journal of the American Chemical Society, 130, 1124-5.
5. Gong, J., Sumathy, K., Qiao, Q., Zhou, Z. (2017) Renewable and Sustainable Energy Reviews, 68, 234-246.
6. Chandiran, A. K., Abdi-Jalebi, M., Nazeeruddin, M. K., Grätzel, M. ACS nano, 8, 2261-2268.
7. Leschkies, K. S., Divakar, R., Basu, J., Enache-Pommer, E., Boercker, J.E., Carter, C.B., Kortshagen, U.R., Norris, D.J., Aydil, E.S. (2007) Nano letters, 7, 1793-8.
8. Zhao, H., Liu, L., Vellacheri, R., Lei, Y. (2017) Advanced Science, 4, 1700188.
9. Hu, J., Li, M., Lv, F., Yang, M., Tao, P., Tang, Y., Liu, H., Lu, Z. (2015) Journal of Power Sources, 294, 120-7.

10. Kim, B. G., Chung, K., Kim, J. (2013) *Chemistry–A European Journal*, 19, 5220-5230.
11. Ooyama, Y., Harima, Y. (2012) *ChemPhysChem*, 13, 4032-4080.
12. Shi, Y., Zhu, C., Wang, L., Zhao, C., Li, W., Fung, K.K., Ma, T., Hagfeldt, A., Wang, N. (2013) *Chemistry of Materials*, 25, 1000-12.
13. Peh, C. K. N., Ke, L., Ho, G. W. (2010) *Materials Letters*, 64, 1372-5.
14. Liu, Y., Zhao, J., Li, Z., Mu, C., Ma, W., Hu, H., Jiang, K., Lin, H., Ade, H., Yan, H. (2014) *Nature communications*, 5, 5293.
15. Nazeeruddin, M. K., Pechy, P., Renouard, T., Zakeeruddin, S. M., Humphry-Baker, R., Comte, P., Liska, P., Cevey, L., Costa, E., Shklover, V., Spiccia, L. (2001) *Journal of the American Chemical Society*, 123, 1613-24.
16. Lü, X., Mou, X., Wu, J., Zhang, D., Zhang, L., Huang, F., Xu, F., Huang, S. (2010) *Advanced Functional Materials*, 20, 509-15.
17. Rao, H., Sun, W., Ye, S., Yan, W., Li, Y., Peng, H., Liu, Z., Bian, Z., Huang, C. (2016) *ACS applied materials & interfaces*, 8, 34482-9.
18. Wang, Z.S., Kawauchi, H., Kashima, T., Arakawa, H. (2004) *Coordination chemistry reviews*, 248, 1381-9.
19. Delekar, S. D., More, K. V., Dhodamani, A. G., Patil, S. M., Dongale, T., Maity, K., Dalal, N., Panda, D. K. (2018) *Materials Characterization*, 139, 337-46.
20. Murphy, C. J. (2002) *Analytical Chemistry*, 74, 520-A.
21. Zhao, W. W., Ma, Z. Y., Yu, P. P., Dong, X. Y., Xu, J. J., Chen, H.Y. (2012) *Analytical chemistry*, 84, 917-23.
22. Mahapatra, N. (2014) *Journal of Materials Chemistry C*, 2, 7373-84.
23. Li, Y., Guo, B., Zheng, X., Pang, A., Wei, M. (2012) *Electrochemical acta.*, 60, 66-70.
24. Yuan, Z., Yin, L. (2014) *Nanoscale*, 6, 13135-13144.

# Review on Candle Soot based Superhydrophobic Surfaces for Oil-Water Separation

Mehejbin R. Mujawar<sup>a,\*</sup>, Rajesh B. Sawant<sup>a</sup>, Amol B. Pandhare<sup>b,f</sup>,  
Prashant D. Sanadi<sup>g</sup>, Sanjay S. Latthe<sup>c</sup>, Ankush M. Sargar<sup>d</sup>,  
Raghunath K. Mane<sup>e</sup>, Shivaji R. Kulal<sup>a,\*</sup>

<sup>a</sup>Department of Chemistry, Raje Ramrao Mahavidyalaya, Jath, Sangli 416 404 (MS) India.

<sup>b</sup>Department of Chemistry, Shivaji University, Kolhapur 416 004 (MS) India.

<sup>c</sup>Department of Physics, Vivekanand College, Kolhapur 416 003 (MS) India.

<sup>d</sup>Department of Chemistry, Bharati Vidyapeeth's Dr. Patangrao Kadam Mahavidyalaya,  
Sangli 416 416 (MS) India.

<sup>e</sup>Department of Chemistry, Smt. Kusumtai Rajarambhapu Patil Kanya Mahavidyalaya,  
Islampur, Sangli 416 409 (MS) India.

<sup>f</sup>Department of Chemistry, M.H. Shinde Mahavidyalaya, Tisangi, Gaganbavda, Kolhapur 416 206 (MS) India.

<sup>g</sup>Department of Enggining, Chemistry, Institute of Technology's College of Engineering (Autonomous),  
Kolhapur 416 234 (MS) India.

\*Corresponding authors: srkulal@gmail.com and mehejabeenmujawar@gmail.com

---

## ABSTRACT

*Over the many years, the oceanic oil spill accidents and most industries worldwide discharging immense levels of oil in the surroundings is a serious problem for the environment. There is a need to develop technology for oil-water separation because the spilled oil affects the ecological and environmental system. Candle soot nanoparticles are hydrophobic (water repellent) in nature and has the advantages of cost-effectiveness and production scalability over other carbons like graphene, Carbon Nanotubes (CNTs), Carbon Nanodots (CNDs), etc. in their synthesis. Candle soot based superhydrophobic materials have outstanding water repulsion and oil absorption capacity, highly selectivity, chemical inertness and excellent recyclability. In this paper, we discuss applications of candle soot based superhydrophobic materials applied on sponge and mesh substrates for oil-water separation.*

## KEYWORDS

*Carbon Nanotubes, Carbon Nanodots.*

---

## 1. INTRODUCTION

The oil spilling and discharge of industrial organic solvents causes several damages to water resources and aquatic ecosystems [1-3], which became a global problem and need to solve it urgently to save the ecosystems. A new technology in material science has been developed for oil-water separation using superhydrophobic nanomaterial. As like the lotus leaf, superhydrophobic surface having water contact angle greater than 150° and oil contact angle near 0°[4]. Different chemical methods



are used for the fabrication of the superhydrophobic mesh/sponge for efficient oil-water separation. As the carbon nanoparticles are hydrophobic in nature, it shows strong affinity toward oil. At the same time, huge amount of candle soot waste is produced. Undoubtedly, it is of great benefit to turn candle soot waste into high value oil absorbent materials [5]. The superhydrophobic mesh/sponge exhibited high selectivity toward different oil and organic pollutants, fast and efficient oil-water separation capability, good repeatability, good reusability, mechanically stable, chemically stable and thermally stable [6]. Candle soot-based absorbents demonstrate superior efficiency in the removal of oils. However, the high production costs of carbon nanotube[7], graphene[8], activated carbon [9], expanded graphite [10], etc. So, these absorbents limit their wide adoption at large scale. Candle soot (CS) generated from incomplete combustion of paraffin wax has demonstrated the advantages of cost effectiveness and production scalability over CNTs, graphene and activated carbons in their synthesis [11]. However, candle soot coated superhydrophobic materials are the best solution from these. The superhydrophobic surfaces on which water achieves water contact angle higher than  $150^\circ$  and sliding angle less than  $5^\circ$  are attracting minds of researchers due to their efficient oil-water separation abilities [12-14]. J. Song et al. [15] fabricated CS-coated mesh by using dip-coating method. The cleaned stainless-steel mesh (SSM) was dipped in the glue solution for 10 min and then dried at  $80^\circ\text{C}$  to obtain the CS-glue coated mesh. The CS coating is close packed because of using superglue as a binder. The CS-glue coated mesh revealed the separation efficiency higher than 99.95%. Even after 20 cycle separation tests, it was shown superior reusability and durability. Li et al. [16] prepared the hydrophobic CS by incomplete combustion of hydrocarbons from the middle of candle flame. The PU sponge dipped in the solution of CS,  $\text{SiO}_2$  and PU resin to achieve stable superhydrophobicity. The CS- $\text{SiO}_2$ -PU sponge showed excellent oil-water separation efficiency. The CS- $\text{SiO}_2$ -PU sponge was also shown superior separation efficiency from hot water, acidic solutions, alkaline solutions and salt solutions. Zulfiqar et al. [17] deposited cheaply available sawdust on polychloroprene adhesive-coated stainless-steel mesh with deposition of silicone polymer by using dip-coating method. Then, a thin layer of CS particle was applied on the prepared stainless-steel mesh by simply holding it above a candle flame. The CS particles get uniformly deposited on silicone covered sawdust which exhibited highly rough and porous morphology required for superhydrophobicity. It showed excellent oil-water separation efficiency greater than 95% which showed its recyclability, reusability and mechanical stability. In this article, we will mostly discuss on the simple, low-cost, rapid and innovative methods for the fabrication of superhydrophobic/superoleophilic CS coated sponges/meshes for efficient oil-water separation application.

## 2. SUPERHYDROPHOBIC-SUPEROLEOPHILIC SURFACES FOR OIL-WATER SEPARATION

### 2.1 Oil-water separation using Superhydrophobic-superoleophilic sponges

#### 2.1.1 Highly efficient carbon soot sponge

The CS particles obtained from ethylene-oxygen combustion flame with flow rate of 5:3. These CS particles were dispersed in 1, 2-dichloroethane followed by sonication. The sponge was dipped in CS dispersion solution to attain superhydrophobic sponge. The superhydrophobic sponge achieved by a uniform coating of as-grown CS particles onto the porous skeleton through simple immersion in CS dispersion. The CS-modified sponge exhibited excellent oil-water separation efficiency without further chemical modification. The fast and easy recovery of engine oil floating on the water surface by CS-modified sponge confirms its high oil-water separation efficiency. The CS-sponge was shown an absorption capacity in the range of 25-80 times its original weight. The absorption capacity of the CS-sponge does not show severe degradation after 10 cycles which indicating a highly stable absorption performance of CS-sponge. After 10 cycles which indicating a highly stable absorption capacity is kept for CS-modified sponge, which much higher than that of the CS-sponge [18].

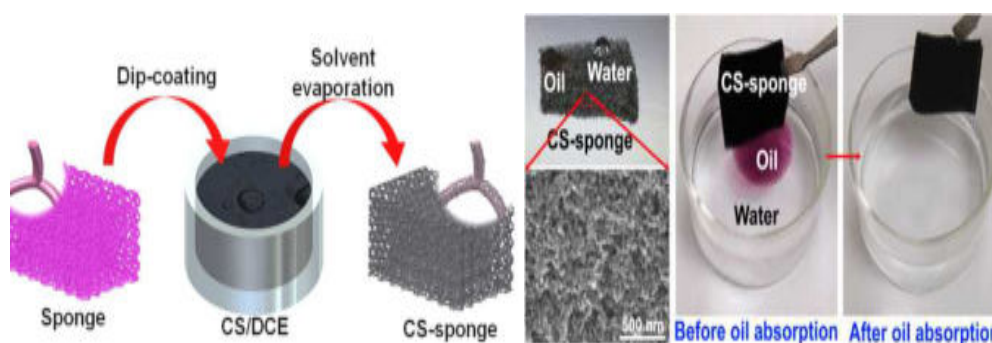


**Figure-1. Schematic showing the carbon soot-sponge preparation by dip-coating and carbon soot sponge before & after oil absorption. Images reprinted from [18], with permission from American Chemical Society, Copyright 2014.**

#### 2.1.2 Recyclable superhydrophobic straw soot sponge

The straw soot on the glass slide was collected by shaving soot from the glass using a spatula. The colloidal suspension of CS was prepared by simply mixing the soot in ethanolic medium. The sponge was dipped into straw soot solution by using dip-coating method to form superhydrophobic sponge. The modified sponge was shown the water contact angle up to  $154^\circ$ . This superhydrophobic sample had good hydrophobic stability even in acidic condition and it can show the efficient oil-water separation. The amount of the absorbed oil was about 30 times of sponges own

weight which can be shown that the evaluation of the mass based on absorption capacity. The absorption capacity based on density, viscosity and surface tension of the absorbed liquids. This superhydrophobic sponge shows highly recyclability. The experiments demonstrate that the sponge can absorb the oil more than 30 cyclic applications without any significant change in the absorption. This method shows the benefits of easy preparation using natural soot source, better performance, oil absorption in a very short time in comparison with previous works [19].

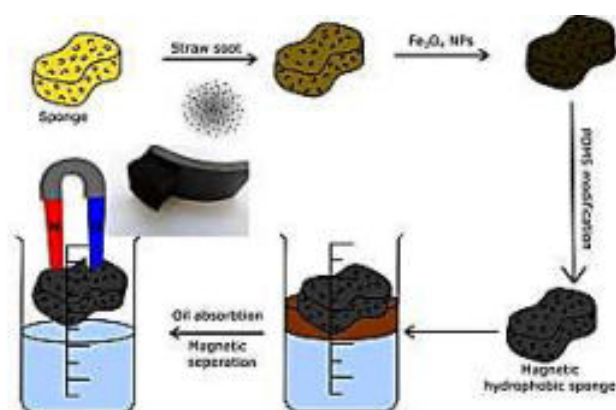


**Figure-2. Schematic illustration of preparation of modified polyurethane sponge and oil separation process. Images reprinted from [19], with permission from Elsevier, Copyright 2017.**

### **2.1.3 Durable PVDF/CS sponge**

The superhydrophobic surface was fabricated by using PVDF and candle soot via sugar template method. It was shown the water contact angle of  $158.3^\circ$  and roll on angle of  $6.7^\circ$ . The oil quickly absorbed by superhydrophobic sponge which can be shows the superoleophilic property of superhydrophobic sponge. The solar value of candle soot is up to 99.4% which shows excellent light absorbing property. The sponge shows excellent oil-water separation property even after 25 cycles without destroying the sponge. The strong elasticity & high stretch resistance confirms that the modified superhydrophobic surface is highly mechanical durable. The modified sponge maintains the 89% of recovery rate even after 10 cycles. The absorption capability recovered up to 96% without obvious change of morphology of the sponge surface. This method was used to prepare a photothermal & porous PVDF/CS sponge with structural, chemical and mechanical property. It was shown high photothermal property.

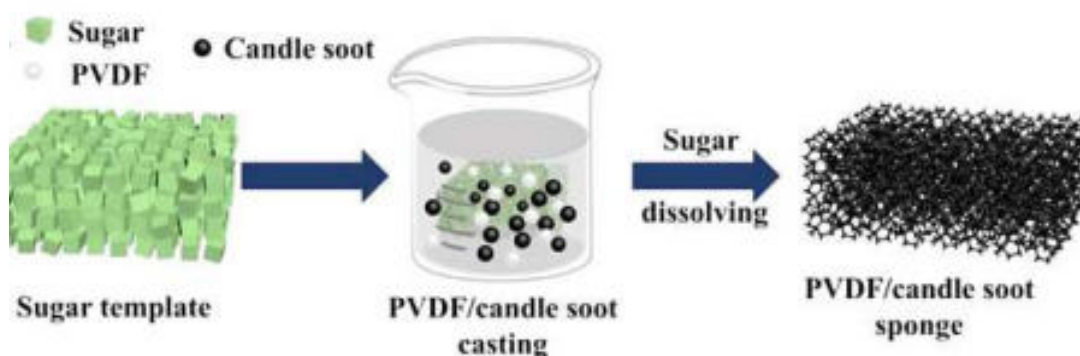


Figure-3. Schematic illustration of the fabrication of porous PVDF/candle soot sponge using sugar template. Images reprinted from [20], with permission from Elsevier, Copyright 2021.

## 2.2 Oil-water separation using superhydrophobic-superoleophilic meshes

### 2.2.1 Superhydrophobic $\text{SiO}_2$ /Carbon mesh

The candle soot was collected on the surface of stainless-steel mesh by placing the mesh above the wick of candle. Then by using chemical vapour deposition method the  $\text{SiO}_2$ /carbon layer deposited on stainless steel mesh. Modify this mesh by using PFOTS and PDDA-PFO respectively to form the superhydrophobic and superoleophilic mesh membrane. This modified superhydrophobic stainless steel mesh exhibits excellent repellence for all the tested strong acids, strong bases and saturated salts, indicating a good stability of modified mesh under a series of hard environment. The separation efficiencies obtained repeatedly even after 15 cycles without any noticeable deterioration. Both superhydrophobic and superoleophilic modified stainless steel mesh membranes shows stability, durability and reusability. The  $\text{SiO}_2$ /Carbon modified stainless steel mesh indicates good material for treating real oil-polluted water in different practical applications as well as in oil spill clean-up. This method shows higher performance, oil-water separation in a short time and repeatedly in comparison with earlier works [20].

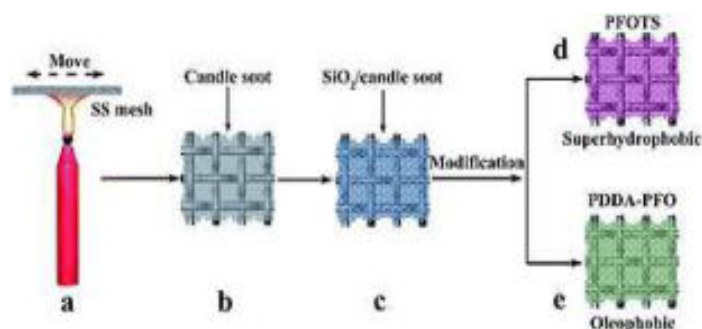
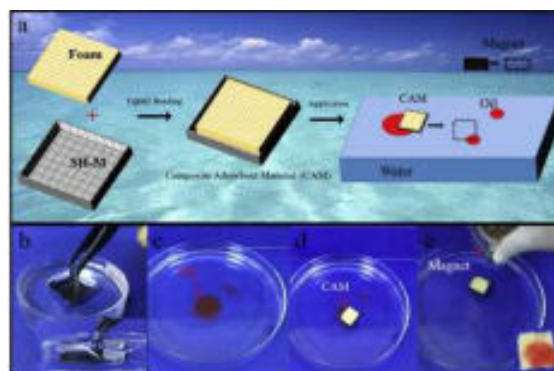


Figure-4. Process of superhydrophobic and oleophobic mesh membranes preparation: (a) coating stainless steel mesh with carbon nanoparticle (candle

soot), (b) carbon nanoparticle coated stainless steel mesh, (c) SiO<sub>2</sub>/carbon stainless steel mesh, (d) PFOTS modified SiO<sub>2</sub>/carbon stainless steel mesh, (e) PDDA–PFO modified SiO<sub>2</sub>/carbon stainless steel mesh. Images reprinted from [21], with permission from Royal Society of Chemistry, Copyright 2017.

### 2.2.2 Durable PDMS-CS based superhydrophobic mesh

The candle soot was deposited on stainless steel mesh by simply placed above the candle flame for 15 sec. Then this CS coated stainless steel mesh was dipped in solution of PDMS & Xylene for 10 min by using immersion method. After that same process will be carried out for deposition of candle soot on this modified stainless-steel mesh was prepared. It was shows 156<sup>0</sup> water contact angle & nearly 0<sup>0</sup> oil contact angle. Also, it was shown 3<sup>0</sup> sliding angles. It was shows higher water contact angle even after 10 times tests of oil-water separation. The oil-water separation efficiency was nearly 91% by using this modified superhydrophobic stainless steel mesh. It exhibits high thermal stability, good corrosion resistance and reusability. It was modified though combine mesh & polymer foam the composite adsorbent material successfully separate the oil from water via magnet drive method. This modified method was very useful than other research work. So, it was very useful than any other works [21].



**Figure-5. a) Schematic for the preparation process of composite adsorbent material (CAM) from the SH-M square boat and polymer foam, as well as its application of magnet drive for oil/water separation; b) SH-M square boat immersion in water by force; c–e) picture of the magnet drive CAM oil adsorption process. Images reprinted from [22], with permission from Progress in Organic Coatings, Copyright 2019.**

### 2.2.3 CS templated superhydrophobic silica coating on SS mesh

The superhydrophobic coating was prepared through placing the cleaned substrate over candle flame until a few microns thick layer of candle soot deposited on



stainless steel mesh. The candle soot coated substrate together with  $\text{SiCl}_4$  was placed in a drier for chemical vapour deposition. Then, though calcination at  $600\text{ }^\circ\text{C}$  for half in air, CS composed NPs thermally degraded and diffused through the silica shell gradually. It shows highly oil-water separation efficiency even after 30 times cycle separation superhydrophobic surface remained. The superhydrophobic coating revealed excellent separation efficiency even after 6 times reuses of same superhydrophobic material. It could be potentially used in optical and visual application scenarios where in harsh & oily environments, like goggles, building façade, visual oil-water separation device & touch screen, etc. Among the all-other research work it shows tremendous oil-water separation properties [22].

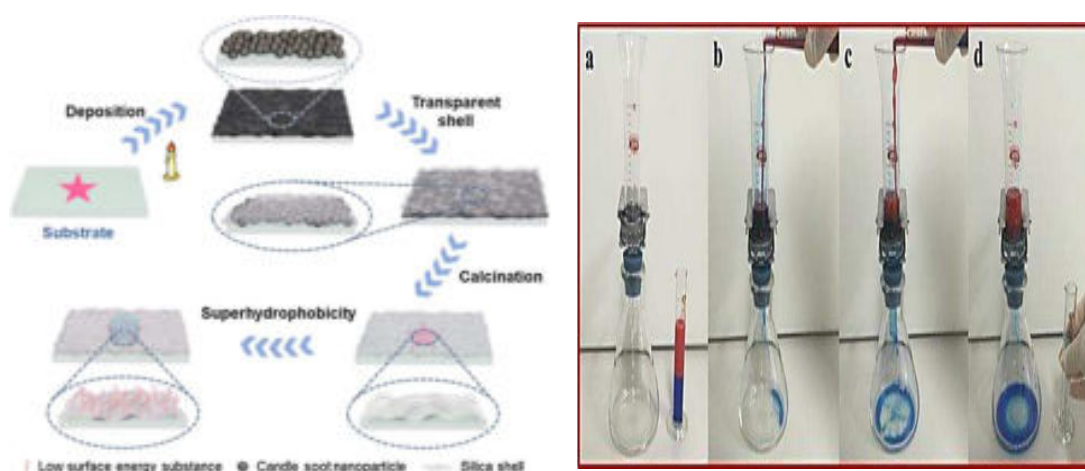


**Figure-6. Schematic of preparation and properties of the transparent and robust superhydrophobic coating and oil–water separation. Images reprinted from [23], with permission from Nature, Copyright 2022.**

### 3.CONCLUSION

As this review highlights, candle soot nanoparticles are unique in that, their fabrication requires little control of external parameters. It is very economical beneficial, facile and straightforward to synthesize. Candle soot coated sponge/mesh for use in oil-water separation has been developed by using CS-nanoparticles and different polymers. The candle soot synthesis, candle soot coated sponge/mesh preparation, procedures are simple, cost-effective and scalable. The absorption/separation investigation demonstrates that, the candle soot sponge/mesh is highly efficient and stable in absorbing a wide range of oil and organic solvents. It can be believed that, the candle soot coated superhydrophobic materials are very useful for oil-water separation. It shows various tremendous results with candle soot-

polymer composite in various mechanical conditions. A candle soot nanoparticle shows significant surface area to volume ratio, high electronic and ionic conductivity. Candle soot is produced by simply burning of candles and hence, it is ecofriendly, economical and useful. Candle soot coated sponge/mesh can show stability, durability, reusability and reproducibility.

## ACKNOWLEDGEMENT

This work was supported by Department of Chemistry and Department of Physics, RajeRamrao Mahavidyalaya, Jath. We also acknowledge Prof. (Dr.) Suresh S. Patil, Principal, RajeRamrao Mahavidyalaya, Jath.

## REFERENCES

1. Yao, T.,Zhang, Y.,Xiao, Y.,Zhao, P.,Li, G.,Yang, H., Li, F.(2016) Journal of Molecular Liquids, 218, 611–614.
2. Bi, H., Xie, X., Yin, K., Zhou, Y., Wan, S., He, L., Xu, F., Banhart, F., Sun, L., Ruoff, R.S. (2012) Advanced Functional Materials, 22, 4421-4425.
3. Cong, H.P., Ren, X.C., Wang, P., Yu, S.H. (2012) American Chemical SocietyNano, 6, 2693-2703.
4. Li, L., Li, B., Dong, J., Zhang, J. (2016) Journal of Materials Chemistry A, 4, 13677-13725.
5. Gao, J., Huang, X., Xue, H., Tang, L., Li, R.K. (2017) Chemical Engineering Journal, 326, 443-453.
6. Bayat A., Aghamiri, S. F., Moheb, A.,Vakili-Nezhaad, G. R.(2005) Chemical Engineering & Technology, 12, 28-40.
7. Li, J., Zhu, L.,Luo, Z.(2016) Chemical Engineering Journal, 287, 474-481.
8. Wu, Z., Li, C., Liang, H., Zhang, Y.,Wang, X., Chen, J.,Yu, S. (2014) Scientific Reports, 4, 4079.
9. Bi, H., Xie, X., Yin, K., Zhou, Y., Wan, S., He, L., Xu, F., Banhart, F.,Sun, L.,Ruof, R. S.(2012), Advanced Functional Materials, 22, 4421-4425.
10. Sam, E. K., Sam, D. K., Lv, X., Liu, B., Xiao, X., Gong, S., Yu, W., Chen, J., Liu, J.(2019) Chemical Engineering Journal, 19, 3012-3018.
11. Zulfiqar, U., Hussain, S. Z., Subhani, T., Hussain, I., Rehman, H.(2018), Colloids and Surfaces A: Physicochemical and Engineering Aspects, 539, 391–398.
12. Gao, Y., Zhou, Y. S., Xiong, W., Wang, M., Fan, L., Golgir, H., Jiang, L., Hou, W., Huang, X., Jiang, L., Silvain, J.,Lu, Y. F. (2014) ACS Applied Materials &Interfaces, 6, 5924–5929.
13. Ren, G., Song, Y., Li, X., Zhou, Y.,Zhang, Z., Zhu, X.(2018) Applied Surface Science, 428, 520-525.

14. Choi, S., Kwon, T., Im, H., Moon, D., Baek, D., Seol, M., Duarte, J., Choi, Y.(2011) *ACS Applied Materials & Interfaces*, 3, 4552–4556.
15. Song, J., Na, L., Li, J., Cao, Y., Cao, H.(2022) *Nanomaterials*, 12, 761-775.
16. Li, J., Zhao, Z., Kang, R., Zhang, Y., Lv, W., Li, M., Jia, R., Luo, L.(2017)*Journal of Sol-Gel Science and Technology*, 3, 817–826.
17. Zulfiqar, U., Hussain, S., Subhani, T., Hussain, I., Rehman, H.(2018) *Colloids and Surfaces A: Physicochemical and Engineering Aspects*, 539, 391–398.
18. Gao, Y., Zhou, Y., Xiong, W., Wang, M., Fan, L., Rabiee-Golgir, H., Jiang, L., Hou, W., Xi, H., Jiang, L., Silvain, J., Lu, F.(2014) *ACS Applied Materials & Interfaces*, 6, 5924–5929.
19. Beshkar, F., Khojasteh, H., Niasari, M.(2017) *Journal of Colloid and Interface Science*, 497, 57–65.
20. Liu, D., Yu, Y., Chen, X., Zheng, Y.(2017) *RSC Advances*, 7, 12908–12915.
21. Zhang, R., Zhou, Z., Ge, W., Lu, Y., Liu, T., Yang, W., Dai, J. (2020) *Chinese Journal of Chemical Engineering*, 5, 30292-30294.
22. Chen, B., Zhang, R., Fu, H., Xu, J., Jing, Y., Xu, G., Wang, B., Xu, H.(2022)*Scientific Reports*, 8, 1-9.



# A Review on Current Advancements in Magnetic Nanomaterials for Magnetic Hyperthermia Applications

Amol B. Pandhare<sup>a,b</sup>, Prakash S. Pawar<sup>a,c</sup>, Vijay S. Ghodake<sup>a,d</sup>, Swapnajit V. Mulik<sup>a</sup>, Pramod A. Koyale<sup>a</sup>, Ankita K. Dhukate<sup>a</sup>, Deepak B. Mohite<sup>b</sup>, Karishma V. Shikhare<sup>b</sup>, Rajendra P. Patil<sup>b,\*</sup>, Sagar D. Delekar<sup>a,\*</sup>

<sup>a</sup>Department of Chemistry, Shivaji University, Kolhapur 416 004 (MS) India.

<sup>b</sup>Department of Chemistry, M.H. Shinde Mahavidyalaya, Tisangi, Gaganbavda, Kolhapur 416 206 (MS) India.

<sup>c</sup>Department of Chemistry, Shri Yashwantrao Patil Science College, Solankur, Kolhapur 416 212 (MS) India.

<sup>d</sup>Department of Chemistry, Yashwantrao Chavan Mahavidyalaya, Halkarni, Kolhapur 416 552 (MS) India.

\*Corresponding author: sdd\_chem@unishivaji.ac.in and patilraj\_2005@rediffmail.com

---

## ABSTRACT

Cancer is one of the major causes of death worldwide, and its prevalence is rising every day. Nanoscience and nanotechnology, as well as their diverse applications, have proliferated around the world due to the different techniques for producing unique nanomaterials. Nowadays, nanotechnology is widely used in the form of nanotherapeutics in the biomedical field. Therefore, current biomedical research pays much attention to micro-structured nanomaterials for the development of efficient cancer treatment. Iron-containing nanoparticles, in particular, are being extensively used to produce very effective killing of the cancerous cell by magnetic hyperthermia therapies. The present review is focusing on representative nanomaterials for nano-bio applications. The review covers all of the major topics of magnetic nanoparticle functionalization. This paper provides an in-depth and current overview of mixed metal oxide nanoparticles in terms of characteristics, uses, and hyperthermia classes, as well as potential biological applications. In addition, this review covers the fundamentals of magnetic hyperthermia, heat loss processes, induction heating systems in detail, and ideas for improving heating efficiency. This study tried to provide a comprehensive evaluation of magnetic hyperthermia therapy through the determination of magnetic nanoparticles such as surface chemistry, and intrinsic and extrinsic magnetic properties. In addition, the features of the magnetic field that substantially play on induction heating power and hyperthermia temperature are reviewed. Furthermore, the constraints in this interesting field, as well as prospects, are discussed.

## KEYWORDS

Cancer, Magnetic hyperthermia therapy, Magnetic nanoparticles, Cancer therapy, Covering and functional materials, Magnetic materials.

## 1. INTRODUCTION

Cancer is one of the most devastating diseases in the world, causing millions of fatalities every year[1]. Over the past two decades, the mortality rate has significantly reduced due to considerable progress in the diagnosis and treatment of the disease[2]. The optimization of the heating efficiency of magnetic nanoparticles (MNPs) can shape their future in biomedical applications, such as hyperthermia therapy, heat-mediated drug delivery, and heat-triggered control of biological processes. In this section, we will review the solution-based synthesis routes that have recently been employed to obtain MNPs. Nanoparticles (NPs) are defined as particles that have one or more physical dimensions under 100 nm. Due to their small size, and particularly due to their increasing surface-to-volume ratio, the properties of nano-sized materials will differ from the ones of the bulk material (i.e., optic, catalytic, magnetic, and electronic properties)[3]. According to the World Health Organization fact sheet, 2017, cancer is one of the key reasons for leading morbidity and mortality rates worldwide, with approximately 70% of deaths occurring in low and middle-income countries are shown in **Figure-1**.

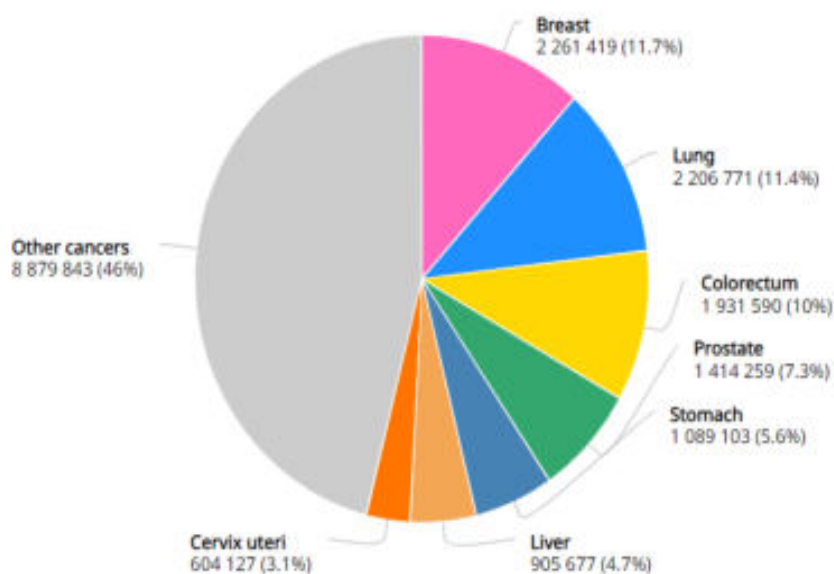


**Figure-1. Estimated number of new cases in 2020, all cancers, Both sexes, ages 0-85.**

Nanostructured magnetic materials have undoubtedly seen widespread use in a variety of applications in recent years, including catalysis, drug delivery, water purification and sterilization, and self-cleaning coatings[4]. Their fascinating

properties have led to their applications in catalysis, hyperthermia, contrast agents in magnetic resonance imaging, and energy storage via ion adsorption or fast surface redox reactions are shown in **Figure-2**. In recent years, nanostructured metal oxides, a particular class of nanoparticles, have gained considerable attention from the scientific community owing to their unexpected physical and chemical properties that comes from the quantum confinement at nano dimensions[5]. For biomedical applications, such superparamagnetic particles are preferred due to this property of no retained magnetization (zero remanence,  $M_r$ ) once the magnetic field is removed. MNPs, nanoscale substances with unique magnetic characteristics, are one of them that have been widely employed in many industries such as biomedical, energy, engineering, and environmental applications[6]. Because of their unique and distinguishing features, MNPs have recently become a focus of intense research due to their potential applications in biology, catalysis, agriculture, and the environment.



**Figure-2. Schematic representation of biomedical applications of IONPs.**

In this review, we will discuss propulsion and steering of micro- and nanostructures induced by external magnetic fields. Using magnetic fields for manipulation has several advantages. First of all, the response can be varied by choosing the type of magnetism of the material, ranging from ferromagnetism and paramagnetism to diamagnetism. In this review, we will focus on the basic concepts of magnetism and review the physics of the hyperthermia process. though some excellent reviews on magnetic manipulation of nanostructures have been published in the past, most of them have focused on micro and nanostructures containing ferromagnetic and paramagnetic particles, since these only require magnetic fields up

to several tenths of mT. Here, we also include the magnetic manipulation of diamagnetic materials, which normally require magnetic fields in the order of 1 T or more. The ability to magnetically manipulate seemingly nonmagnetic (diamagnetic) materials can lead to new opportunities to control and steer (biocompatible) so much matter. It is our goal to inform the reader about the possibilities of these different types of magnetic materials and magnetic fields for the propulsion and steering of micro- and nanostructures. In the remainder of this review, we will focus on the three introduced classes of magnetic materials. For each, we will discuss how homogeneous, inhomogeneous, rotating and oscillating magnetic fields can be used to manipulate the motion of micro- and nanostructures.

## **2. PRESENT CANCER TREATMENT: PROS AND CONS**

There are many types of cancer treatment. The treatment you receive depends on the type of cancer you have and how advanced it is. Some people with cancer will have only one treatment. But most people have a combination of treatments such as surgery with chemotherapy and radiation therapy, etc.

### **2.1 Chemotherapy**

Chemotherapy is a type of cancer treatment that uses drugs to kill cancer cells[7]. Chemotherapy is used to treat many types of cancer. Chemotherapy not only kills fast-growing cancer cells but also kills or slows the growth of healthy cells that grow and divide quickly. Examples are cells that line your mouth and intestines and those that cause your hair to grow. Damage to healthy cells may cause side effects, such as mouth sores, hair loss, and nausea.

### **2.2 Hormone therapy**

Hormone therapy is a cancer treatment that slows or stops the growth of cancer that uses hormones to grow. Hormone therapy is also called hormonal therapy, hormone treatment, or endocrine therapy[8].

### **2.3 Hyperthermia**

Hyperthermia is a type of treatment in which body tissue is heated to as high as (42-44°C) to help damage and kill cancer cells with little or no harm to normal tissue. Hyperthermia to treat cancer is also called thermal therapy, thermal ablation, or thermotherapy[9].

### **2.4 Immunotherapy**

Immunotherapy is a type of cancer treatment that helps your immune system fight cancer. Immunotherapy is a type of biological therapy. Biological therapy is a type of treatment that uses substances made from living organisms to treat cancer.

## 2.5 Photodynamic therapy

Photodynamic therapy uses a drug activated by light to kill cancer and other abnormal cells.

## 2.6 Radiation therapy

Radiation therapy is a type of cancer treatment that uses high doses of radiation to kill cancer cells and shrink tumors[10].

## 2.7 Stem cell transplant

Stem cell transplants are procedures that restore stem cells that grow into blood cells in people who have had theirs destroyed by high doses of chemotherapy or radiation therapy.

## 2.8 Surgery

When used to treat cancer, surgery is a procedure in which a surgeon removes cancer from your body[11]. There are many types of surgery. The types differ based on the purpose of the surgery, the part of the body that requires surgery, the amount of tissue to be removed, and, in some cases, what the patient prefers.

## 2.9 Targeted therapy

Targeted therapy is a type of cancer treatment that targets the changes in cancer cells that help them grow, divide, and spread.

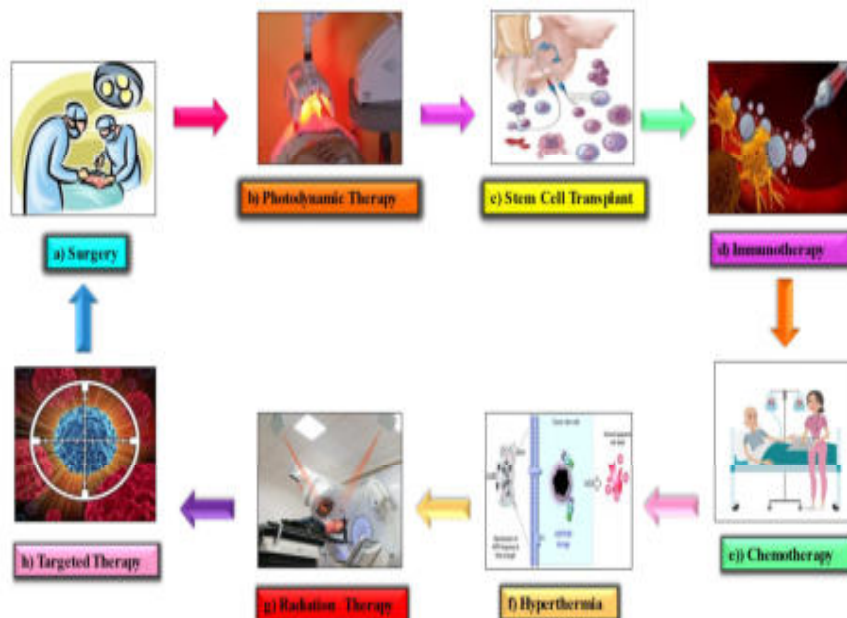
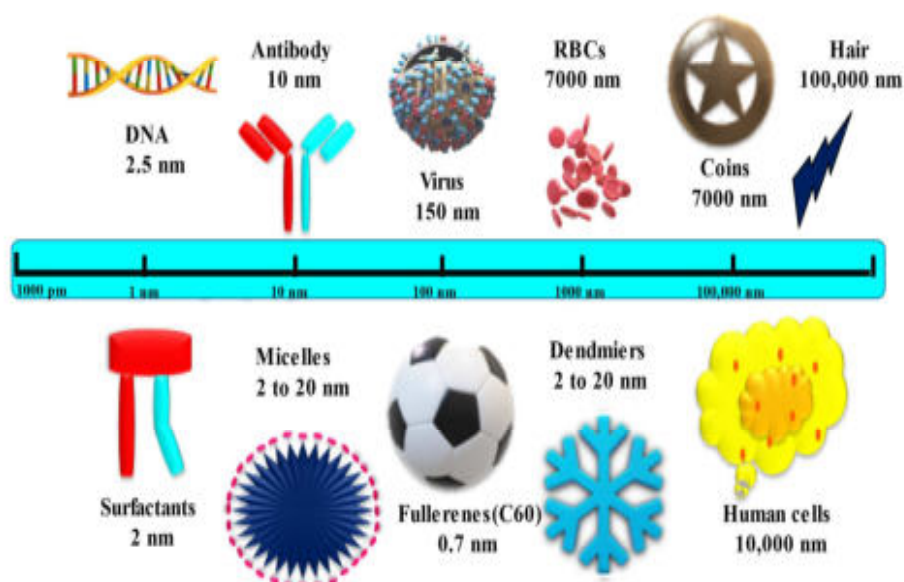


Figure--3. Types of cancer treatment.

### 3. CLASSIFICATIONS OF NANOMATERIALS

Nanomaterials (NMs) are gaining popularity in nanotechnology due to their adaptable chemical, physical, mechanical, and physical characteristics, as well as their improved performance compared to bulkier rivals[12]. NM is divided into several categories depending on various factors. NMs are classified according to their size, stage, morphology, and chemical content. Also, this classification is determined by their size, which falls between 1-100 nm in at least one dimension are shown in **Figure-4**.



**Figure--4. Scheme showing the size scale of objects compared with the nanoscale regime.**

NMs can be classified into four types based on their dimensions and general appearance are shown in **Figure-5**. All dimensions of zero-dimensional nanomaterials (0D) are on the nanoscale, i.e., they are less than 100 nm[13]. Spherical NM, nanorods, cubes, hollow spheres, metal, and core-shell NM, as well as quantum dots, are all included in 0D. Zero-dimensional materials are measured in all dimensions within the nano range, such as certain clusters and nano shells. A one-dimensional system with diameters ranging from 1 to 100 nm and a single layer, employed in sectors such as solar cells, it adds to numerous technical applications such as natural sensors, storage devices, and fiber-optic systems[14]. One-dimensional nanomaterials (1D) are one-dimensional materials that are not on the nanoscale but

in the other two dimensions. Metallic, polymeric, nanotubes, nanorods or fibers, nanowires, and nanofibers are examples of 1D materials. Two-dimensional nanomaterials (2D) have just one dimension on the nanoscale, whereas the other two do not. 2D thin films, nanolayers, and nanoplates can be single-layered or multi-layered, crystalline, or amorphous. Three-dimensional (3D) materials have dimensions greater than 100 nm. 3D NMs mix several nanocrystals in various directions. C60 fullerenes, quantum dots, foams, fibers, carbon nanobuds, nanotubes, and pillars are examples of the same[15].

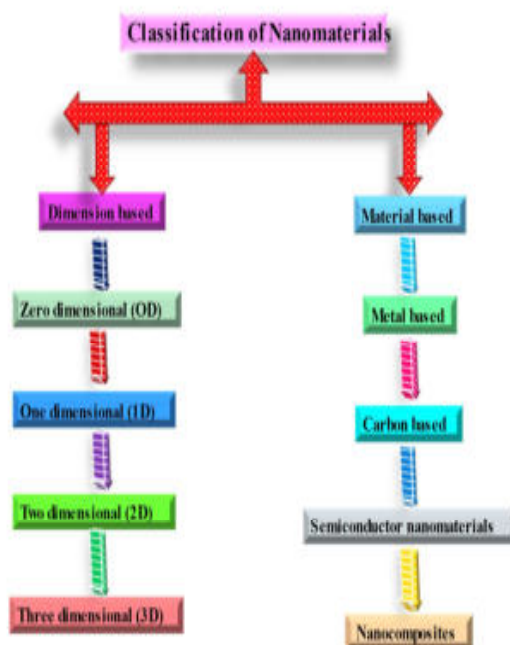


**Figure-5. Classification of various nanomaterials.**

#### **4. THE KEY ROLE OF MAGNETISM IN HYPERTHERMIA APPLICATION**

In the research of magnetic hyperthermia, magnetism plays a significant role and hence its detailed discussion of their types is necessary for a complete understanding of the hyperthermia phenomenon. So, in that sense, the basics of magnetism as well as the different types of magnetic materials are highlighted here.

##### **4.1 Basics of magnetism**

The matter is made up of atoms; which further consist of a positively charged nucleus surrounded by negatively charged electrons revolving in orbits around the nucleus[16]. Particularly, magnetism has been contributed by the different processes, viz. orbital motion, as well as spin motion of electrons, and spin motion of the



nucleus. These three motions are also defined through (i) orbital magnetic momentum of electrons, (ii) spinmagnetic momentum of electrons, and (iii) spin magnetic momentum of the nucleus, respectively.

## 4.2 Magnetic materials with their types

Magnetic materials are categorized into five kinds based on their net magnetic moment and spin orientations;**Figure-6.**; namely: a) Diamagnetic materialsb) Paramagnetic materialsc) Ferromagnetism materials d) Antiferromagnetism materials e) Ferrimagnetism materials

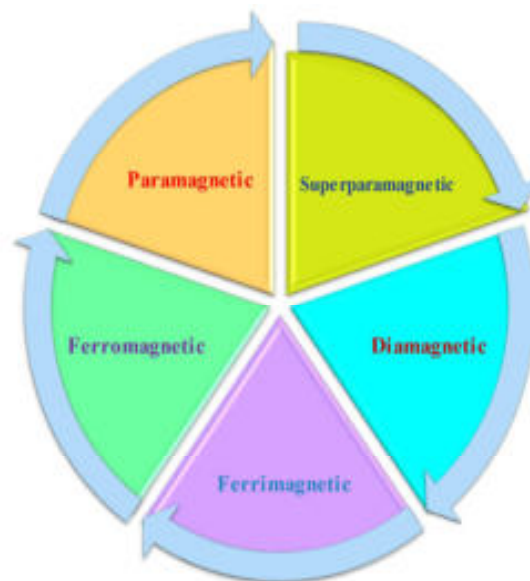


**Figure-6.Type of magnetic materials.**

To classify the materials, let us know some distinguishing properties of each of them. An atom is said to be magnetic if it carries a permanent magnetic moment. Every substance is formed from an assembly of atoms which can be either magnetic or non-magnetic. In the case of magnetic materials, the direction and sometimes the modulus of the magnetic moment can depend upon the particular environment of each atom. This environment depends upon the nature of the material, temperature, and applied magnetic field. The behavior of each material can be explained based on its response to the applied magnetic field and temperature.

### a) Diamagnetic materials

Diamagnetic materials have no magnetic moment since their spin orientations are paired. Furthermore, because these materials oppose applied magnetic fields significantly, their magnetization is in the opposite direction of the applied magnetic field[17]. Diamagnetism refers to the magnetism displayed by certain materials.



Diamagnetism is a very weak magnetization phenomenon of materials caused by electron spin and orbital mobility. When a magnetic field is given to an atom, the orbital motion of the electrons is altered, resulting in the induction of a weak magnetic moment opposing the field[18]. According to Lenz's law, the induced current produces an induced flux in the opposite direction of the applied field change[19]. The diamagnetic susceptibility and, as a result, magnetization is both exceedingly low and negative. Antimony, bismuth, mercury, gold, and copper are some examples of diamagnetic substances[20].

### b) Paramagnetic materials

Paramagnetic materials are materials that tend to get weakly magnetized in the direction of the magnetizing field when placed in a magnetic field[21]. Paramagnetic materials have a permanent dipole moment or permanent magnetic moment and spins are oriented in all directions[17]. After removing the applied field, however, as seen in **Figure-7**, the materials may lose their magnetism. The spin orientations of the electrons are randomized by thermal motion. Paramagnetism is due to the magnetic moments arising from the individual ions, atoms, or molecules which contain an odd number of electrons or because of an inner unfilled electron shell. The magnetism of materials that are just slightly attracted to an external magnetic field is known as paramagnetism[21]. The magnetic moment in these materials has negligible interaction with each other and can orient themselves freely in any direction. Thus, in some materials, the permanent magnetic moments of the atoms or ions are acted upon individually with no interaction among them, this effect is called Paramagnetism. Materials containing unpaired spin atoms are effectively paramagnetic. Paramagnetic substances include NO, O<sub>2</sub>, Mg, and Cesium, to name a few[20].

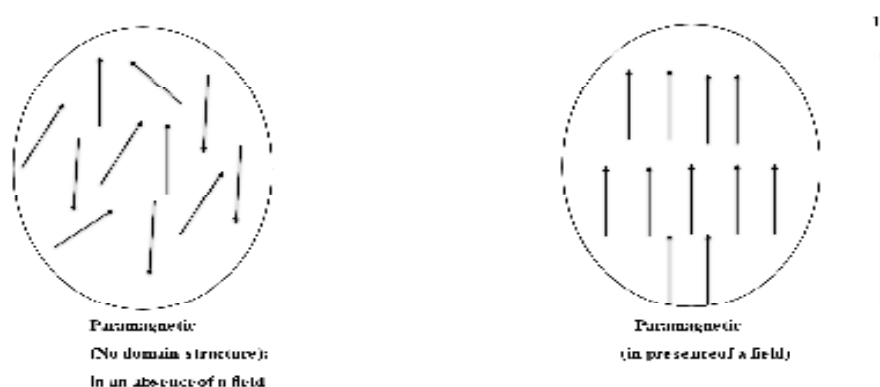


**Figure-7. Comparison of the orientation of magnetization (i.e., magnetic moment) of paramagnetic nanoparticles in the presence and absence of an external magnetic field (H).**

### c) Ferromagnetic materials

Even in the absence of an external magnetic field, ferromagnetic materials exhibit a spontaneous net magnetization at the atomic level. When subjected to an external magnetic field, ferromagnetic materials become strongly magnetized in the direction of the field[17]. Ferromagnetic materials are aggressively attracted by a magnet[21]. Even if the external magnetizing field is removed, these materials will keep their magnetization for a period of time. In these materials, the individual moments of the atoms or ions are strongly coupled and are more or less parallel to each other even in the absence of a magnetic field, so-called positive exchange interactions. Ferromagnetism (FM) occurs when a substance is powerfully drawn to a magnet and magnetization in the field direction[21]. These results in a very large macroscopic moment. It is a spontaneous magnetization of small regions of material that exists even in the absence of an external magnetic field. Ferromagnetism occurs when paramagnetic ions in a solid, lock together in a small region in which all magnetic moments are along the same direction. Such a region is called a domain. When a ferromagnetic sample is not exposed to an external magnetic field, the domains are randomly oriented, yielding a net magnetic moment of zero. When the sample is placed in an external magnetic field, the domains tend to align along the direction of the field giving the net magnetization shown in **Figure-8**. If the temperature of the ferromagnetic substance is increased, at a sufficiently high temperature the domain structure breaks down and the ferromagnetic substance becomes paramagnetic. This temperature is called Curie temperature ( $T_c$ ).

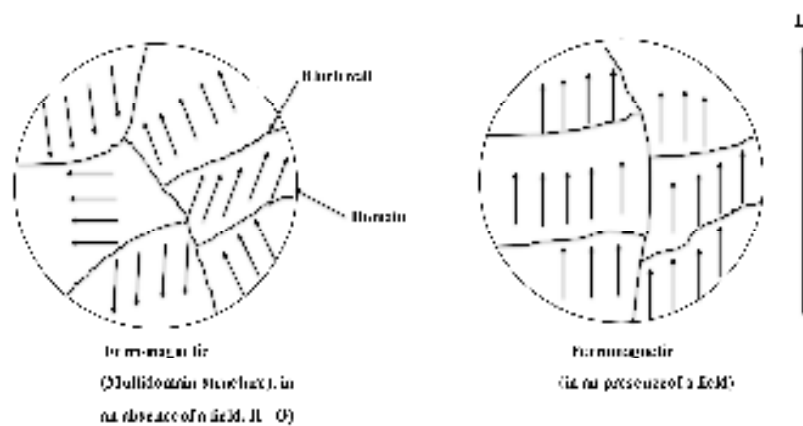


**Figure-8. Comparison of the orientation of magnetization (i.e., magnetic moment) of ferromagnetic (bulk) nanoparticles in the presence and absence of an external magnetic field ( $H$ ).**

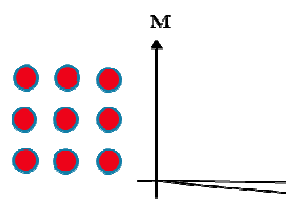
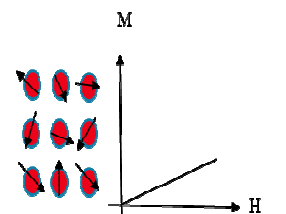
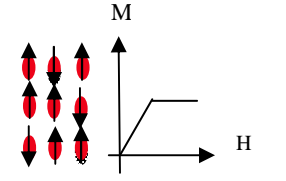
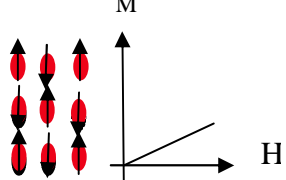
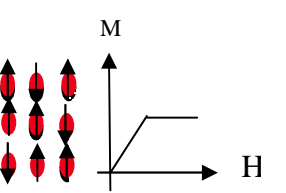
#### **d) Anti-ferromagnetic materials**

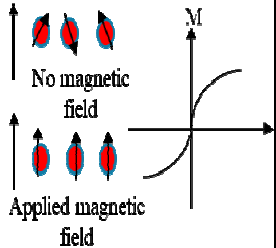
Antiferromagnetic materials are materials that exhibit antiferromagnetism. When these materials are exposed to a high magnetic field, they become weakly magnetised in the direction of the field. This is known as antiferromagnetism. This is a weak form of magnetism similar to that of paramagnetism with a weak and positive susceptibility. Several materials show interesting modifications of ferromagnetic behavior[22]. These materials are characterized by two interlocking sets of atoms, which have the spin lining up the character of ordinary ferromagnetic substances. In some materials like MnO, the two sublattices have identical magnetic moments but are opposite in direction. These orientations are due to exchange forces between adjacent atoms to have anti-parallel spin orientations. Hence such materials show very less gross external magnetism. Such materials are called anti-ferromagnetic materials. If they are heated sufficiently, at high temperature, thermal agitation overcomes the interaction effects of the material which shows susceptibility similar to that of paramagnetic materials. anti-ferromagnetic materials have zero net magnetic moments[21].

#### **e) Ferrimagnetic materials**

These materials are also referred to as partially antiferromagnetic due to the uncompensated magnetic spin moment. The resultant of two sublattices produces magnetization in this situation. Each sublattice behaves as an individual ferromagnet within which moments are aligned parallel. These sublattices are alternately arranged with one another. There will be a strong interaction between the two sublattices in opposite directions so that it results in a total magnetic moment equal to the difference between their magnitudes. Below a certain temperature, materials exhibit spontaneous magnetization. Thus, the class of materials with unequal and opposite spin systems has been named ferrimagnetism and the materials are so-called **ferrites**. Above certain high temperatures below  $T_C$ , these materials behave as paramagnetic due to the cancellation of magnetic moments. Also, the thermal variability of the reciprocity is almost linear at extremely high temperatures, but they move away from linear behavior as the temperature approaches the Curie point. The distinguishing properties of all the above magnetic materials such as the orientation of spin moments, magnetization, and susceptibility with varying magnetic fields and temperatures are tabulated in **Table-1** below [20-23].

**Table-1. Classification of magnetic materials.**

Type of Magnetism	Susceptibility/ Effect of the external field	Atomic / Magnetic Behavior/Example	
Diamagnetism	Small & Diamagnetic material has a negative magnetic Susceptibility. Weakly repelled by a magnet. Net magnetization is zero.	Atoms have no magnetic moment e.g., $H_2$ , $N_2$ Permeability $\mu < 1$	
Paramagnetism	Small & paramagnetic material has a negative magnetic Susceptibility. Weakly attracted by a magnet.	Atoms have randomly oriented magnetic moments e.g., NO, $O_2$ and Cesium Permeability $\mu > 1$	
Ferromagnetism	Large & ferromagnetic material has a positive magnetic susceptibility. Strongly attracted by a magnet.	Parallel aligned magnetic moments e.g., $Mn_3O_4$ Permeability $\mu \gg 1$	
Antiferromagnetism	Small & ferromagnetic material has a positive magnetic susceptibility. Weak attraction,	Anti-parallel aligned equal magnetic moments e.g., NiO, $Cr_2O_3$ , MnO Permeability $\mu > 1$	
Ferrimagnetism	Large & ferromagnetic material has a positive magnetic susceptibility. Strong attraction	Anti-parallel aligned unequal magnetic moment. eg., $Fe_3O_4$ , $\gamma-Fe_2O_3$ , $BaFe_{12}O_{19}$ . Permeability $\mu \gg 1$	

Superparamagnetism	Superparamagnetic $\text{Fe}_3\text{O}_4$ nanoparticles with only a single magnetic domain exhibit high magnetic susceptibility. The susceptibility of a superparamagnetic material is not near that of a ferromagnetic material	Randomly oriented magnetic moments in the absence of applied magnetic field, but when the applied magnetic field is applied to them then spins are aligned in parallel to each other.	
--------------------	--	---	---

#### f) Superparamagnetic materials

Superparamagnetic materials, which are made up of extremely small magnetic grains or nanoparticles, are gaining popularity, particularly in biological applications. Their numerous promising uses, such as anticancer magnetic hyperthermia, magnetoreception, magnetic resonance imaging, and ferrofluids for liquid sealing, efficient heat transfer, and damping, have sparked attention. Single-domain magnetic (para or ferro or ferri) particles are also called superparamagnetic nanoparticles and the concerned phenomenon is called superparamagnetism[24]. A superparamagnetic material's susceptibility is not comparable to that of a ferromagnetic material. Single-domain magnets are found in all superparamagnets, however not all single-domain magnets exhibit superparamagnetic activity[25]. They are found in single-domain nanoparticles and are typically found in small ferromagnetic or ferrimagnetic nanomaterials. Such magnetism is a miracle that occurs in ferromagnetic nanoparticles below a certain size to produce single-domain particles, and it is a magnetic nanomaterial's unique importance[26]. A superparamagnetic material's susceptibility is not comparable to that of a ferromagnetic material. Single-domain magnets are found in all superparamagnets, however not all single-domain magnets exhibit superparamagnetic activity, as shown in **Figure-9**[27]. SPIONs are a form of iron oxide nanoparticle that exhibit superparamagnetism where a material shows magnetic properties only when under the influence of an external magnetic field.

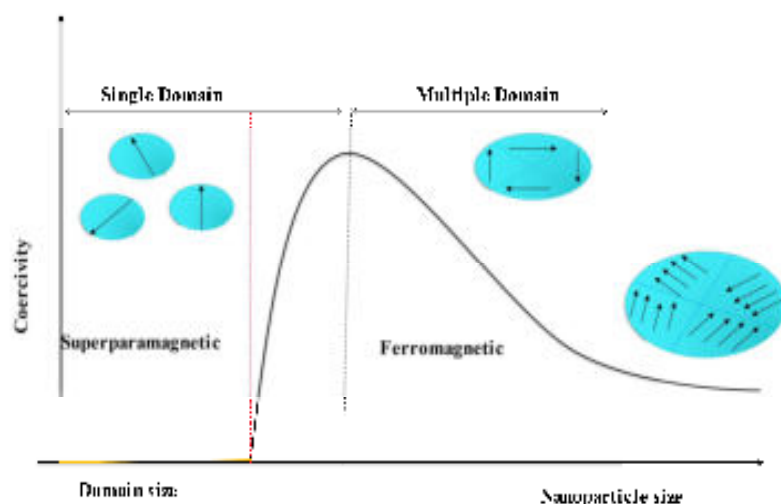


**Figure-9. Magnetic domain structure from Superparamagnetism to ferromagnetism.**

When ferromagnetic or ferrimagnetic materials are in the form of sufficiently small nanoparticles, superparamagnetism arises. Because of their large size, bulk materials essentially include several magnetic domains[28]. Small enough NPs, on the other hand, are single-domain particles, which can be thought of as a single gigantic magnetic moment made up of all the magnetic moments of the atoms that make up the nanoparticle.

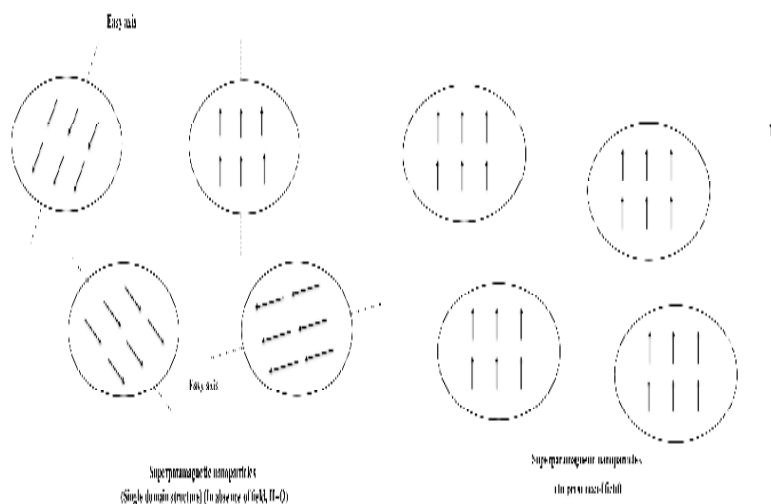


**Figure-10. Comparison of the orientation of magnetization(i.e., magnetic moment) of superparamagnetic nanoparticles in the presence and absence of an external magnetic field(H).**

For biomedical applications, superparamagnetic NPs are preferable over ferri and ferromagnetic NPs because they do not retain any magnetization once the magnetic field is withdrawn as shown in **Figure-11**. As the field intensity increases, the squares show the orientation of the moment of single-domain nanoparticles[28].

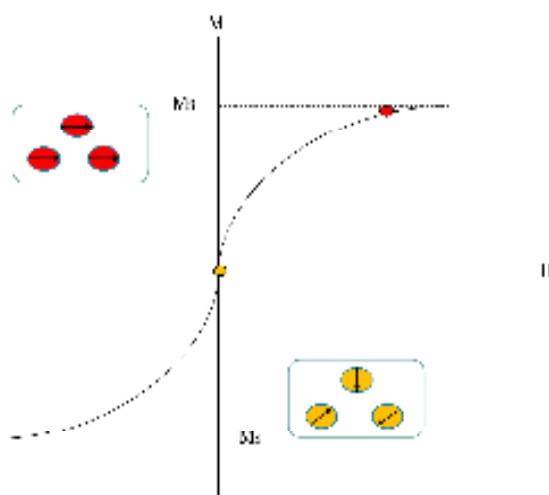


**Figure-11.**A superparamagnetic material's typical curve.

## 5. HYPERTHERMIA

The term "hyperthermia" is derived from two Greek words, "hyper" and "therme," which indicate "rising" and "heat," respectively, because this condition is indicated by an increase in body temperature[29]. Cancer treatment options include hyperthermia (HT), chemotherapy, radiotherapy, surgeries, immunological, and gene therapy. HT is considered to be an artificial method of elevating bodily tissue temperature by raising the temperature from outside sources to prevent malignancy cells from growing further or to eradicate cancerous cells. HT has emerged as a viable therapeutic tool for the successful treatment of cancer, with a focus on generating heat at the tumor site to alter cellular machinery. Its method of action is based on the idea that raising the temperature from 37 to 42-45°C can cause tumor cell death by activating specific intracellular and extracellular degradation pathways. (This certainly shows a growing interest in the potential of MHCT among cancer researchers around the world. Despite recent advances, MHCT has not yet become part of cancer treatment care standards. Researchers are working harder to do so[30]. The ideal delivery mechanism for hyperthermia would be non-invasive, tissue-specific, and capable of precisely localized, high-intensity heating in deep

tissues. Gilchrist et al. first proposed magnetic materials for hyperthermia in the 1950s, and in the intervening years, magnetic nanoparticles are capable of meeting each of these requirements[31]. HT has been delivered by various methods and in conjunction with numerous agents for a variety of illnesses over several decades. HT has shown effectiveness in treating a wide range of tumors, including tumors of the head and neck, breast, brain, bladder, cervix, rectum, lung, esophagus, vulva, and vagina, as well as non-melanoma and melanoma skin cancer and sarcoma. Magnetic nanoparticle-mediated hyperthermia has emerged as a promising modality for cancer treatment due to the unique heat-generating properties of SPIONs under an alternating magnetic field. During hyperthermia, the body tissue temperature increases to around 40 to 45°C by delivering heat obtained from external sources to destroy cancerous cells or to prevent their further growth. Several studies have revealed that hyperthermia acts synergistically with radiotherapy or chemotherapy, providing a promising strategy to improve cancer therapy.

### 5.1 Classification of hyperthermia

There are three essential clinical techniques of high temperature application comprising of whole-body hyperthermia (WBH), regional hyperthermia (RHT), and local hyperthermia (including superficial local and interstitial local hyperthermia) (LHT) are shown in **Figure-12**. Energies used to heat tumors include microwaves (wavelengths ranging from 433 to 2450 MHz), radiofrequency (ranging from 100 KHz to 150 MHz), ultrasound, hot water perfusion (tubes, blankets), infrared radiators, nanoparticles, ferromagnetic seeds, and resistive wire implants[29].



**Figure-12. Types of hyperthermia treatment.**



#### **a. Local hyperthermia**

Currently, only local hyperthermia is considered for magnetic fluid hyperthermia. For this purpose, MNP in a carrier fluid is placed inside the tumor through direct injection or tumor-specific antibody targeting, after which the tumor is exposed to an alternating magnetic field. The hyperthermia technique has not been very effective in treating serious cancers due to basic problems associated with local hyperthermia; such problems include heterogeneous temperature dispensation in tumor mass and the inability to prevent overheating at the deep-seated tumor area[32].

#### **b. Regional hyperthermia**

In regional hyperthermia, a part of the body, such as an organ, limb, or body hole is heated. It is not hot enough to destroy cancer cells completely. In regional hyperthermia, doctors use heat to treat large areas of the body, including the cavity, organ, or limb. Also, the deep tissue approach, regional perfusion, and continuous hyperthermic peritoneal perfusion are important methods used in regional hyperthermia.

#### **c. Whole-body hyperthermia**

Whole-body hyperthermia: is used to treat metastatic cancer that has spread throughout the body[26]. Cancer that has spread throughout the body can be treated with whole-body hyperthermia. Such kind of hyperthermia involves inserting you in a thermal chamber or covering you in hot water blankets to temporarily increase your body temperature to 41-42°C.

### **5.2 Magnetic hyperthermia**

The magnetic field used in MHT promotes magnetic nanoparticle localization/accumulation in malignant tissues and boosts selectivity. The alternating magnetic field causes the nanoparticles to vibrate, producing heat that can reach 40-43°C and destroy the cancerous tissues are shown in **Figure-13**. Magnetic hyperthermia is one of the most promising cancer therapies approaches due to its deep tissue penetration and localized focused restricted heating provided by MNPs[33]. Magnetic NPs have been used in a variety of applications, including magnetic data storage, permanent magnets, microwave absorption, magnetic refrigeration, self-healing materials, and tissue engineering, to name a few. Thanks to their high surface-to-volume ratio, unique tunable characteristics, colloidal stability, and biocompatibility, iron oxide MNPs have expanded their biomedical applications to advanced therapies since their initial approval as MRI contrast agents and medications to treat iron deficiency. The improvement in heating efficiency would be especially advantageous for biological applications dependent on local heat generation, such as magnetic hyperthermia, as well as heat-triggered drug delivery and heat-mediated cell signaling[34]. The important specifications of magnetic

hyperthermia are that energy is absorbed from the alternating magnetic field and transformed into heat through one or a grouping of the next mechanisms. Therefore, hyperthermia can be summarized as follows: (1) Generation of eddy currents in a material of low electrical resistivity, (2) reversal of the magnetization inside a magnetic material, and (3) rotation of the magnetization material relative to its surrounding.

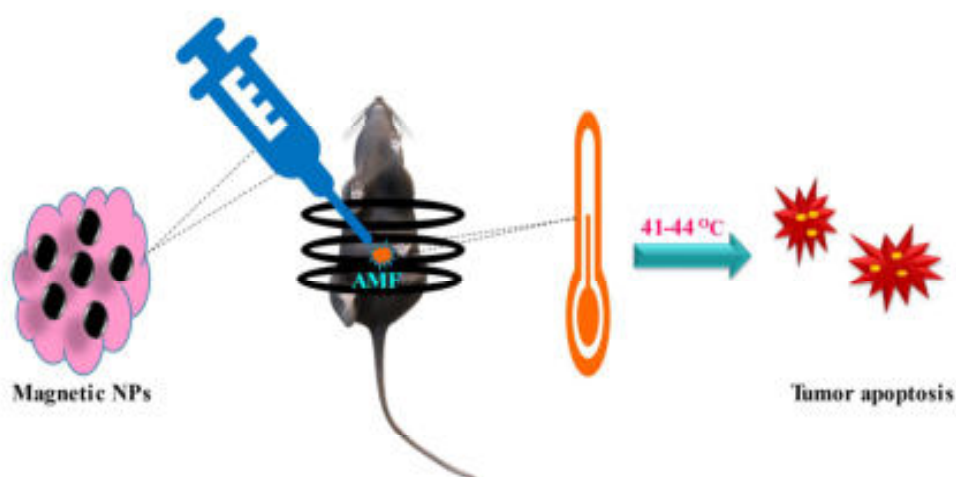


**Figure-13. In vivo magnetic hyperthermia treatment.**

## **6. METAL OXIDE-BASED COMPOSITES FOR MAGNETIC HYPERTHERMIA APPLICATION**

Magnetic nanoparticles have been explored for medical applications due to their unique physical as well as magnetic properties. Host-guest structured nanocomposites are very interesting in the biomedical field. Host-guest structured nanocomposites consisting of magnetic iron oxide host other metal oxide guest have an attraction in particular unique magnetic properties, low cytotoxicity, and also provide high surface area. These properties are more beneficial in the medical field. The nano dimensions mixed metal oxide system with contrast in magnetic crystalline anisotropy and exchange coupling between host and guest have become increasingly popular for biomedical applications. Patil et al. have studied the core-shell structured particles, especially magnetic materials, which have attracted attention because they offer new nanostructured materials with diverse applications for their unique magnetic responsivity and chemically liable surface. Qing Song et al. studied that the magnetic properties of magnetic spinel ferrites  $\text{CoFe}_2\text{O}_4$  and  $\text{MnFe}_2\text{O}_4$  nanocrystals with core-

shell nanocrystals possess very unique properties. Core-shell nanomaterials are extremely important because they offer different properties as well as multifunctionality behaviors. Shell is utilized as a protective shield for sensitive core material and having a biocompatible shell around toxic host material helps to reduce the toxicity of core material. Xue gang Lu et al. studied well by using multifunctional triple-porous  $\text{Fe}_3\text{O}_4@\text{SiO}_2$  superparamagnetic behavior with saturation magnetization of  $52 \text{ emu g}^{-1}$ , large surface area  $426 \text{ m}^2\text{g}^{-1}$ , temperatures of physiological saline suspensions containing  $\text{m-Fe}_3\text{O}_4@\text{dm-SiO}_2$  microspheres were increased to  $41^\circ\text{C}$ ,  $48^\circ\text{C}$  and  $56^\circ\text{C}$  when the colloidal concentrations are 5, 7.5, and  $10 \text{ mg mL}^{-1}$ , respectively [35]. Yang Qu et al. got a good hyperthermia result by using  $\text{Mn}_x\text{Zn}_{1-x}\text{Fe}_2\text{O}_4$  NPs with a high specific absorption rate of  $1618.8 \text{ W/g}$ , magnetic saturation of  $23.7 \text{ emu/g}$ , a mild hyperthermia temperature range near  $43^\circ\text{C}$  [36]. Tonelli et al.,  $\text{Co}_3\text{O}_4@\text{TiO}_2$ ,  $\text{Co}_3\text{O}_4$  cores show saturation magnetization  $11.0 \text{ emu/g}$ , hyperthermia temperature range  $41\text{--}42^\circ\text{C}$ . Runsheng Wang has achieved real results as he prepared  $\text{Zn}_{0.5}\text{Fe}_{2.5}\text{O}_4$  NPs coated with silica for magnetic hyperthermia agents using a one-pot technique. High specific absorption rate ( $1083 \text{ Wg}^{-1}$ ,  $f = 430 \text{ kHz}$ ,  $H = 27 \text{ kAm}^{-1}$ ), with large saturation magnetization ( $M_s = 85 \text{ emu g}^{-1}$ ), good colloidal stability, and minimal cytotoxicity are characteristic of NPs.

## 7. METHODS FOR MEASURING THE MAGNETISM OF THE MAGNETIC MATERIALS

Magnetization of the materials is studied using different tools including heating capacity: induction heating system, and Mossbauer measurements as well.

### 7.1 Vibrating sample magnetometer

Vibrating-sample magnetometry (VSM) is a scientific technique for determining magnetic characteristics [5]. VSM includes the vibration of magnetic material inside a homogenous magnetic field  $H$ , which generates an electric current in sensing coils that are suitably arranged [37]. In comparison to an alternating gradient magnetometer, the VSM is insensitive to sample mass and size across a wide range. The sample is put into a steady uniform external magnetic field in this technique, which produces magnetization in the sample as shown in **Figure-14**. When the magnetized sample is vibrated, it causes disturbances in the external magnetic field. To measure these disturbances, a collection of coils or magnetic field sensors can be positioned around the sample. In the case of coils, for example, magnetic flux penetrating the coils will vary, leading to the formation of an electromotive force in the coils. The emf generated in coils depends on (a) the amplitude and frequency of vibration, and (b) the external magnetic field for a given coil shape.

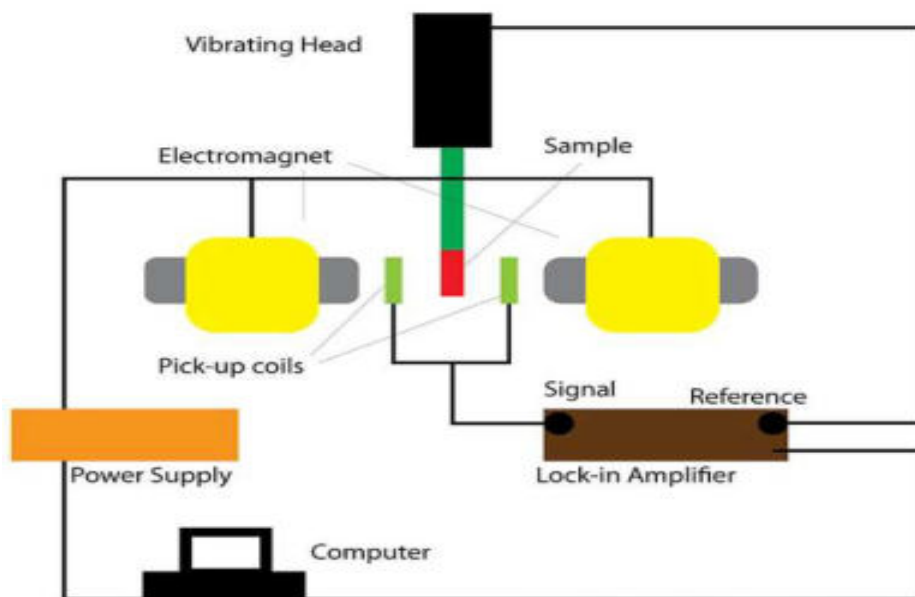


Figure--14. Simplified VSM schematic.

## 7.2 Induction heating system

Nowadays, due to its benefits in terms of efficiency, quick heating, safety, cleanliness, and precise control, induction heating (IH) technology is the heating method of choice in many industrial, home, and medical applications. Figure-15 shows three essential technologies that have advanced, allowing the creation of highly dependable and affordable systems, making this technology widely used and accessible.

Among the many benefits of IH, the following are widely acknowledged

- **Fast heating:** IH technology rapidly warms the induction target, preventing wastage of heat and slashing heating times thanks to high power densities and little thermal inertia.
- **Efficiency:** Obtaining efficiency levels of above 90% is made possible by modern, effective designs of the coil and the power converter, greatly enhancing the performance of traditional heating methods. Furthermore, because just the induction target is heated, there is less heat lost through the ambient environment and surrounding materials, allowing for the achievement of high temperatures.
- **Controlled heating:** The power applied by the IH system and its position may be precisely regulated by designing the coil, the power converter, and its management. As a result, complex functionality such as local heating, specified temperature profiles, and so on may be implemented.

- **Improved industrial process:** IH consistency and repeatability improve the quality of the process and increase process productivity. Furthermore, because IH is a contactless heating method, the induction target is not impacted by the heating instrument, i.e., the coil, ensuring quality.
- **Cleanness and safety:** Since IH heats directly the induction target, the temperature of the surroundings of the heating area is lower, avoiding burning other materials.

IH technology's medical applications are now the third important area of application. IH was initially used to manufacture and sterilise several surgical tools since it is a safe, quick, and portable heat source.

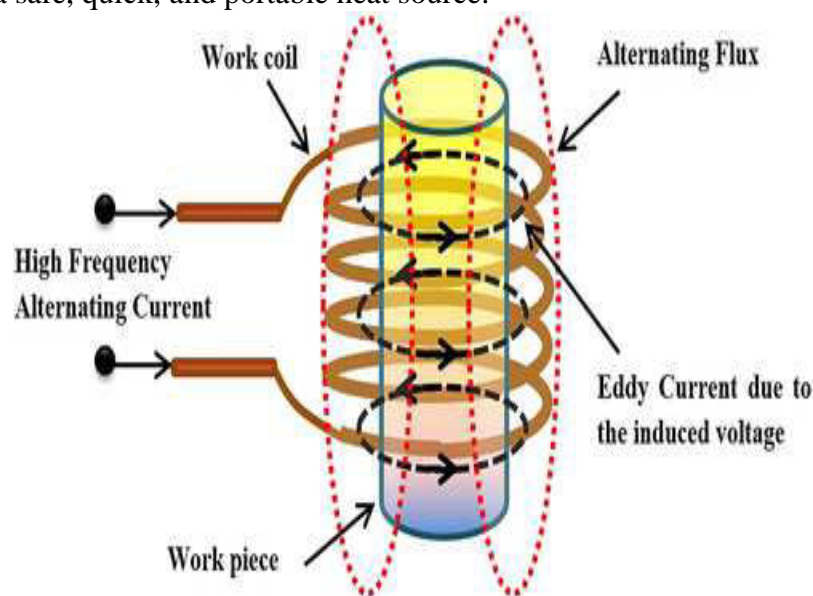


**Figure-15. Schematic representation of the induction heating system.**

### 7.3 Mossbauer spectroscopy

Mossbauer spectroscopy is a spectroscopic technique that measures the magnetic properties of materials using gamma rays. Mossbauer spectroscopy gives an idea about symmetry, oxidation state, surface spins, magnetic ordering of Fe atoms, thermal unblocking, magnetic anisotropy energy, and distinguishing between iron oxides. Magnetically organized materials are used in a variety of applications, including motors, magnetic imaging, and magnetic recording. As a result, hard magnetic materials, magnetic thin films, and molecular magnets have all undergone significant improvements [38]. Mossbauer-effect spectroscopy, which examines solid-state materials at specific atomic locations and offers microscopic information on their magnetic and electronic properties, has evolved from a laboratory curiosity

to a mature spectroscopic technique as a result of this. The Mossbauer method gives unique information about magnetic properties, but the combination with other experimental methods such as thermomagnetic ones, neutron diffraction, etc. is essential. One of the most common uses of mossbauer spectroscopy has been the investigation of the magnetic characteristics of materials. The 14.4 keV transition in  $^{57}\text{Fe}$  has been used in the majority of research.

There are several reasons for the popularity of this isotope in the study of magnetic materials. The major reason is the presence of iron as a constituent in most of the scientifically and technologically important materials. Even other materials not containing iron can be studied by the introduction of very small amounts of  $^{57}\text{Fe}$  as a substitutional sound. The iron isotope has also nuclear properties that facilitate the measurements: low energy, long lifetime, adequate nuclear moments, and usually strong lattice bonding (high Debye temperature) and long-lived parent activity  $^{57}\text{Co}$ . For this reason, we will in the following concentrate mostly on the application of  $^{57}\text{Fe}$  mossbauer spectroscopy in the study of magnetic materials. The number of magnetic moments, their spatial arrangement, and their evolution with temperature are all required for a thorough description of a material's magnetic state. Using Mossbauer spectroscopy, Gabbasov et.al. have carefully studied the iron oxide nanoparticles covered with oleic polymers. Mossbauer spectroscopy at RT has observed a magnetically ordered state of the Li-Zn ferrite samples. With the help of Mossbauer spectroscopy, Sundar and his colleagues discovered the spatial structure and magnetic properties of the cubic iron oxide NP formed in zeolite.

## 8. CONCLUSION

The different magnetic bare metal oxide, mixed metal oxides, and their composites for hyperthermia therapy as well as the advancement of nanotechnology in the field of cancer treatment were highlighted. Initially, the basic information of hyperthermia, types of hyperthermia, metal oxide nanoparticles, and their use in cancer treatment have been stated well. Among the various types of treatments, magnetic hyperthermia is one of the most promising treatments not only for cancer but also for pain, wounds, arthritis, and so on. Magnetic nanoparticles are the most attractive choice for magnetic hyperthermia because of their properties such as strong biocompatibility, minimal toxicity, ease surface functionality, high SAR value, etc. The efficiency of magnetic hyperthermia treatment can be improved by optimizing particle distribution, the frequency of alternating magnetic fields, nanoparticle size, type of magnetizations, etc. The various measurements for studying the magnetic properties of materials were discussed. In the end, it is concluded that magnetic hyperthermia would have the overriding advantages in terms of reasonable cost, ease of protocol, less complication, and minimum side effects to that of presently

available cancer treatments. Additionally, current developments on the most popular MNPs for use in biomedicine were reviewed.

## **9. CHALLENGES & FUTURE PERSPECTIVE**

We reviewed current progress in the synthesis, characterization, and possible uses of MNPs in this review. Various types of MNPs with attractive properties are being produced using several synthetic techniques. The primary goal of hyperthermia in these cancer treatments is to raise the temperature of the target tissue to near 42 to 44 °C. As a thermal mediator in cancer therapy, magnetic hyperthermia is being used in conjunction with nanoparticles. Maximizing the heating capacity of nanoparticles as well as controlling the local temperature of the tumor are the two main challenges of magnetic hyperthermia. Current studies have investigated the excellent hyperthermia performance of magnetic iron oxide nanoparticles when internalized into tumor cells. Hyperthermia is a promising way to improve cancer treatment, but it is largely an experimental technique at this time. It requires special equipment and a doctor and treatment team who are skilled in using it. Because of that, it's not offered in all cancer treatment centers. Many clinical trials of hyperthermia are being done to better understand and improve this technique. Researchers continue to look at how hyperthermia is best used along with other cancer treatments to improve outcomes. Studies are also looking at ways to reach deeper organs and other sites that cannot be treated with hyperthermia at this time. Current studies are looking at how it might work to treat many types of cancer, including the following: Bladder, Melanoma, head and neck, Kidney, Liver, Lung, Leukemia, and Neuroblastoma. Results from studies on laboratory animal models and initial human clinical trials have been very promising and suggest that hyperthermia may have a vital role in future cancer treatment. Two major technological challenges make hyperthermia therapy complicated: the ability to achieve a uniform temperature in a tumor, and the ability to precisely monitor the temperatures of both the tumor and the surrounding tissue. Advances in devices to deliver uniform levels of the precise amount of heat desired, and devices to measure the total dose of heat received, are hoping for.

## **CONFLICTS OF INTEREST**

The author declares that there is no conflict of interest regarding the publication of this article.

## **ACKNOWLEDGMENT**

Author Amol B. Pandhare gratefully acknowledges Mahatma Jyotiba Phule Research Fellowship (MJPRF-2021) for financial support. And also, the author (Dr. R. P. Patil) is thankful to Shivaji University, Kolhapur for financial assistance through research



project no. SU / C & U. D. Section / Prop. No. 8 / 1403 Dated 24th March 2021 under Research Initiation Scheme.

## REFERENCES

1. Fan,X., Jiao,G., Zhao,W., Jin,P.,Li,X. (2013) *Nanoscale*, 5,1143–1152.
2. Jia,W. L., Xu,L. F., Xu,W. J., Yang,M., Zhang,Y. W. (2022) *Nanoscale Advances*, 4,3183–3200.
3. Baig,N., Kammakakam,I., Falath,W., Kammakakam,I. (2021)*MaterialsAdvances*, 2,1821–1871.
4. Granados-Miralles,C., Quesada,A., Saura-Múzquiz,M., Andersen,H. L., Fernández,J. F., Christensen,M. (2020) *Materials Chemistry Frontiers*,4, 1222–1230.
5. Mourdikoudis S., Pallares R. M., Thanh N. T. (2018) *Nanoscale*,10, 12871–12934.
6. Shi,D. A., Sadat,M. E., Dunn,A. W., Mast,D. B. (2015) *Nanoscale*, 7, 8209–8232.
7. Ha,P. T., Le,T. T., Bui,T. Q., Pham,H. N., Ho,A. S., Nguyen,L. T.(2019) *New Journal of Chemistry*, 43,5404–5413.
8. Porret,E., Guével,X., Coll,J. L. (2020)*Journal of Materials Chemistry B*, 8, 2216–2232.
9. Ortega,D., Pankhurst,Q. A. (2012)*The Journal of Physical Chemistry C*, 9,60–88.
10. Sharmiladevi,P., Girigoswami,K., Haribabu,V., Girigoswami,A. (2021)*Materials Advances*, 2, 2876–2891.
11. Lizio,M. G., Boitor,R., Notingher,I. (2021) *Analyst*, 146, 3799–3809.
12. Huang,J., Lin,L., Sun,D., Chen,H., Yang,D., Li,Q. (2015), *Chemical Society Reviews*, 44, 6330–6374.
13. Fu,S., Sun,Z., Huang,P., Li,Y., Hu,N. (2019)*Nano Materials Science*, 1, 2–30.
14. Yaqoob,A. A., Umar,K., Ibrahim,M.M. (2020)*Applied Nanoscience*, 10, 1369–1378.
15. Naghdi,M., Metahni,S., Ouarda, Y., Brar, S. K., Das, R. K., Cledon, M.(2017)*Nanotechnology for Environmental Engineering*, 2, 1–17.
16. Visser,G. W.,Windhors,A. D. (2021) *RSC Advances*, 11, 27978–27991.
17. Rikken,R. S., Nolte,R. J., Maan,J. C., Van Hest J. C., Wilson D. A., Christianen, P. C. (2014) *Soft Matter*, 10, 1295–1308.
18. Cardona,J. E., Louaguef,D., Gaffet,E., Ashammakhi,N., Alem,H. (2021)*Materials Chemistry Frontiers*, 5, 6429–6443.
19. Ortega,D. A.,Pankhurst,Q. A. (2012) *Journal of Physical Chemistry E*, 1, 60–88.



20. Hedayatnasab,Z., Abnisa,F., Daud,W. M. (2017) *Materials & Design*, 123, 174–196.
21. Shukla,V., (2020) *Nanoscale Advances*, 2, 962–990.
22. Islam,M. A.,Hossain,A. K.(2022) *RSC Advances*, 12, 17362–17378.
23. Plakhotnik,T., Aman,H., Zhang,S., Li,Z. (2015) *Journal of Physical Chemistry C*, 119, 20119–20124.
24. Soetaert,F., Korangath,P., Serantes,D., Ivkov,R., (2020)*Advanced Drug Delivery Reviews*, 163, 65-83.
25. Laurent,S., Dutz,S.,Häfeli,U. O.,Mahmoudi,M. (2011) *Advances in Colloid and Interface Science*, 166, 8–23.
26. Lekha,G. M.,George,S. (2020)*Colloidal Metal Oxide Nanoparticles*, 100, 289-335.
27. Hervault,A.,Thanh,N. T.(2014) *Nanoscale*, 6, 11553–11573.
28. Gupta,R., Sharma, D., (2019) *ACS Chemical Neuroscience*, 10, 1157–1172.
29. Deatsch,A. E.,Evans,B. A.,(2014) *Journal of Magnetism and Magnetic Materials*, 354, 163–172.
30. Bañobre-López,M., Teijeiro,A., Rivas,J. (2013) *Reports of Practical Oncology & Radiotherapy*, 18, 397–400.
31. Gupta,R.,Sharma,D. (2021) *Nanoscale Advances*, 3, 3663–3680.
32. Lu,X., Liu,Q., Wang,L., Jiang,W., Zhang,W., Song,X.(2017)*Journal of Materials Chemistry A*,83, 32049–32057.
33. Qu,Y., Li,J., Ren,J., Leng,J., Lin,C., Shi,D. (2014)*Nanoscale*, 6, 12408–12413.
34. Agirre-Olabide,I., Kuzhir,P., Elejabarrieta,M. J., (2018) *Journal of Magnetism and Magnetic Materials*, 446, 155–161.
35. Ahmed,M. A., Hassan,H. E., Eltabey,M. M., Latka,K., Tatarchuk,T. R.(2018) *Physica B: Condensed Matter*, 530, 195–200.
36. Mourdikoudis,S., Pallares,R. M.(2018) *Nanoscale*, 832, 112–124.
37. Stefanos, M., Roger, P., Nguyen, T. (2018) *Nanoscale*,10, 12871-12934.

# One-Step Synthesis of Biomass-Derived Carbon Dots: Study of Optical Properties

Akanksha G. Kolekar<sup>a</sup>, Omkar S. Nille<sup>a</sup>, Shubham J. Kumbhar<sup>a</sup>, Priyanka S. Mahadar<sup>a</sup>, Sayali B. Lohar<sup>a</sup>, Govind B. Kolekar<sup>a</sup>, Gavisiddappa S. Gokavi<sup>a</sup>, Vishalkumar R. More<sup>b,\*</sup>

<sup>a</sup>Department of Chemistry, Shivaji University, Kolhapur 416 004 (MS) India.

<sup>b</sup>Department of Chemistry, The New College, Kolhapur 416 012 (MS) India.

\*Corresponding author: morevishalkumar@newcollege.ac.in

---

## ABSTRACT

*Carbon dots have demonstrated great potential as luminescent nanoparticles in bio applications as well as environmental pollutants analysis and water analysis. Although such nanoparticles appear to exhibit low toxicity compared to other metal luminescent nanomaterials. Today we know that toxicity of carbon dots (C Ds) strongly depends on the protocol of fabrication. In this work, aqueous fluorescent C-Ds have been synthesized from cinnamon by hydrothermal synthesis method. The synthesized CDs were first characterized by means UV - visible spectroscopy, spectrofluorometer, Fourier transform infrared spectroscopy (FTIR), and XRD.*

## KEYWORDS

*Cinnamon carbon dots (C-CDs), Hydrothermal, Fluorescent probe.*

.....

## 1. INTRODUCTION

Nanotechnology is the design, characterization, production, and applications of structures, devices, and systems by controlling shape and size at the nanometer scale. Nanotechnology is the study and manipulation of matter at an incredibly small size, generally between 1 and 100 nm, nanotechnology encompasses a very broad range of materials, manufacturing processes and technologies that are used to create and enhance many products [1,2]. Nanotechnology is part of the next wave of innovation in science and engineering that will transform many sectors including aerospace, energy, information technology, medicine, national defence and transportation [3]. Nanotechnology will enable the development of next generation materials that are stronger, cost effective, lighter and more durable than the materials used today. Nanotechnology also holds great promise for creating products for a more energy efficient world such as more energy efficient world, such as more efficient fuel cells, batteries and solar panels. Nanotechnology can provide solutions for cleaning contaminated soil and water, and it will play a critical role in transforming medicine and health care [4].

Carbon-based nanomaterials include fullerenes, carbon nanotubes, graphene and its derivatives graphene oxide and fluorescent carbon dots. Due to their unique structural dimensions and excellent mechanical, electrical, thermal, optical and chemical properties, these materials attracted significant interest in diverse areas including biomedical applications, environmental remediation forensic applications and many more [5,6]. The physical, chemical, optical, electrical and biological properties of nanomaterials are size dependent at the nano-level properties such as melting point, fluorescence, electrical conductivity, magnetic permeability and chemical reactivity changes as the function of the particles. Nanostructure shows sizes and shape subordinate physical and concoction properties which makes them reasonable in the different field applications.

Inherently safer chemistry for accident prevention these principle summarized as using nontoxic renewable precursors and solvent in CD synthesis that is safe to perform the synthesized CDs should be non-toxic and chemically stable. Although CDs synthesis is generally an energy intensive process lower energy synthesis method should be prioritized moreover given the possibility of the formation of several side products and intermediates one must consider their safety profile to ensure their proper disposal these principle will guide using the following subsection.

The variety of synthetic approach for CDs can be categorized into two main routes a) top down, b) bottom up methods including laser ablation, Arc discharge, electrochemical approach, microwave irradiation, chemical oxidation, carbonization, direct pyrolysis and hydrothermal reaction among all these methods the CDs synthesized via hydrothermal treatment is the most popular approach because the synthesis process is simple clean and economical, in this method the carbon yielding compounds are subjected to mild experimental condition and biomass and bio waste can be used to synthesize the CDs [7,8].

Owing to its low cost and ease of implementation hydrothermal synthesis is the most common and green process for CDs preparation this thermal mediated approach requires pressurized autoclave vessel's reaction temperature ranging from 120°C to 240°C and the reaction times of 3-12 hrs, in a typical synthesis [9,10]. The definition of green synthesis stipulates using water hydrothermal or benign organic solvents such as ethanol, DMF etc. these reaction parameters can be readily optimized to maximize product yield and application specific performance while minimizing energy requirements.

Fluorescent carbon dots are a type of novel carbon-based nanomaterial (generally the diameter < 10 nm) with a photoluminescent behavior since their discovery in 2004 the preparation of fluorescent carbon dots and their applications have been continually expanded with advanced optical and physico-chemical properties over other fluorescent nanomaterials [8,11]. The carbon dots have various advantages such as desirable size and excitation wavelength dependent

photoluminescence, photo stability, easy surface fictionalization, low toxicity. Carbon dots (CDs) have nearly spherical shapes having an amorphous and crystalline core with predominant  $sp^2$  carbon and oxidized carbon surface with carboxyl, hydroxyl groups etc. Recently, CDs have evolved tremendous interests in researchers as a potential candidate to substitute toxic metal-based Quantum dots (QDs) [12]. CDs were reported to have good biocompatibility, less toxicity, high photoluminescence (PL) intensity, high chemical stability and posse's excellent biological, physical and chemical properties, thus have great potential in various applications [10].

The diverse optical, chemical, size-dependent fluorescence, biocompatible, chemical inertness, and such excellent properties of fluorescent carbon dots makes it multifaceted applicative. Some selected applications are represented in given schematic [13].

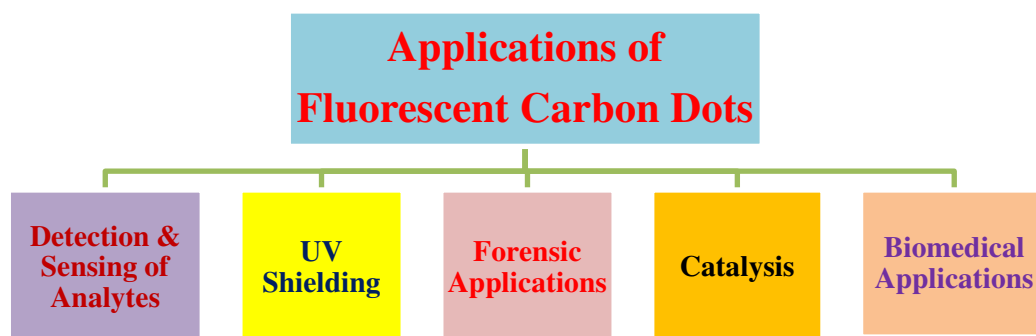


**Figure-1. Schematic showing multifaceted applications of fluorescent carbon dots.**

## **2. EXPERIMENTAL**

### **2.1 Materials and Chemicals**

All chemical reagents were of analytical reagent grade and used as received without further purification. All aqueous solutions of metal ions were prepared by using respective metal salts of analytical grade with distilled water.

### **2.2 Instrumentation**

The absorption spectrum was acquired at room temperature by using Specord 210 plus, Analytikjena UV-Vis spectrophotometer with the use of 1 cm quartz cuvette. The fluorescence measurements of C-CDs and solutions were made with PC based spectrofluorometer (Model- Jasco FP 8300, Japan). Equipped with xenon lamp source and 1 cm quartz cuvette. Both excitation and emission slits were fixed at 5 nm. High speed centrifugation model REMI R-24 was applied for centrifugation

operation. The pH of solution was measured with digital pH meter model LI-120 with a combined glass electrode.

### 2.3 Hydrothermal synthesis of cinnamon carbon dots (C-CDs)

In this process, we have used the kitchen material Cinnamon as a precursor material for synthesis of cinnamon carbon dots (C-CDs). Cinnamon the eternal tree of tropical medicine belongs to the lauraceae family cinnamon is one of the most important spices daily used by people all over the world cinnamon primarily contains vital essential oil and other derivatives such as cinnamaldehyde, cinnamic acid and cinnamate. The Fig. 1 showing the hydrothermal synthesis of cinnamon carbon dots (C-CDs).



**Figure-2. The schematic for the hydrothermal synthesis of cinnamon carbon dots (C-CDs).**

Here, we have used cinnamon as precursor material for the synthesis of CDs. 2 gm of crushed powder of cinnamon weighted and added in 10 ml of distilled water. This reaction mixture was taken in teflon lined hydrothermal and the temperature was set to be 180<sup>0</sup> C for 12 hrs. The completion of the reaction the teflon lined hydrothermal autoclave was allowed to cool up to room temperature and the solution was filtrated by using Whatman's No. 41 filter paper and diluted to 100 ml with distilled water. The synthesized cinnamon carbon dots (C-CDs) were purified by centrifugation at 8000 rpm for 20 min and then passed with 0.22 micrometer syringe filter. Finally, the successfully synthesized cinnamon carbon dots (C-CDs) were prepared in stock and stored in refrigerator for further use.

### 3. RESULTS AND DISCUSSION

#### 3.1 Characterization of Cinnamon carbon Dots (C-CDs)

The synthesized C-CDs are ascertained by wide range of spectroscopic, surface and microscopic techniques. Among them, some selective techniques are theoretically and C-CDs perspective described below.

#### 3.2 UV-Visible spectroscopy

The UV-Visible spectroscopy is useful characterization technique utilized to know the absorption band of the synthesized nanomaterials as a function of the wavelength. The absorption of light either from UV ( $\sim 200 - 400$  nm) or visible ( $\sim 400 - 800$  nm) region results in the movement of electrons from ground state to high energy excited state and gives distinct spectrum. The energy (wavelength) of absorbed light corresponds to the difference in energy between ground and excited state. Thus, reduction of nanomaterial size particle shifts the wavelength of absorption to blue region. The absorption peak position is useful to understand transitions ( $\pi-\pi^*$ ,  $n-\pi^*$ , and  $\sigma-\sigma^*$ ) and ultimately electronic structures of materials [14].

From the literature survey, it was observed that the absorption of CDs is depending on the type of synthetic method, precursor, and other experimental conditions [15]. Generally, CDs have some graphite carbon core and have different carboxyl, hydroxyl, and amine functional groups on their surfaces. Therefore, most of the absorption peaks are due to the electronic transitions.

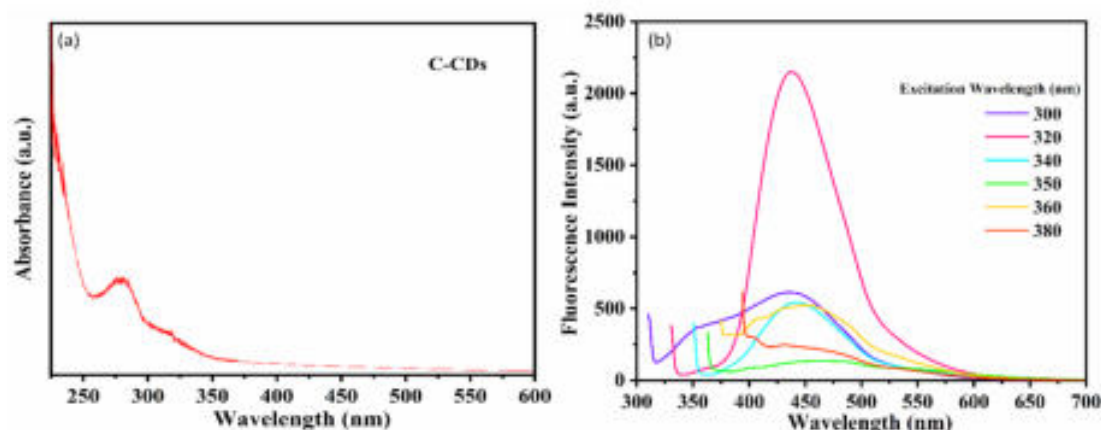


**Figure-3. (a) UV-Vis. Spectra of C-CDs, (b) Fluorescence emission peaks of C-CDs at different excitations.**

The optical properties of C-CDs were explored by UV-Visible and fluorescence spectroscopy. The absorption spectrum showed that the synthesized material showed characteristic peaks at 260 nm and a small hump at 320 nm. The absorption peak at 260 nm could be associated with the  $\pi-\pi^*$  transition of the C=C

core whereas the peak at 320 nm correlates to the  $n-\pi^*$  transitions of the ( $-\text{C}=\text{O}$ ) carbonyl group of C-CDs. Fig. 3 (a) represents the UV-Vis. spectra of C-CDs [14].

### 3.3 Fluorescence spectroscopy

**Figure 3 (b)** indicates the emission spectra of C-CDs at different excitation wavelengths. It indicates maximum emission wavelength lies at 446 nm to the corresponding excitation at 320 nm wavelength; the synthesized C-CDs have bright fluorescence properties. However, the origin of fluorescence of CDs is still under investigation, it is assumed that it may be due to the surface trap states, surface defects, etc. Moreover, the fluorescence properties of C-CDs have been studied by changing the excitation wavelength from 300 to 380 nm. It was noticed that increasing excitation wavelength was accompanied by a gradual red shift to emission peaks with variable emission intensity.

### 3.4 IR Spectroscopy

IR spectroscopy is one of the most important and necessary characterization tools to evaluate the presence of different functional groups on the surface of CDs. The presence of C-N bond, Amino acid, Amide, N-H bond, ketone, aldehyde, alcohol, halogens, etc. can be determined using IR spectroscopy, which is used to reveal the complex formation mechanism between CDs and analytes. The broad peak at  $3350\text{ cm}^{-1}$  is due to the presence of hydroxyl ( $-\text{OH}$ ) functionality, and the peak at  $2215\text{ cm}^{-1}$  is due to  $\text{C}\equiv\text{C}$  stretching vibrations. The prominent peak at  $1623\text{ cm}^{-1}$  can be prescribed due to  $\text{C}=\text{C}$  stretching. The small peaks at  $1315\text{ cm}^{-1}$  and  $1110\text{ cm}^{-1}$  are due to C-O stretching [16]. It can be concluded from the FT-IR spectra that C-CDs are rich in carboxyl, and hydroxyl functionalities which can help to interact with various analytes.

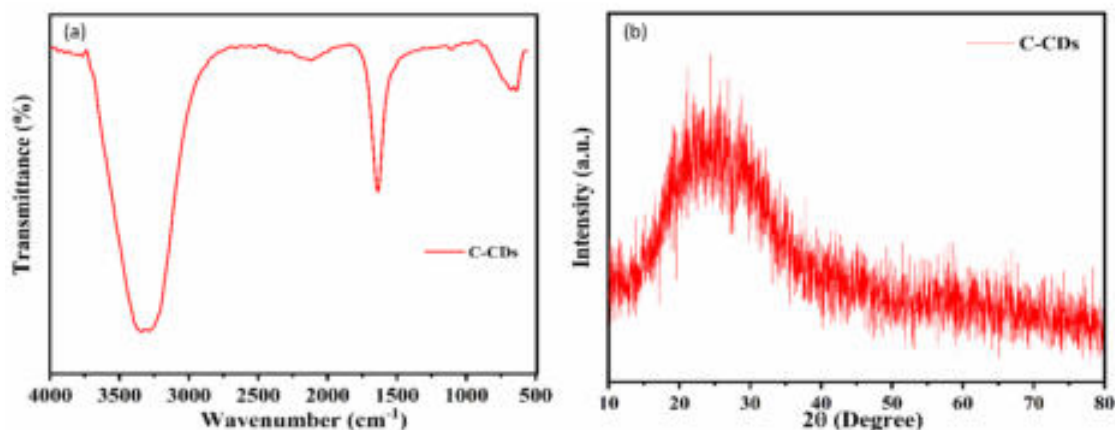


**Figure-4. (a) FT-IR and (b) XRD spectra of cinnamon carbon dots (C-CDs).**

### 3.5 XRD



The amorphous and graphite nature of CDs can be distinguished with the assistance of X-Ray diffraction. The XRD pattern of C-CDs displayed a broad peak centered at 20-30 degrees owing to the highly disordered structure of C-CDs. The broad peak at 23.5 degrees can be prescribed for the (002) plane showing the amorphous nature of C-CDs [17]. Fig. 3 (b) shows XRD spectra of C-CDs.

#### 4. CONCLUSION

In summary, an efficient, simple and economical approach has been utilized to synthesize C-CDs very successfully. The hydrothermal route (bottom-up approach) was utilized for the synthesis of C-CDs at 180<sup>0</sup>C for 12 hrs. The as synthesized C-CDs exhibited ideal fluorescent property showing bright blue colored fluorescence under UV light. The as synthesized C-CDs have excitation dependent behavior showing the highest emission intensity (446) nm at an excitation wavelength of 320 nm.

#### ACKNOWLEDGEMENT

We are very much thankful to the Department of Chemistry, Shivaji University, Kolhapur for the lab facilities as well as characterizations and also grateful to one of our authors (SVK) for financial support through Mahatma Jyotiba Phule Research Fellowship (MAHAJYOTI/2022/Ph.D. Fellow/1002 (909).

#### DECLARATION

Authors declare that, there is competing interests.

#### REFERENCES

1. Nille, O.S., Patil, A.S., Kolekar, G.B., Gore, A.H. In Environmental Remediation Through Carbon Based Nano Composites, edited by Jawaid, M., Ahmad, A., Ismail, N. and Rafatullah, M. (2021) pp.427–443.
2. Sun X., Lei Y. (2017) Trends in Analytical Chemistry, 89, 163–180.
3. Gattoo M. A., Naseem S., Arfat M. Y., Dar A. M., Qasim K., Zubair S. ( 2014) BioMed Research International Hindawi Publishing Corporation, 2014.
4. Makarov, V. V. (2014) Acta Naturae, 6, 35–44.
5. Nille, O. S. In Valorization Agri-Food Wastes By-Products Recent Trends, Innov. Sustain. Challenges, edited by Bhat, R. (2021) pp.219–236.
6. Jawaid, M., Ahmad, A., Ismail, N., Rafatullah, M. In Environmental Remediation Through Carbon Based Nano Composites, edited by Jawaid, M., Ahmad, A., Ismail, N., Rafatullah, M. (2021) pp.427–443.
7. Kang, C., Huang, Y., Yang, H., Yan, X. F., Chen, Z. P. (2020) Nanomaterials, 10, 1–24.



8. Yan, F., Sun, Z., Zhang, H., Sun, X., Jiang, Y., Bai, Z. (2019) *Microchimica Acta*, 186, 1-37.
9. Nille., O. S. In *Valorization Agri-Food Wastes By-Products Recent Trends, Innov. Sustain. Challenges*, edited by Bhat, R. Elseiver, (2021) pp.219–236.
10. Naik, V., Zantye, P., Gunjal, D., Gore, A., Anbhule, P., Kowshik, M., Bhosale, S., Kolekar, G. (2019) *ACS Applied Bio Materials*, 2(5), 2069-2077.
11. Ding, H., Yu, S. B., Wei, J. S., Xiong, H. M. (2016) *ACS Nano*, 10(1), 484-491.
12. Qi, B. P., Bao, L., Zhang, Z. L., Pang, D. W. (2016) *ACS Applied Materials & Interfaces*, 8(42), 28372-28382.
13. Patil, A. S., Nille, O. S., Kolekar, G. B., Sohn, D., Gore, A. H. (2021) *Sustainable Packaging*, 177-202.
14. Gunjal, D. B., Naik, V. M., Waghmare, R. D., Patil, C. S., Shejwal, R. V., Gore, A. H., Kolekar, G. B. (2019) *Journal of the Taiwan Institute of Chemical Engineers*, 95, 147-154.
15. Naik, V. M., Gunjal, D. B., Gore, A. H., Pawar, S. P., Mahanwar, S. T., Anbhule, P. V., Kolekar, G. B. (2018) *Diamond and Related Materials*, 88, 262-268.
16. Patil, A. S., Waghmare, R. D., Pawar, S. P., Salunkhe, S. T., Kolekar, G. B., Sohn, D., Gore, A. H. (2020) *Journal of Photochemistry and Photobiology A: Chemistry*, 400, 112647.
17. Gunjal, D. B., Gore, A. H., Bhosale, A. R., Naik, V. M., Anbhule, P. V., Shejwal, R. V., Kolekar, G. B. (2019) *Journal of Photochemistry and Photobiology A: Chemistry*, 376, 54-62.

# Synthesis and Characterization of Plant-Mediated CuO Nanoparticles

Omkar S. Nille<sup>a</sup>, Harshad A. Mirgane<sup>b</sup>, Sneha V. Koparde<sup>a</sup>, Akanksha G. Kolekar<sup>a</sup>, Ashlesha R. Pawar<sup>a</sup>, Pallavi J. Pawar<sup>a</sup>, Abhishek A. Waghmode<sup>a</sup>, Tanaji R. Dhage<sup>a</sup>, Vijay S. Ghodake<sup>a,d</sup>, Prasad M. Swami<sup>a</sup>, Sarita D. Shinde<sup>c</sup>, Govind B. Kolekar<sup>a,\*</sup>.

<sup>a</sup>Department of Chemistry, Shivaji University, Kolhapur 416 004 (MS) India.

<sup>b</sup>School of Chemical Sciences, Goa University, Goa 403 206 (Goa) India.

<sup>c</sup>Department of Chemistry, Vivekanand College, Kolhapur 416 003 (MS) India.

<sup>d</sup>Department of Chemistry, Yashwantrao Chavan Mahavidyalaya, Halkarni, Kolhapur 416 552 (MS) India.

\*Corresponding author: gbk\_chem@unishivaji.ac.in, gbkolekar@gmail.com

---

## ABSTRACT

*In present study, we aim to synthesize Copper Oxide Nanoparticles (CuO NPs) using Clitoriaternate seed pod extract at room temperature without the addition of any previous capping agents. The obtained CuO NPs were characterized by UV-Visible spectroscopy, x-ray diffraction (XRD), and Fourier transforms infrared spectroscopy (FTIR). It shows a monoclinic crystal structure with an approximate 20.41 nm crystalline size. The synthesized material is having potent antimicrobial properties.*

## KEYWORDS

*Clitoriaternate, Green synthesis, CuO NPs.*

.....

## 1. INTRODUCTION

Nanostructure Science and technology is a broad and interdisciplinary area of research and development activity that has been growing explosively worldwide in the past few years. It has the potential for revolutionizing the ways in which materials and products are created and the range and nature of functionalities that can be accessed. For these reasons, many research groups have an increasing interest in the development and study of this material[1]. In recent years' metal oxide nanoparticles (NPs) are widely used due to their extensive application in catalysis[2], gas sensing[3], solar cells [4], high semiconductors properties[5], etc. CuO is a good p-type semiconductor that exhibits a narrow band gap of 1.2 eV. Owing to its unique optical, electrical, and magnetic properties which lead it to various biomedical[6], catalytic[2], and sensor applications[7]. There are several methods that have been developed for synthesizing metal oxide NPs such as the sol-gel method[8], pyrolysis method, hydrothermal method, Vacuum- vapor decomposition, colloidal thermal method, etc.[9].

The chemical routes of synthesis are mostly employed with toxic chemicals, precursors, capping agents, solvents, and reducing and oxidizing agents which contain potentially toxic impurities[10]. These toxic elements lead to unsuitable use of these nanomaterials for applications in clinical and biomedical fields. To overcome these issues researchers had developed some clean and green methods for the synthesis of important nanomaterials. The green synthesis route is not just environment-friendly but also non-toxic for living beings [11-19]. Synthesis NPs using plant extract from *Gloriosa superba* L., *Fusarium oxysporum*[11], *Saracaindica*[12], *Lactobacillus storage*[13], *Aloe-vera*[14], *Albizialebeck leaf*[15], *Brown algae*[16], *Calotropis progeria*, *L. latex*[17], *Gum Karya*, *Tinosporacordifolia*[18], *Azadirachtaindica*[6], *Cassia auriculata*[19], etc. via green synthesis route have been reported. The *Clitoriaternatea* commonly known as Asian pigeon wings is a flowering plant belonging to the Fabaceae family known for its antimicrobial, antipyretic, anti-inflammatory, analgesic, diuretic, local anesthetic, antidiabetic and insecticidal in Ayurveda[20].

In this work, seed pods of *Clitoriaternatea* were used as reducing and capping agents for the synthesis of CuO NPs. The crystal structure, surface morphology, and sizes was characterized by using UV–Visible spectroscopy, XRD, SEM, and FTIR techniques. The efficiency of CuO NPs as catalysts for one pot organic synthesis of bis(indolyl)methane was studied. We also carried out the antimicrobial test of the biosynthesized CuO NPs.

## 2. MATERIAL AND METHOD

All chemicals were of AR grade and used without any further purification. The Copper sulphate ( $\text{CuSO}_4 \cdot 6\text{H}_2\text{O}$ ) was used as Copper (Cu) source and freshly prepared powder of well sundried seeds of *Clitoria* as a complexing agent.

### 2.1 Preparation of plant extract

Freshly collected seed pods of *Clitoriaternatea* were dried in sunlight for one day in dust free conditions. After completely dried seeds were grinded to get fine powder. About 5g of seed powder was added to 500 ml of de-ionized water and kept for boiling at 80°C for about 1 hour. The appearance of the light brownish colored solution was observed which settled down at room temperature. The formed precipitate was filtered and the obtained supernatant was stored at 4°C in the refrigerator for further use. The **Figure-1** shows the preparation of plant extract. synthesis route of CuO NPs.



**Figure-1. Preparation of *Clitoria ternatea* plant extract.**

## **2.2 Synthesis of Copper oxide (CuO) nanoparticles**

Required amount of precursor  $\text{CuSO}_4 \cdot 6\text{H}_2\text{O}$  was dissolved in de-ionized water to prepare 0.5 N 100 mL solutions after stirring for some time. Then 50 mL of *Clitoria ternatea* plant seed extract was mixed with 50 mL precursor solution in equal ratio (1:1 v/v) drop by drop with stirring. Then whole solution stirred for 15 min till the formation of a brownish colored precipitate which is allowed to settle. The solution was filtered and finally washed 2–3 times with distilled water to remove impurities followed by drying at  $80^\circ\text{C}$  in hot air oven for 3 h. The **Figure-2** shows the experimental setup for green synthesis of CuO NPs.



**Figure-2. Schematic experimental set up for the synthesis of CuO NPs.**

## **3. RESULTS AND DISCUSSION**

Optical absorption measurement was performed in the wavelength range 350–1100 nm by using a UV-visible spectrophotometer (UV-1800, Shimadzu, Japan). The X-ray Diffraction (XRD) spectrum of the film was recorded using X-ray diffractometer (Bruker AXS Model D8 Advance X-ray Diffractometer) with  $\text{Cu K}\alpha$  target having

wavelength 1.542 Å. The Fourier transform infrared (FT-IR) spectra of samples were collected using a Spectrum100 Perkin Elmer FT-IR spectrophotometer using pellets made by mixing the sample with KBr, to investigate the functional groups of the CuO nanoparticles.

### 3.1 Optical absorption study

The room temperature optical absorption spectra of the CuO thin film recorded in the range of 380-1000 nm without taking into account scattering and reflection losses. **Figure-3** shows variation in the optical absorption with wavelength[21].

The extrapolation of straight line portions to zero absorption coefficient ( $\alpha = 0$ ), leads to the estimation of the band gap energy values which is found to be 3.4 eV due to quantum size effect. Which confirms the synthesized material was CuO NPs. Quantum confinement leads to a collapse of the continuous energy bands of a bulk material into discrete, atomic like energy levels. Thus, one observes an increase in the band gap of the semiconductor with a decrease in the particle size.

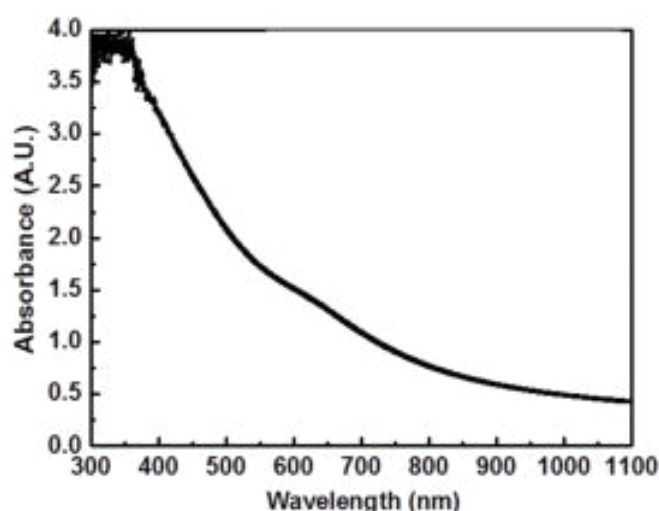


**Figure-3.**Optical absorption spectra of CuO NPs.

### 3.2 X-Ray diffraction (XRD) study

The XRD patterns of the CuO thin films are shown in **Figure-4**. The comparison of observed XRD patterns with the standard JCPDS data (Card no. 80-0076) confirms the formation of a CuO phase with monoclinic crystal structure.

The lattice parameters were calculated from XRD data as follows,  $a = 4.529 \text{ Å}$ ,  $b = 3.43 \text{ Å}$ ,  $c = 5.07 \text{ Å}$ . The CuO film exhibits XRD peak corresponding to (110) plane. Besides this major peak, nine more peaks corresponding to (111), (220), (202), (020), (113), (022), (420), (422) and (311) planes are observed. This suggests that, CuO phase is stable[22].

Further, the average crystallite size was calculated using a well-known Debye-Scherrer's as described in equation (1).

$$D = \frac{0.9\lambda}{\beta \cos \theta} \quad (1)$$

where,  $\lambda$  is the wavelength of X-rays (1.5406 Å),  $\beta$  the full width at half maximum (in radian) of the peak,  $D$  is the diameter of the crystallite and  $\theta$  is Bragg's angle of XRD peak. Further, the average crystallite size is estimated using Scherrer's formula is approximately 20.41 nm.

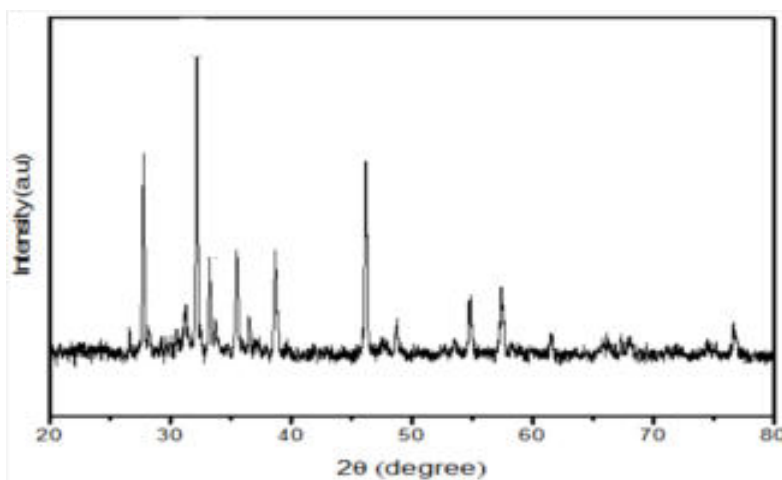


**Figure-4. X-ray diffraction pattern of the CuONPs.**

### 3.3 Fourier transform infrared (FT-IR) spectroscopy:

FT-IR spectroscopy was carried out to identify the functional groups present in the *C. ternatea* which acts as reducing and capping agents of synthesized CuO NPs as shown in **Figure-5**. FTIR measurements were carried out to identify the possible biomolecules responsible for the capping and efficient stabilization of the silver nanoparticles synthesized by the plant extracts. The spectra consist of nine vibrational bands. The band at  $521 \text{ cm}^{-1}$  is due to copper oxide and assigned to the stretching of Cu–O. The vibrations due to the carboxyl group are obtained in the range of  $1382\text{--}1393 \text{ cm}^{-1}$ .

The stretching mode of vibration corresponding to C=C is obtained at  $1509 \text{ cm}^{-1}$  and due to the alkyl group are obtained in the range  $2847\text{--}2923 \text{ cm}^{-1}$ .

The band arising from the absorption of atmospheric  $\text{CO}_2$  on the metallic cations at  $2350 \text{ cm}^{-1}$  is clearly seen in the FTIR spectra. The bands at  $3200\text{--}3600 \text{ cm}^{-1}$  correspond to the O–H mode of vibration, i.e. due to the hydroxyl

group[23].The presence of hydroxyl group in IR spectrum may be due to absorption of water during mixing and pelleting with KBr.

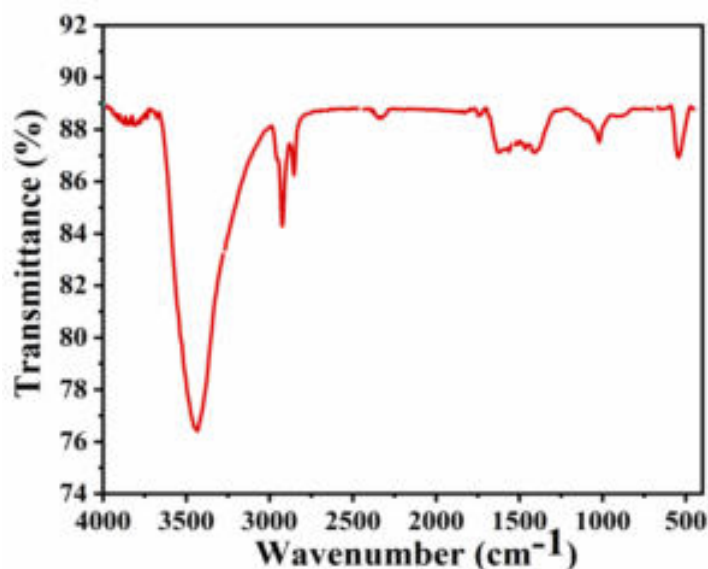


**Figure-5:FTIR transmission spectra of the CuO NPs.**

#### **4. CONCLUSION**

We demonstrate a simple and low temperature strategy of chemical synthesis of CuO NPs. The XRD analysis gave the formation of polycrystalline CuONPs with monoclinic crystal structure. Existence of different peaks of CuO nanoparticles in FTIR revealed the formation of CuONPs and presence of different surface functional groups. This procedure offers several advantages including mild condition, high yields, inexpensive catalyst, and operational simplicity, wide scope of applications.

#### **ACKNOWLEDGEMENT**

Grateful to one of our authors (SVK) for financial support through Mahatma Jyotiba Phule Research Fellowship (MAHAJYOTI/2022/Ph.D.Fellow/1002 (909)) and we are very much thankful to the Department of Chemistry, Shivaji University, Kolhapur for the lab facilities as well as characterizations.

#### **DECLARATIONS**

Authors declare that, there is competing interests.



## REFERENCES

1. Mobasser, S., Firoozi, A. (2016) *Journal of Civil Engineering and Urbanism*, 6, 84–93.
2. Nasrollahzadeh, M., Sajadi, S. M., Rostami-Vartooni, A., Hussin, S. M.(2016)*Journal of Colloid and Interface Science*,466, 113–119.
3. Mahajan, S., Jagtap, S. (2020) *Applied Materials Today*,18,100483,.
4. Rai,P. (2019)*Sustainable Energy & Fuels journal*,3, 63–91.
5. Liao, W. Q. (2015) *Nature Communications*, 6, 1–7.
6. Sharma, B. K., Shah, D. V., Roy, D. R. (2018) *Materials Research Express*, 5, 0–7.
7. Ashok, A. Kumar, A., Tarlochan, F. (2019) *Applied Surface Science*, 481, 712–722.
8. Parashar, M., Shukla, V. K.,Singh,R. (2020) *Journal of Materials Science: Materials in Electronics*, 31, 3729–3749.
9. Rane, A.V., Kanny, K., Abitha, V.K., Thomas, S. (2018) In *Synthesis of inorganic nanomaterials*, edited by Bhagyaraj, S. M., Oluwafemi, O. S., Kalarikkal, N., Thomas, S. Woodhead publishing, (2018) pp. 121-139.
10. Sharifi, S., Behzadi, S., Laurent, S., Forrest, M. L., Stroeve, P., Mahmoudi, M. (2012)*Chemical Society Reviews*, 41. 2323–2343.
11. Uddin, I., Adyanthaya, S., Syed, A., Selvaraj, K., Ahmad, A., Poddar, P. (2008) *Journal of Nanoscience and Nanotechnology*, 8, 3909–3913.
12. Vidhu, V. K., Philip, D. (2015) *Spectrochimica Acta Part A: Molecular and Biomolecular Spectroscopy*,134, 372–379.
13. Nagajyothi, P. C., Muthuraman, P. T., Sreekanth, V. M., Kim, D. H., Shim, J. (2017) *Arabian Journal of Chemistry*, 10, 215–225.
14. Pammi, V. N. (2015) *Bionanoscience*, 5(3), 135–139, 2015.
15. Jayakumarai, G., Gokulpriya, C., Sudhapriya, R., Sharmila, G., Muthukumaran, C (2015) *Applied Nanoscience*, 5, 1017–1021.
16. Mittal, A. K., Chisti, Y., Banerjee, U. C. (2013) *Biotechnology Advances*, 31, 346–356.
17. Harne, S., Sharma, A., Dhaygude, M., Joglekar, S., Kodam, K., Hudlikar, M. (2012) *Colloids Surfaces B Biointerfaces*, 95, 284–288.
18. Padi, V. V. T., Cernik, M.(2013) *International Journal of Nanomedicine*, 8,



- 889–898.
19. Prasad, K. S. (2020) *Biomolecules*, 10, 1–14.
  20. Mukherjee, P. K., Kumar, V., Kumar, N. S., Heinrich, M. (2008) *Journal of Ethnopharmacology*, 120, 291–301.
  21. Ravishankar, T. N., Vaz, M. D. O., Teixeira, S. R. (2020) *New Journal of Chemistry*, 44, 1888–1904.
  22. Radhakrishnan, A. A., Beena, B. B. (2014) *Indian Journal of Advances in Chemical Science*, 2, 158–161.
  23. Reddy, K. R. (2017) *Journal of Molecular Structure*, 1150, 553–557.

---

---

## GUIDELINES FOR CONTRIBUTORS

---

---

- 1] **Journal of Shivaji University : Science & Technology** is the publication of Shivaji University, Kolhapur (Maharashtra, India), being published twice a year. It is an academic peer reviewed ISSN approved Journal.
- 2] The Journal welcomes research articles based on original research, review papers, research communication/notes by the faculty and research scholars working in various fields of Science and Technology. Articles/Papers can be submitted in English language only.
- 3] The length of manuscripts should not exceed 6000 words for review article, 5000 words for research article, 2000 words for research communication and 1000 words for research note.
- 4] The article/paper must accompany an **abstract not exceeding 200 words**.
- 5] During writing and submission of a manuscript, please follow the author guidelines available on the home page of Journal of Shivaji University: Science and Technology.
- 6] All the sources of literature referred to while writing the article/paper must be properly cited in the text. The serial numbers of End Notes, if any, must also be indicated within text at appropriate places.
- 7] The listing of references must follow the standard format.
- 8] Tables, charts, maps, figures etc. should be placed at appropriate places in the text of the article/paper and must be numbered serially with suitable headings. The tables should be referred to by their numbers within the text. Art-work for maps, figures and charts should be provided separately, if necessary.
- 9] Only articles evaluated and approved by the subject Experts/Referees/Departmental editorial board are considered for their publication in the Journal. The referees evaluate Article/ Paper drafts in term of structure and organization of paper/argument, originality of the research, appropriateness of abstract and introduction, literature review, methodology and data sources, data/evidence and conclusions, and quality of language.
- 10] The name of the author/co-author of the article being submitted should mentioned on the first page of the article/paper below title of that article. An asterisks (\*) is used for defining corresponding author/s of a manuscript.
- 11] For any other information and for inquiries regarding submitted articles/papers preferably use e-mail communications. (**E-mail : editor.jscitech@unishivaji.ac.in**)
- 12] Manuscript should be sent to email of the Editor (**editor.jscitech@unishivaji.ac.in**) {or associate editor of the concerned subject}, Journal of Shivaji University: Science and Technology, Kolhapur with e-copy only (single M.S. word as well as PDF file).  
**Only research articles/review papers/research communication/notes prepared strictly in accordance with the above guidelines will be sent to referees for their evaluation and opinion about their acceptability or otherwise. We do not send back rejected articles.**

